OCEAN BEACH DUNEDIN

A numerical study of the coastal dynamics

Prepared for Dunedin City Council

July 2010

Suite 3, 17 Nobs Line, New Plymouth, New Zealand
T: 64-6-7585035 E: enquires@metocean.co.nz

Report Status

Version	Date	Status	Approved By:
RevA	21/10/2009	Draft for internal review	McComb
RevB	30/10/2009	Draft for client review	Johnson
RevC	09/11/2009	Updated draft for client review	McComb
RevD	12/11/2009	Updated draft for client review	McComb
RevE	20/07/2010	Final draft for internal review	Johnson
RevF	23/07/2010	Final draft for client review	McComb
Rev0	04/08/2010	Approved for release	McComb

It is the responsibility of the reader to verify the currency of the version number of this report. This report was prepared by D. Johnson, P. McComb, B. Beamsley, S. Weppe and R. Zyngfogel.

TABLE OF CONTENTS

LIST OF TABLES

LIST OF FIGURES

EXECUTIVE SUMMARY

A numerical study of wave, current and sediment transport along Ocean Beach, Dunedin has been undertaken. The study has made use of available local oceanographic data to validate numerical models, which have been used to simulate the coastal dynamics, particularly under storm conditions. The work to date has clearly identified the key physical processes that dominate the sediment dynamics along Ocean Beach. A set of robust numerical tools has been established which can be used to evaluate a range of potential management options for the beach.

The Ocean Beach wave climate was re-created (hindcast) for a 10-year period (1998-2007), with the results indicating that the nearshore wave climate is strongly influenced by White Island and its' underwater features. The combined effects of sheltering and wave refraction and seabed friction cause a wave height shadow that extends over the western half of Ocean Beach. The shadowing effect varies with the incoming wave conditions, so the wave energy gradients along the beach front are not constant. The dominant condition, however, is for larger waves to reach the shore between Lawyers Head and St Kilda, and a transition zone to lower wave energy typically located between St Kilda and Middles Beach. The wave climate at St Clair is consistently less energetic than St Kilda and the eastern third of Ocean Beach.

The open ocean current regime for Dunedin area was hindcast for a 5-year period (1998-2002), considering both the tidal and non-tidal components of flow. Near Ocean Beach, the currents are predominantly directed alongshore and to the east, and the tides make only a small contribution to the overall flow regime. The current flows are accelerated between White Island and the St Clair Headland, and also in the region to the east of Lawyers Head. The underwater features of White Island create a slight current shadow in their lee. The periods with the highest current flows are during stormy conditions, with strong winds and large waves.

The sediment transport and response of the beach to southerly and southeasterly storms has been modeled. Southerly storms are the most frequent, and under these conditions there is a consistent pattern of wave-driven circulation, sediment transport, and areas of beach erosion (see Fig. E1). The gradient in wave height along the beach drives a persistent westerly-directed flow within the surf zone along the western third of the beach. Seaward of the surfzone, there is another broader zone of westward flow that also extends along much of the western parts of the beach. In the central beach regions the flows tend to split; with a broad westerly flow on one side and easterly flows on the other. At the eastern end of the beach, the flows are mainly directed eastward but also feature recirculating regions associated with rip channels.

Active erosion of the upper beach face occurs primarily along the western half of the beach, with the eroded material being deposited in the beach trough and then moved westward by the strong surfzone currents. In southerly storms, the morphology model predicts shoreline erosion from just west of St Kilda Beach to the immediate east of St Clair Beach.

The outcome for the southeasterly storm condition is very different. Here, the wave height gradient is reversed and there is more energy reaching the St Clair end of the beach. The current flows and sediment transport are uniformly directed to the west, and there is no significant rip cell circulation. However, strong nearshore flows and intertidal beach erosion occurs from St Kilda to St Clair, as also observed during the southerly storms.

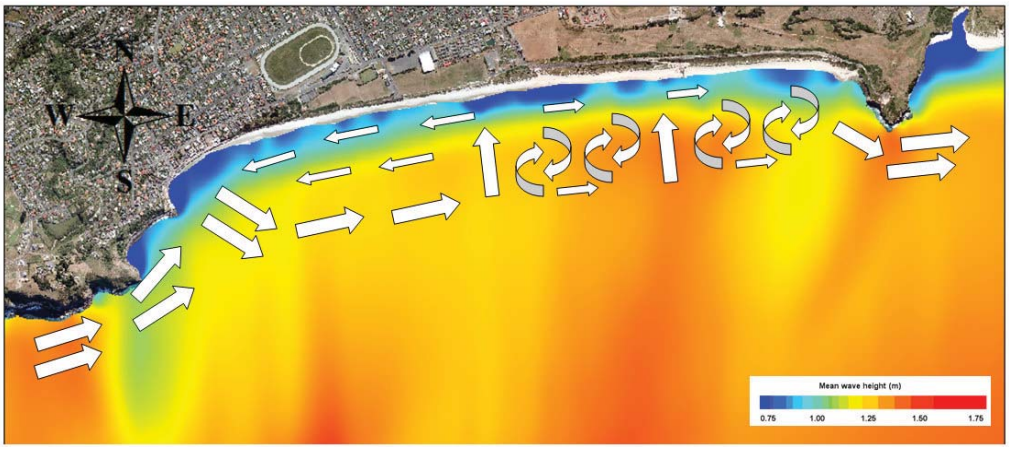

Figure E1 Conceptual diagram showing the mean sediment transport pathways during southerly storm conditions, along with the annual mean significant wave height.

1 INTRODUCTION

1.1 Scope

The Dunedin City Council has initiated a numerical model study of Ocean Beach, on the southern margin of the city and adjacent to the suburbs of St Clair and St Kilda. The purpose of the study is to gain an understanding of the coastal processes along the shoreline from St Clair to Lawyers Head (Fig. 1.1), and to use the models to identify and investigate coastal protection options and management scenarios. The specific aims of the model study are to:

1. Quantify the frequency and longshore variability of inshore wave heights, periods and direction.
2. Determine sediment transport directions and quantify flux volumes.
3. Characterise the morphological response of the beach to storm events.
4. Undertake evolution modeling to determine responses from possible management options.

This report considers the first three aims in the study scope.

1.2 Report structure

This report is structured as follows. The data sources and numerical techniques and methodologies are detailed in the following sections; wave modeling is presented in Section 2, the ocean current modeling in Section 3, and the morphology modeling methods are described in Section 4. The local and regional wave climate results are presented in Section 5, with additional wave data tables appended to the report. The ocean current regime is characterised in Section 6. Morphology modeling outcomes are presented and discussed in Section 7. A summary of the dominant physical process is provided in Section 8, and recommendations for future modeling of potential management options

are presented in Section 9. The references cited in this report are listed in the final Section 10.

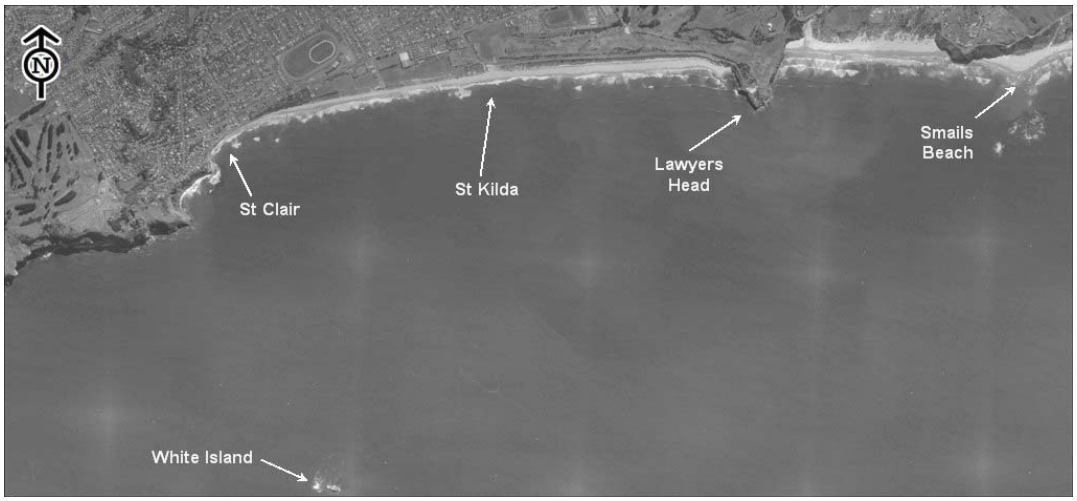

Figure 1.1 Ocean Beach study zone, extending from St Clair to Lawyers Head.

2 WAVE HINDCAST MODELLING METHODS

2.1 Bathymetric and topographic data

Bathymetric and shoreline data for regional and local scale modeling (i.e. for waves, currents and sediment transport) have been collated from several sources, including:

- Published navigation charts and archived NZOI and RNZ Navy soundings.
- Near shore hydrographic survey of Ocean Beach undertaken in December 2008 by Hunter Hydrographics Ltd.
- Beach topographic survey collected data by the University of Otago.
- LIDAR data held by the Otago Regional Council.

2.2 Wind inputs

A spatially varying wind field was specified from a blended global wind product developed by MetOcean Solutions Ltd. These data are 10 m wind velocity vectors in a 3-hourly gridded format at a resolution of 0.25° of longitude and latitude. The wind field is a combination of the 6-hourly Blended Sea Winds data[1] and 3-hourly NWW3 model wind fields[2] from the National Centers for Environmental Prediction (NCEP) at the United States National Oceanic and Atmospheric Administration (NOAA). The blended data product combines the benefits of measured satellite data with the temporal resolution and continuous coverage of the modeled re-analysis.

For this project, a regional validation was performed using one year of data from the wind station on the Southwest Cape of Stewart Island (47.278S,

[1] From the NOAA National Climatic data Center (NCDC), Zhang (2006).
[2] These wind fields are used in the NCEP Wavewatch III global wave hindcast (NWW3), and consist of analyses and 3-hour forecasts from NCEP's operational Global Data Assimilation Scheme (GDAS) and the aviation cycle of its Medium Range Forecast model.

167.464E). The station data are measured at an elevation of 101 m above sea level, while the Blended data are at the reference level of 10 m elevation. Comparison plots for the east/west and north/south components of velocity are shown on Figure 2.1.

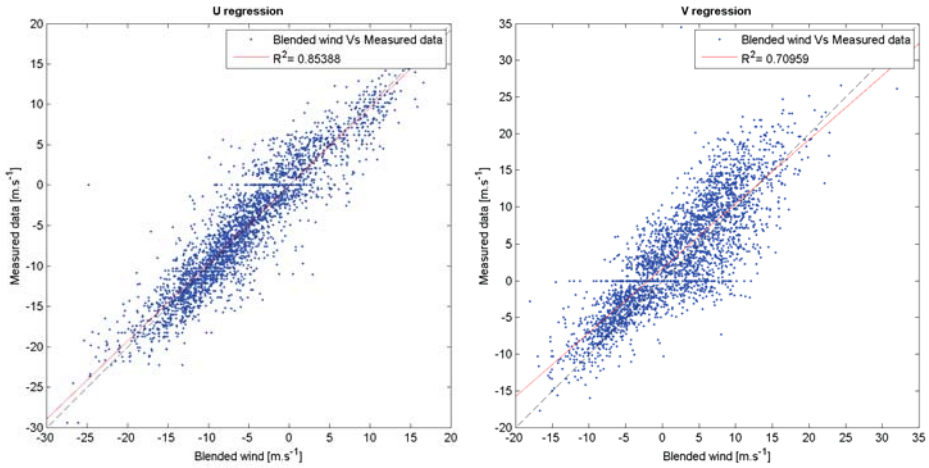

Figure 2.1 Comparison of the raw measured wind data from SW Cape (Stewart Island) and the Blended Wind product for the same location.

2.3 Wave hindcast model

SWAN (Simulating Waves Nearshore) was used for the regional hindcast wave modeling. SWAN is a third generation ocean wave propagation model, which solves the spectral action density balance equation for wavenumber-direction spectra. This means that the growth, refraction and decay of each component of the complete sea state, each with a specific frequency and direction, is solved, giving a complete and realistic description of the wave field as it changes in time and space. Physical processes that are simulated include the generation of waves by surface wind, dissipation by white-capping, resonant nonlinear interaction between the wave components, bottom friction and depth limited breaking. A detailed description of the model equations, parameterizations and numerical schemes can be found in the SWAN Manual (2009)[3]. All 3rd generation physics are included. The Collins friction scheme is used for wave dissipation by bottom friction with a friction factor of 0.015 used throughout.

[3] Available online at: http://vlm089.citg.tudelft.nl/swan/online_doc/swanuse/swanuse.html

The solution of the wavefield is found for the non-stationary (time-stepping) mode. Boundary conditions, wind forcing and resulting solutions are all time dependent, allowing the model to capture the growth, development and decay of the wavefield.

Multiple, nested numerical domains were established for the regional and local modeling. Fully nested spectral open ocean boundaries on the NZ domain were obtained from the MetOcean Solutions global WW3 hindcast[4] and the Blended Wind product (section 2.1) was used to specify a spatially-varying wind field. The regional scale model domain extended from 170.17˚E to 170.9˚E and 46.17°S to 45.63°S (Figure 2.2), on a longitude/latitude grid with resolution of 0.006˚ by 0.005˚ (approximately 500 m by 500 m). The local scale domain had a grid size of approximately 50 m, extending east-west over all of Ocean Beach and nearby coastline, and offshore beyond White Island (Figure 2.3).

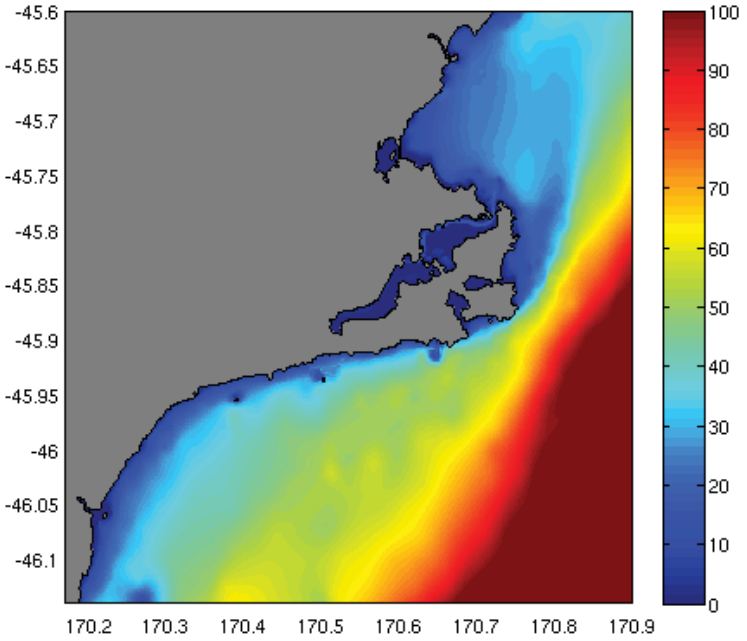

Figure 2.2 Regional wave hindcast domain.

[4] The MetOcean Solutions Ltd (MSL) global WW3 hindcast replicates the NOAA WaveWatch3 (NWW3) hindcast, using the same domain, forcing winds and then assimilating the NWW3 significant wave heights. The MSL WW3 output is effectively identical in terms of spectral parameters, but has the advantage of full spectra being available at arbitrary locations and on nested model boundaries.

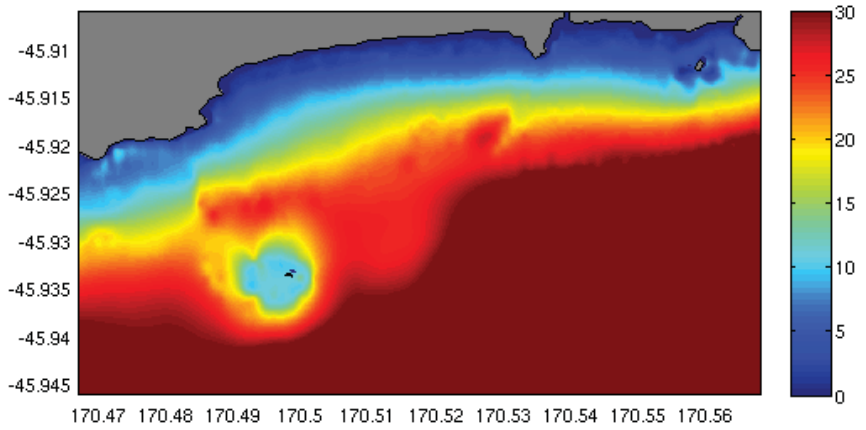

Figure 2.3 Local scale wave hindcast domain.

2.4 Spectral parameters

Directional wave spectra were output at hourly intervals over the hindcast run; with 10 years of data available for the study (1998 – 2007). The standard spectral wave parameters were derived as follows. Given a directional wave spectrum $S(f,\theta)$, the 1-dimensional spectrum is obtained by integrating over directions:

$$S(f) = \int_0^{2\pi} S(f,\theta)d\theta \qquad (2.1)$$

From the computed spectral energy density $S(f)$, the peak frequency f_p and peak energy $S_p = S(f_p)$ of the spectrum are located. Spectral moments

$$M_j = \int_0^{\infty} f^j S(f)\, df \qquad (2.2)$$

are computed, allowing further statistics to be defined:

significant height $H_s = 4\sqrt{M_0}$ (2.3)

mean period $T_{m1} = M_0 / M_1$ (2.4)

Directional moments are:

$$M_c = \int_0^{\infty}\int_0^{2\pi} S(f,\theta)\cos\theta \; d\theta \, df \tag{2.5}$$

$$M_s = \int_0^{\infty}\int_0^{2\pi} S(f,\theta)\sin\theta \; d\theta \, df \tag{2.6}$$

The mean direction is $\theta_0 = \arctan\left(\frac{M_s}{M_c}\right)$ (2.7)

2.5 Extreme value analysis (EVA)

The derivation of return period values in this report is based on the advice of Holthuijsen (2007). The *Peaks over Threshold* (POT) sampling method was used for wave height data selection, applying the 90th percentile exceedence level as the threshold - consistent with the methods of Caires and Sterl (2004). The selected storm wave events were fitted to a General Pareto Distribution (GPD), with the location parameter fixed by the threshold and the Maximum Likelihood Method (MLM) used to obtain the scale and shape parameters. Return period values are calculated for the omni-directional condition. Guidance on the probable range of peak wave periods ($T_{ass,\ min}$ and $T_{ass,\ max}$) associated with the return period extrema is assumed to be steepness-limited and having the relationship:

$$\sqrt{13H_s} \le T_{ass} \le \sqrt{30H_s} \; . \tag{2.8}$$

3 CURRENT HINDCAST MODELLING METHODS

A 5-year hindcast of the ocean currents was implemented for the study. The MSL implementation of POM (Princeton Ocean Model) was used to hindcast the depth-averaged wind-driven and tidal currents in the wider Otago region as well as at high-resolution in the Ocean Beach area. The details of the model are described in Mellor (2004)[5]. The POM code has been used for numerous scientific applications studying oceanic and shelf circulation.

3.1 Model equations

For the hindcast simulations, MSL-POM is used in a vertically integrated two-dimensional mode, solving the momentum and mass conservation equations given by:

$$\frac{\partial u}{\partial t}+u\frac{\partial u}{\partial x}+v\frac{\partial u}{\partial y}-fv=-g\frac{\partial \eta}{\partial x}-\frac{1}{\rho}\frac{\partial P_a}{\partial x}+A_H\left(\frac{\partial^2 u}{\partial x^2}+\frac{\partial^2 u}{\partial y^2}\right)+\frac{\tau_w^x}{\rho h}-\frac{\tau_b^x}{\rho h}$$

$$\frac{\partial v}{\partial t}+u\frac{\partial v}{\partial x}+v\frac{\partial v}{\partial y}-fv=-g\frac{\partial \eta}{\partial y}-\frac{1}{\rho}\frac{\partial P_a}{\partial y}+A_H\left(\frac{\partial^2 v}{\partial x^2}+\frac{\partial^2 v}{\partial y^2}\right)+\frac{\tau_w^y}{\rho h}-\frac{\tau_b^y}{\rho h}$$

$$\frac{\partial \eta}{\partial t}+\frac{\partial(u[h+\eta])}{\partial x}+\frac{\partial(v[h+\eta])}{\partial y}=0 \qquad \text{(3.1 a,b,c)}$$

where t is the time, u and v are the depth-averaged velocities in the x and y directions respectively, h the depth, η is the elevation of the surface, g the gravitational acceleration, f the Coriolis parameter, ρ the density of water, and P_a is atmospheric pressure.

A_H is a horizontal eddy viscosity coefficient, calculated with a Smagorinsky parameterisation,

[5] The numerical model code is freely available as open source.

$$A_H = C_m \Delta x \Delta y \frac{1}{2}\left[\left(\frac{\partial u}{\partial x}\right)^2 + \left(\frac{\partial v}{\partial x} + \frac{\partial u}{\partial y}\right)^2 + \left(\frac{\partial v}{\partial y}\right)^2\right]^{\frac{1}{2}} \qquad (3.2)$$

with C_m set at 0.2.

The surface and bottom shear stress, τ_w and τ_b are due to wind and bottom friction. The bed shear stress is parameterised with a quadratic type friction law,

$$\tau_b^x = C_D \sqrt{\left(u^2 + v^2\right)} u \quad \tau_b^y = C_D \sqrt{\left(u^2 + v^2\right)} v \qquad (3.3\ a,b)$$

that depends on an adjustable drag coefficient, $C_D \sim 10^{-3}$

The wind shear stress is parameterised by:

$$\tau_w^x = \rho_a \gamma |W_{10}| W_{10}^x \quad \tau_w^y = \rho_a \gamma |W_{10}| W_{10}^y \qquad (3.4\ a,b)$$

where ρ_a is the density of air and γ is a coefficient given by:

$$\gamma = \left(A + B|W_{10}|\right) \times 10^{-3} \qquad (3.5)$$

W_{10} is the wind velocity 10 m above sea level and A and B are coefficients with values 0.001 and 0.0001 respectively.

The model equations are solved with finite differences and explicit time-stepping, limited by a Courant condition.

3.2 Model domain

The Otago regional domain (see Fig. 3.1) with a resolution of 0.003˚ by 0.003˚ (approximately 230 m by 330m) was nested within a national domain, which covers all of New Zealand and surrounding waters, with a resolution of 0.06˚ by 0.06˚ (approximately 4-5 km by 6 km).

3.3 Boundary conditions and surface forcing

The same boundary conditions are applied at all open boundaries. For the surface elevation, an Orlanski type radiation boundary condition is applied, but with the normal component of the outgoing phase speed determined as the normal projection of the full oblique phase speed. (*NPO* in Marchesiello *et al.,* 2001). For the normal component of depth-averaged velocity, u_n, a Flather (1976) type constraint is used,

$$u_n = u_n^b + \sqrt{\frac{g}{h}}\left(\eta - \eta^b\right) \tag{3.6}$$

The boundary values of u_n^b and η^b are known boundary values for the surface elevation and depth-averaged current.

The TPXO7.1 global inverse tidal solution (Egbert and Erofeeva, 2002) was used to prescribe the tidal elevation and current velocity at the boundaries of the larger scale New Zealand-wide grid. For the nested regional grid boundaries were obtained for the NZ solution.

Surface forcing, both the 10 m winds and atmospheric pressure were input into the model. The surface pressure is from the NCEP global reanalysis and surface winds are from the Blended Sea Winds data (as for the wave modeling). Wind velocity components and atmospheric pressure were interpolated linearly in both space and time onto the model grid.

3.4 Model output

The 2D hydrodynamic model was used to hindcast the 5-year period from 1998 to 2002, inclusive. Depth-averaged currents were archived at 3-hourly intervals. An example of the current field in the Otago region is presented in Figure 3.1, also illustrating the extent of this model domain.

To interpolate the 3-hourly depth-averaged currents to smaller timesteps, a combined tidal/residual method was used. Harmonic analysis was applied to the full 3-hourly model timeseries to derive the tidal constituents of the current. The

tidal contribution is then calculated and subtracted from the raw model output to leave a slowly varying residual flow. For a given time, the total flow is then reconstructed from the tidal signal calculated from the constituents and the residual component determined by cubic interpolation from the 3-hour residual timeseries.

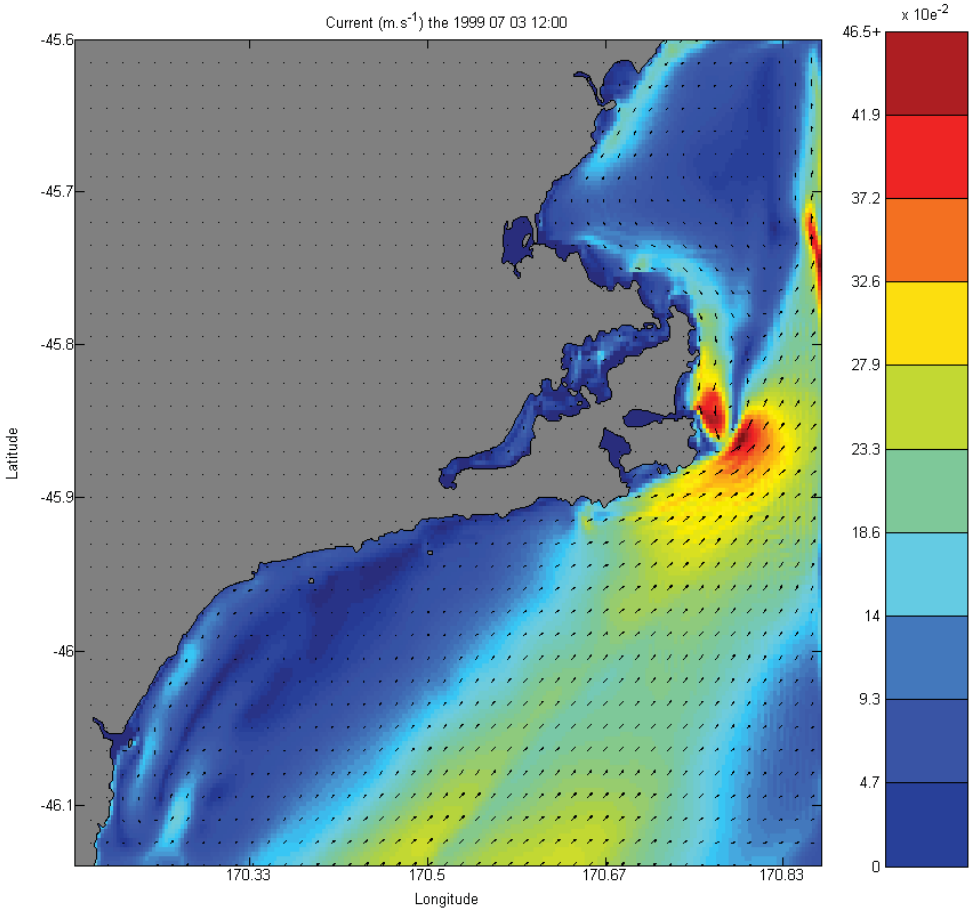

Figure 3.1 Example of modeled depth-averaged current field for a single time step (12:00 07/03/1997) in the 5-year hindcast. A complex interaction is evident between the northerly-directed flows past Cape Saunders, and a residual southerly flow along the margin of the northern Otago Peninsula.

4 MORPHOLOGY MODELLING METHODS

The morphology model is a tool that can be employed to identify the nearshore erosion / accretion patterns as well as provide some quantification to the local-scale coastal processes. Specifically, the model simulates the response of the seabed due to the alongshore and cross-shore sediment transport under the nearshore wave-current interactions.

The numerics of a morphology model need to calibrated and validated to ensure the physical process in the study environment are being properly represented. In this section, the numerical schemes are first described, and then an implementation of the model is presented showing the formation of a tombolo behind an offshore breakwater. This is a common 'benchmark' often used to compare morphology models. A previous implementation of the model considered the accretion of the breakwater tip shoal at Port Taranaki over a six-month period, with comparison to actual survey data. This provided a robust validation that the model can replicate the dominant aspects of the sediment transport regime under complex conditions. However, it must be noted that no subtidal data is available for model validation or calibration at the Ocean Beach site investigated in this work.

4.1 Model system

The complete model system consists of three modules:

- Nearshore wave propagation model to simulate the transformation of the incoming wavefield.
- Nearshore wave-driven current model to simulate currents generated by the incident wave field including the nearbed currents related to vertical variation of the current field.
- Sediment transport and bed level update model to simulate the transport of non-cohesive sediment by the action of waves and currents and calculate resulting changes in bed level.

The modules are fully coupled with varying update intervals, and in this work they are set as follows:

- The wave model has one-hour update cycle. Wave forcing and wave-induced mass flux are passed to current module. Near bed RMS orbital velocity passed to sediment module.
- The current module has a six-minute update cycle. Currents are passed to wave model.
- The sediment module has a six-minute update cycle and the bed level is updated from a representative sediment flux over the preceding six minutes. New bed level is passed to wave module and current module.

The model can be run in a non-updating mode, in which sediment transport and rate of bed level change is calculated and stored, but the model bathymetry is left unchanged. This is a useful option for long term simulations of general sedimentation transport pathways, without the unrealistic divergence that can occur due to the non-linear feedback between waves, currents and morphology and the models' inability to fully and correctly represent these interactions.

4.2 Wave module

A modified version of SWAN is used as the wave model. The code has been changed to allow update of both bed level and currents to be passed into SWAN at each wave model update cycle. The wave forcing as calculated internally by SWAN is also passed back to the current module, and the nearbed orbital velocities are used in the sediment transport calculations. None of the numerics or coding related to the physics has been altered.

The wave boundary conditions are fully nested spectral boundaries from the local scale wave hindcast described in Section 2. This approach retains the local effects of White Island on the wave field.

The model parameterizations in Table 3.1 have been used (described in the SWAN manual). The roughness length of 0.01 for the wave model has been found to be appropriate in several previous wave modeling studies.

Table 4.1 Wave model parameters.

Parameter	Value
Friction	Madsen, roughness length 0.01m
Quadruplet nonlinear transfer	None
Wind	None
Diffraction	Off
Setup	Direct feedback from current module
Currents	Direct feedback from current module
Triad	Off

4.3 Current module

The current module solves the equations governing the depth averaged nearshore current flow in orthogonal curvilinear coordinates,

$$\frac{\partial \varsigma}{\partial t} + \frac{1}{J}\frac{\partial}{\partial x_\alpha}\left(JV^\alpha h\right) = 0$$

$$\frac{\partial V^\alpha h}{\partial t} + \frac{1}{\sqrt{g_0}}\frac{\partial}{\partial x_\beta}\left(V^\alpha V^\beta h\right) + \left(V^\gamma V^\beta h\right)\Gamma^\alpha_{\gamma\beta} = \tag{4.1 a,b}$$

$$-ghg^{\beta\alpha}\frac{\partial \varsigma}{\partial x_\beta} + F^\alpha - \frac{1}{\sqrt{g_0}}\frac{\partial}{\partial x_\beta}T^{\alpha\beta} - T^{\gamma\beta}\Gamma^\alpha_{\gamma\beta} - \frac{1}{\rho}\tau^\alpha_B$$

where V^α is the contravariant depth-averaged velocity vector, ς is the wave-averaged surface elevation, F^α is the forcing due to the incident wavefield, $T^{\alpha\beta}$ is the Reynold's stress tensor, and τ^α_B is the bottom shear stress. g_0 is the determinant of the metric tensor in the curvilinear coordinate system, x_α, and $\Gamma^\alpha_{\beta\gamma}$ is the Christoffel symbol of the second kind.

The current module is based on the curvilinear version of SHORECIRC as described in Shi *et al*. (2003) and Shi *et al*. (2007). SHORECIRC solves the shallow water equations describing the wave and depth-averaged nearshore current field on a curvilinear grid. The radiation stress gradients in the incident wave field are imposed as forcing terms in the equations, obtained from the wave module. Bottom friction is parameterized with a standard drag coefficient approach:

$$\tau_B^{\alpha} = c_f V^{\alpha} \left| V^{\alpha} \right| \tag{4.2}$$

In the absence of data for calibration, a uniform drag coefficient of $c_f = 0.005$ is applied throughout.

The depth-averaged Reynolds stress tensor is given by,

$$T^{\alpha\beta} = h\nu_t \left(g^{\gamma\beta} u^{\alpha}_{,\gamma} + g^{\gamma\alpha} u^{\beta}_{,\gamma} \right) \tag{4.3}$$

with the horizontal eddy viscosity, ν_t, approximated by a Smagorinsky type scheme.

The numerical solution of eqs. 4.1 a,b uses the mode-splitting ADI method described in Shi *et al.* (2007). This method renders the gravity wave mode unconditionally stable. An adaptive timestep has been implemented to keep the vorticity mode Courant number within the stable limit. The actual code used is loosely based on that distributed as part of the NEARCOM project[6].

The boundary conditions used in this work use specified surface elevations around all seaward boundaries. At the offshore open boundary, the elevation is specified as the tidal height, thereby allowing tidal variation to be included. For the cross-shore boundaries a wave induced increase to the base elevation is estimated by assuming a balance between the cross-shore component of incident wave forcing and setup so that for a coordinate axis *x* oriented cross-shore:

$$\eta(x) = \eta_0 + \int_0^x \frac{F_x}{gh} dx \tag{4.4}$$

where η_0 is the tidal elevation at the offshore limit of $x = 0$.

For velocity, two types of condition are used; a simple zero gradient condition at the open seaward boundary and specified current boundaries at the cross-shore boundaries. The latter boundary uses a Flather type condition as specified in equation 3.6. As with elevation a simple wave balanced assumption is made

[6] http://chinacat.coastal.udel.edu/~kirby/programs/nearcom/

that locally the friction balances the wave forcing. The alongshore flow normal to the boundary, V_n^b is then prescribed by:

$$V_n^b = \frac{F_n}{c_f \left| V_n^b \right|} \tag{4.5}$$

In the numerical scheme, the value of V_n^b in the denominator is applied from the current timestep.

Undertow is calculated for use in the sediment module with the near-bed flow given by:

$$u_{bc}^{\alpha} = V^{\alpha} - \frac{Q_w^{\alpha}}{h} - \frac{c_f^{wc} \left| \hat{u}_w \right| u_b^{\alpha} h}{3\nu_t} \tag{4.6}$$

where Q_w^{α} is the mass flux of the incoming wavefield, $\hat{u}_w$ is the RMS near-bed orbital wave velocity and ν_t the vertical turbulent eddy viscosity. The mass flux is composed of the Stokes drift component and an additional contribution of the breaking waves.

The breaking wave flux is modeled by a parametric 'roller' approach in which the mass of whitewater traveling with the wave is approximated by a bore. For any individual wave of height *H* and period *T*, the total mass flux due to breaking is given by,

$$Q_{br} = \frac{q_b H^2}{T} \tag{4.7}$$

where q_b is a constant ~ 1. The fraction of breaking waves follows the parameterisation of Battjes and Janssen (1978) used for wave energy dissipation in the wave module. This allows the breaking wave mass flux to be related to the breaking dissipation as:

$$Q_{br} = \frac{4 q_b D}{\rho g} \tag{4.8}$$

where the dissipation, D comes directly out of the wave module. The angle of the breaking wave mass flux vector is assumed to be the same as the peak spectral wave direction.

Three-dimensional dispersive mixing of the depth-averaged current due to undertow (Svendsen and Putrevu, 1994) is not included.

4.4 Sediment module

The sediment transport module uses a Bagnold type total load transport formulation for the total sediment volume flux vector, $\vec{q}$:

$$\begin{aligned}\vec{q} &= \frac{c_f \varepsilon_b}{\rho(s-1)}\left[\frac{1}{\tan\phi}|\vec{u}_b|^2\vec{u}_b - \frac{\tan\beta}{\tan\phi}|\vec{u}_b|^3\right] \\ &+ \frac{c_f}{\rho(s-1)}\frac{\varepsilon_s(1-\varepsilon_b)}{\omega}\left[|\vec{u}_b|^3\vec{u}_b - \frac{\varepsilon_s(1-\varepsilon_b)}{\omega}\tan\beta|\vec{u}_b|^5\right]\end{aligned} \tag{4.9}$$

where u_b is the instantaneous nearbed velocity, c_f is the bottom friction coefficient, ε_s and ε_b are the suspended and bedload efficiencies. The relative sediment density is s, $\tan\beta$ is the bottom slope, $\tan\phi$ is the sediment friction angle and ω is the representative settling velocity. The upper term represents bedload transport, while the lower term represents the suspended load transport.

Eq. (4.9) can be rewritten as:

$$\begin{aligned}\vec{q} &= \vec{q}' - C_z\nabla z \\ \vec{q}' &= \frac{c_f}{\rho(s-1)}\left[\frac{\varepsilon_b}{\tan\phi}|\vec{u}_b|^2\vec{u}_b + \frac{\varepsilon_s(1-\varepsilon_b)}{\tan\phi}|\vec{u}_b|^3\vec{u}_b\right] \\ C_z &= \frac{c_f}{\rho(s-1)}\left[\frac{1}{\tan\phi}|\vec{u}_b|^3 + \frac{\varepsilon_s(1-\varepsilon_b)}{\omega}|\vec{u}_b|^5\right]\end{aligned} \tag{4.10}$$

which splits the expression into the total transport terms and the bedslope terms, where ∇z is the gradient of the bedslope elevation.

A parametric approach is used to calculate the instantaneous nearbed wave velocity for use in Eq (4.9). The time variation of orbital velocities follows the

method of Elfrink et al. (2006), with a single representative wave period and height corresponding to the local spectral values of H_s and T_p. A local bed slope is also applied for the calculation of the Irribarren number, which a key parameter in the method. The local spectral U_{rms} value is used as an equivalent orbital velocity and corresponds to $0.5U^*$ in Elfrink et al.'s formulation.

The bed level update solves the equation:

$$\frac{\partial z}{\partial t}+\frac{1}{\sqrt{g_0}}\frac{\partial \sqrt{g_0}\left\langle q'^{\alpha}\right\rangle}{\partial x_\alpha}=\frac{1}{\sqrt{g_0}}\frac{\partial}{\partial x_\alpha}\left(\sqrt{g_0}C_z g^{\alpha\beta}\frac{\partial z}{\partial x_\beta}\right) \qquad (4.11)$$

where z is the bed level. The terms $\left\langle q'^{\alpha}\right\rangle$ is the wave-averaged sediment flux vector, which is calculated by numerical integration over 50 wave phase steps. The WENO scheme described in Long *et al*. (2007) is used for the advection terms in Eq. (4.11), which controls the spurious oscillations often experienced with numerical solution of the sediment continuity equation.

4.5 Qualitative validation for idealized tombolo case

A qualitative validation of the fundamental model dynamics has been carried out for a classic tombolo formation example. The purpose of this exercise is simply to demonstrate that the model reproduces the morphological changes normally observed and produced by numerical models for a well understood configuration.

A plane beach with a breakwater is allowed to evolve under the action of a constant wavefield. The initial depth was set up with beach slope of 1:40, and a breakwater 300 m long situated 200 m offshore (Fig. 4.1). A grid with uniform spacing of 5 m and dimensions 81 by 225 was used.

The input wave spectrum has significant wave height of 2.0 m, peak period of 8 s, directional spreading of 10 degrees and with mean direction perpendicular to the beach. A skew factor of 0.05 was used for the wave orbital velocity, and sediment transport parameters: c_f =0.01, ε_s=0.015, ε_b=0.135, s = 2.65, tan ϕ =0.65 and ω= 0.00022 m/s. The deep water boundary was an open fixed level

boundary. The boundaries cross-shore boundaries are open, responding to wave setup and allowing free flow of longshore currents.

The bathymetry was allowed to evolve for 1000 hours. The resulting bathymetries at 50, 200 and 1000 hours are shown in Figure 4.2. The simulated breakwater configuration and incident wave conditions are very similar to those used for comparison in Nicholson *et al.* (1997), and so allow for comparison with other morphological model simulations. The general response is as expected, with the formation of a tombolo on the landward side of the breakwater, and the resulting morphology corresponds to the cases compared in Nicholson *et al.* (1997). One point of difference is the formation of a bar/trough formation with rip channels after a long time period of 900 hours. This is presumably the result of the inclusion of undertow in the model dynamics, and certainly corresponds to observations in nature of the general response of a planar beach with slope of 1:40.

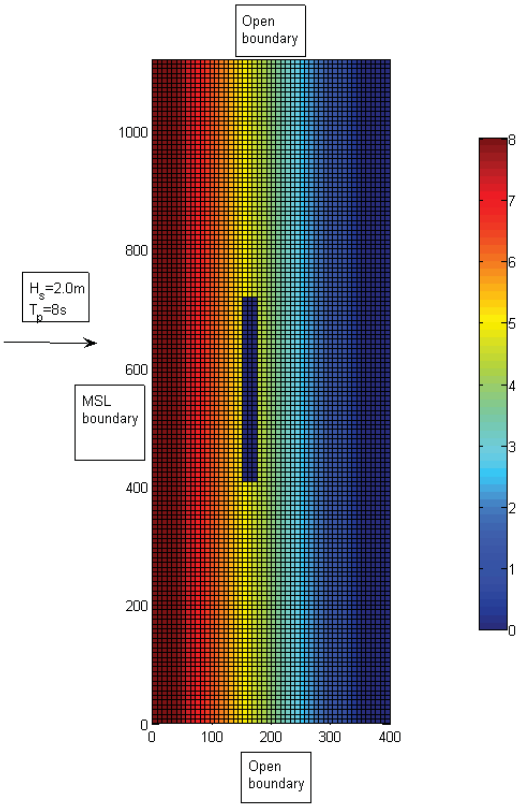

Figure 4.1 Initial depth for the idealised tombolo test.

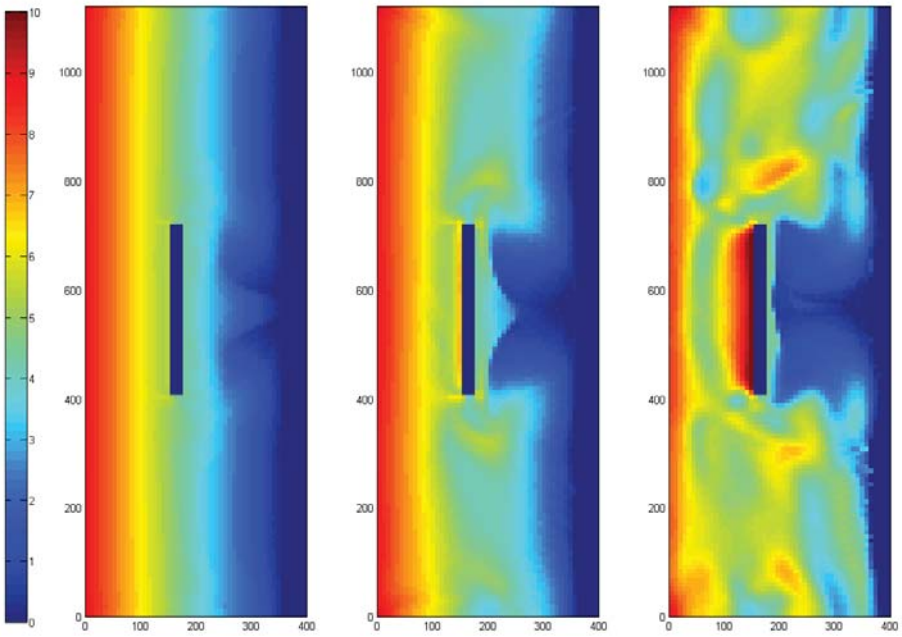

Figure 4.2 Bathymetry from tombolo test after 50, 200 and 900 hours.

4.6 Model domain and configuration

A curvilinear model grid, shown in Figure 4.3 was used which covered all of ocean beach with cross-shore boundaries at the headlands at either extremity. The grid dimensions were 200 by 160 in the alongshore and cross-shore dimensions. The grid size ranged from around 2 to 30 m, with the higher resolution concentrated in the shallower nearshore zones.

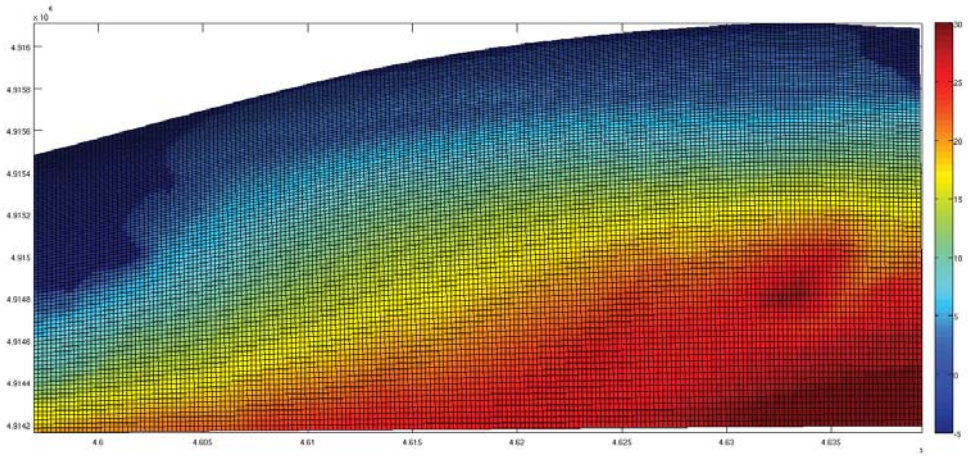

Figure 4.3 Morphological model grid with depth.

The model was run with water level elevations varying with the tide, and without current flow (in addition to the wave balanced flux) into the nearshore model domain from the open ocean.

4.7 Initial bathymetry

The December 2008 hydrographic survey provided good quality data at sufficient density to allow the significant nearshore bathymetric features to be resolved. The bathymetry surface is presented in Figure 7.1, showing the depths from 0-5 m (CD). Several important features can be noted from this map.

At the time of the survey the beach exhibited a well-defined bar system for most of its length. Along the western third of the beach, the bar is a continuous, linear feature, with the mean crest elevation positioned at around 2 m depth (below MSL). Immediately east of Moana Rua Rd, the bar crest becomes deeper, with a mean depth of 3 m along the central third of the beach. In this region, the linear bar arrangement becomes disrupted. Along the eastern third of the beach, the bar crest depth is more variable (1.6 - 2.8 m below MSL) and the bathymetry exhibit classic rip cell morphologies, with a series of cross-shore channels and bars. A series of representative nearshore bathymetry profiles along the beach are shown on Figure 7.1, clearly illustrating the bar / channel morphology.

It is notable that the western third of the beach, with the linear bar morphology and the shallowest and bar crest depths, also corresponds to the region of wave sheltering due to the offshore bathymetry. However, it is unknown at this time if the December 2008 survey data are representative of the typical subtidal profiles along Ocean Beach, and if the linear bar morphology is merely an ephemeral feature.

In the absence of subtidal data for other periods, including the tested scenarios, the same initial bathymetry was used for all simulations. It should be noted that this strongly preconditions the beach response for the particular initial conditions, and that this may not correspond to what existed at the time of the specific modeled periods.

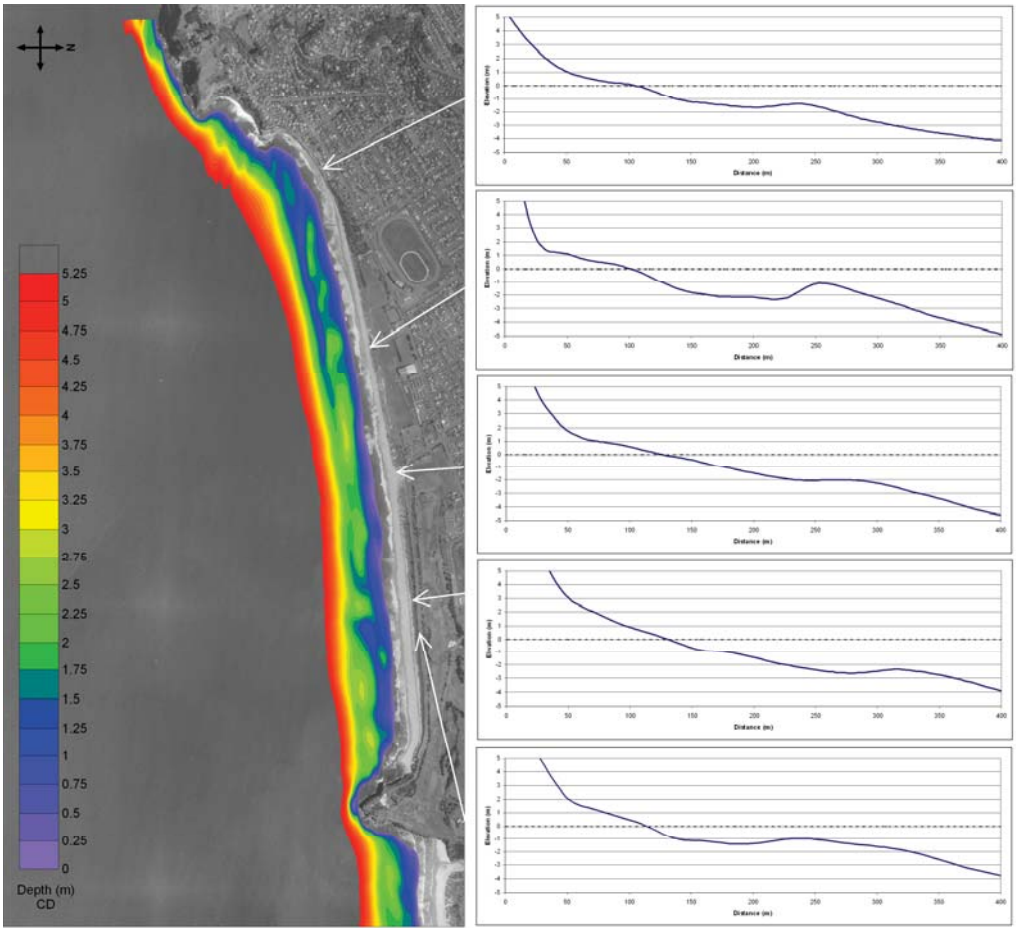

Figure 4.4 The nearshore bathymetry at Ocean Beach, from 0-5 m depth (CD), and 5 representative cross-shore depth profiles.

4.8 Sediment transport modeling scenarios

Sediment transport and morphology simulations have been undertaken for four discrete periods. The first is an energetic period from April to September in 2007, which included several periods of severe erosion along Ocean Beach. The second is the six-month period immediately preceding this period (October 2006 – March 2007), selected for contrast. The third is from January to March 2009, and the fourth from July – September 2009, during which beach building was observed. A series of beach surveys were carried out during the 2009

period, which allow a direct comparison of modeled and measured changes to the upper and inter-tidal zones.

For the long period winter and summer simulations, the model was run in a non-updating mode for the bed level. For the two 2009 periods, the bathymetry was allowed to evolve.

Within the winter period, three significant storms were modeled as discrete events, using the model in an updating mode, and starting in each case from the same initial bathymetry based on the December 2008 hydrographic survey (e.g. Fig. 4.3). The storm dates were 12-13 April, 16-17 May and 22-27 June. These events represent typical periods with large southerly swell and sea that result in the highest energy conditions on the beach. Fortunately, visual assessment of changes to the beach face and subtidal bathymetry were available for these events (DTec, 2009). One other period from 1-4 August 2007, with high energy southeasterly waves, was also modeled as a discrete event for contrast. Wave statistics for an offshore location in 35 m depth (as used for section 5.3) over these periods are presented in Table 7.1.

In addition to the study periods, the model was also run for February and March 2010, for the purposes of comparing the modeled surf zone currents with observations of signal buoys (Section 7.2).

Table 4.2 Wave statistics from offshore Ocean Beach (170.5222˚E - 45.9145˚N) during each of the modeled events.

Scenario	Period	Mean H_s [m]	Max H_s [m]	Mean D_p [deg]	Mean T_p [s]
Winter	1 April 2007- 17 Aug 2007	1.55	6.02	179	11.7
Summer	3 Oct 2006-14 Mar 2007	1.25	3.33	183	11.0
2009a	14 Jan 2009-14 Mar 2009	1.43	4.29	176	11.0
2009b	26 Jul 2009 – 28 Sep 2009	0.94	2.99	172	12.5
Storm 1	12-14 April 2007	3.66	5.3	181	13.0
Storm 2	16-18 May 2007	2.93	3.95	179	12.9
Storm 3	22-27 June 2007	4.4	6.0	176	12.8
SE event	29 July - 4 Aug 2007	2.2	3.8	136	10.9

5 WAVE MODELLING RESULTS

5.1 Validation

The hindcast wave model outputs have been validated with wave buoy data from numerous locations around New Zealand (ranging from 10-110 m depths). Validation results using measured waverider data from just offshore of Ocean Beach during January – May 2007 are presented here to illustrate the ability of the hindcast technique to accurately replicate the wave conditions in this part of New Zealand. The waverider was moored in approximately 15 m depth some 1.2 km offshore of the Tahuna Wastewater Plant.

A timeseries validation plot of the measured and hindcast total significant wave heights is presented in Figure 5.1, showing that the numerical model is faithfully representing the periods of high and low energy. The measured and hindcast wave data have similar statistical means (1.40 m and 1.32 m, respectively). Linear regression of the measured and hindcast wave heights has an R^2 correlation coefficient of 0.85 (Fig. 5.2).

Further quantitative measures of the accuracy of the hindcast are calculated from the measured, x_m and hindcast, x_h, data. These are defined as:

Mean absolute error: $\overline{|x_h - x_m|}$ (5.1)

RMS error: $\sqrt{\overline{(x_h - x_m)^2}}$ (5.2)

Mean relative error: $\overline{\left|\frac{x_h - x_m}{x_m}\right|}$ (5.3)

Bias: $\overline{x_h - x_m}$ (5.4)

where the line indicates an average over all pairs of measured/hindcast data.

The results for the comparison of the significant wave heights for the year 2000-2001 are presented in Table 5.1. The mean absolute error (MAE) is the most

direct representation of the typical deviation of the hindcast from the measured value. The RMS error exaggerates large differences in measured and hindcast wave heights and is therefore larger than the MAE. The mean relative absolute errors are an expression in percentage terms of the error compared to actual, and shown that the hindcast total significant wave heights are on average within 21% of the measured values. The bias, which represents a constant 'offset' in the hindcast significant wave heights, indicates that overall the model slightly under predicts the total significant wave heights by 7 cm. Total significant wave heights are very sensitive to local wind conditions, and the full spatial and temporal variability in the local wind field is not always captured by the Blended Wind product. Also, some of the error in the hindcast wave heights is due to timing of the wave events, as the hindcasting technique has an inherent phase resolution of ~3 hours.

Table 5.1 Accuracy measures for hindcast total significant wave heights. MAE: mean absolute error, RMSE: RMS error, MRAE: mean relative absolute error, BIAS: bias.

MAE (m)	RMSE (m)	MRAE (%)	BIAS (m)
0.27	0.35	21	-0.07

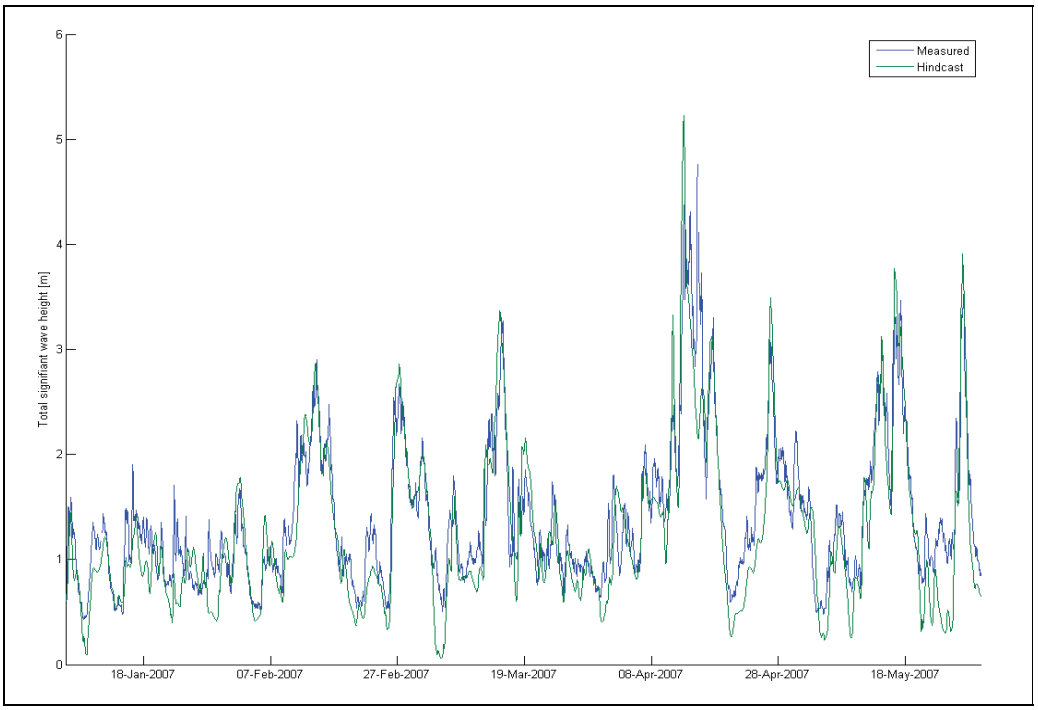

Figure 5.1 Timeseries validation plot of the measured significant wave heights near Dunedin and the nearest node from the hindcast model.

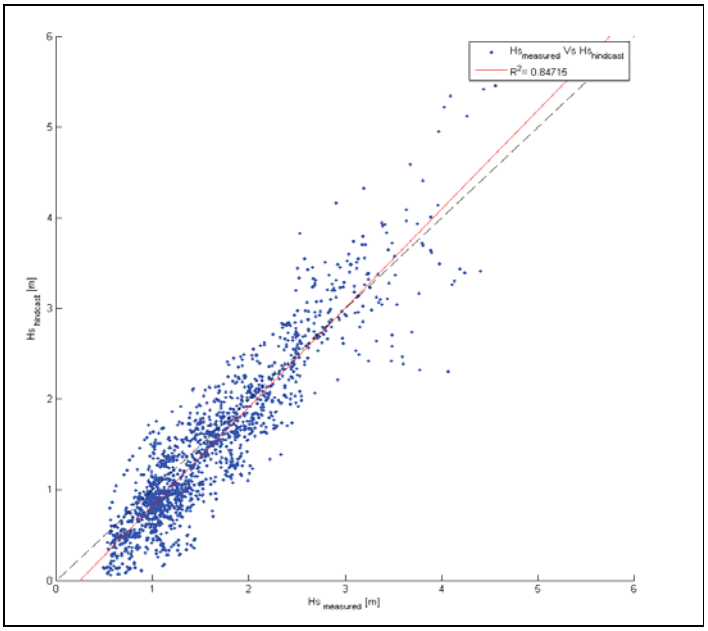

Figure 5.2 Regression plot for measured and hindcast total significant wave heights.

5.2 Regional wave climate

The 10-year hindcast has been used to create summary maps of the wave climate over the wider Dunedin region. The mean significant wave height is presented in Figure 5.3; showing clear gradients in the wave energy. On average, wave heights increase from the south-western region towards the Otago Peninsula. The 99th percentile non-exceedence level exhibits a very similar pattern (Fig. 5.4). The maximum observed significant wave height (Fig. 5.5) is defined from several storms, and has a similar energy gradient to the mean wave heights, with the largest wave heights occurring along the coastline just south of Cape Saunders. Significant wave heights exceeding 8 m were hindcast for the inner shelf regions over the period 1998-2007. The average peak spectral wave period is presented in Figure 5.6; this remains uniform in the vicinity of Ocean Beach and along the coastline south of Cape Saunders. Examples showing wave heights during typical events are provided in Figures 5.7 and 5.8.

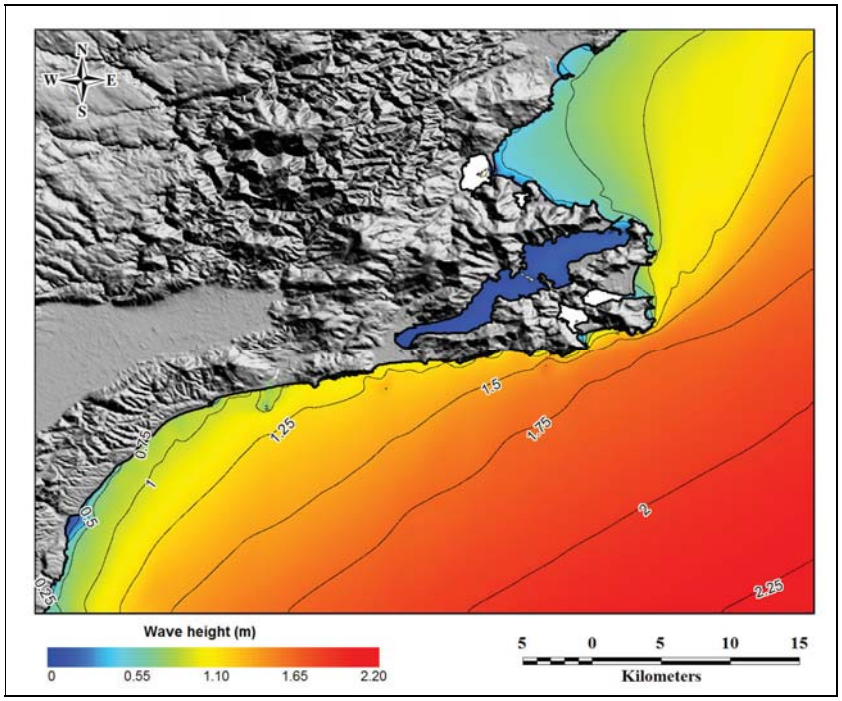

Figure 5.3 Mean significant wave height (1998-2007).

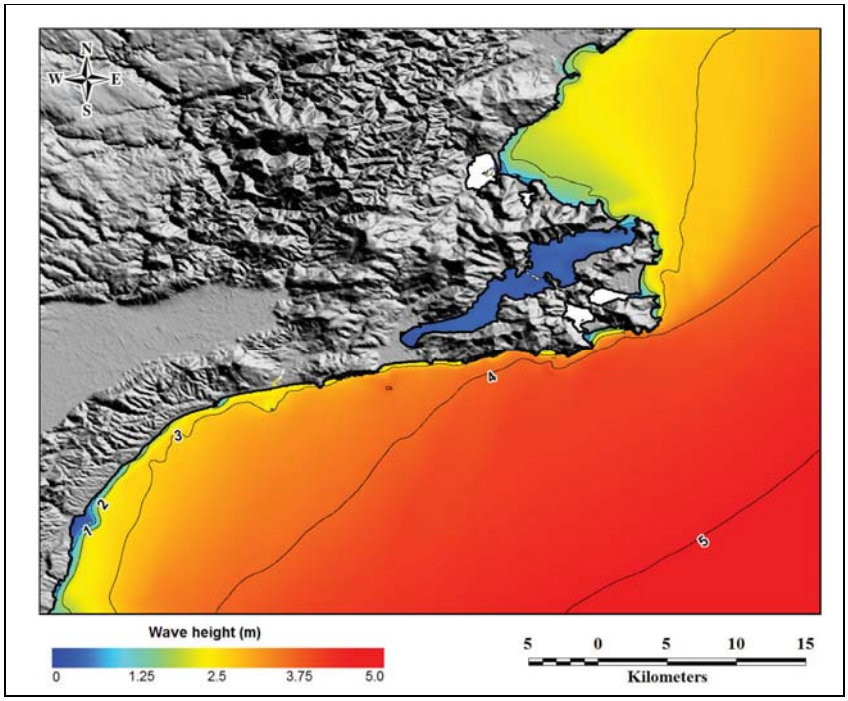

Figure 5.4 99th percentile non-exceedence significant wave height (1998-2007).

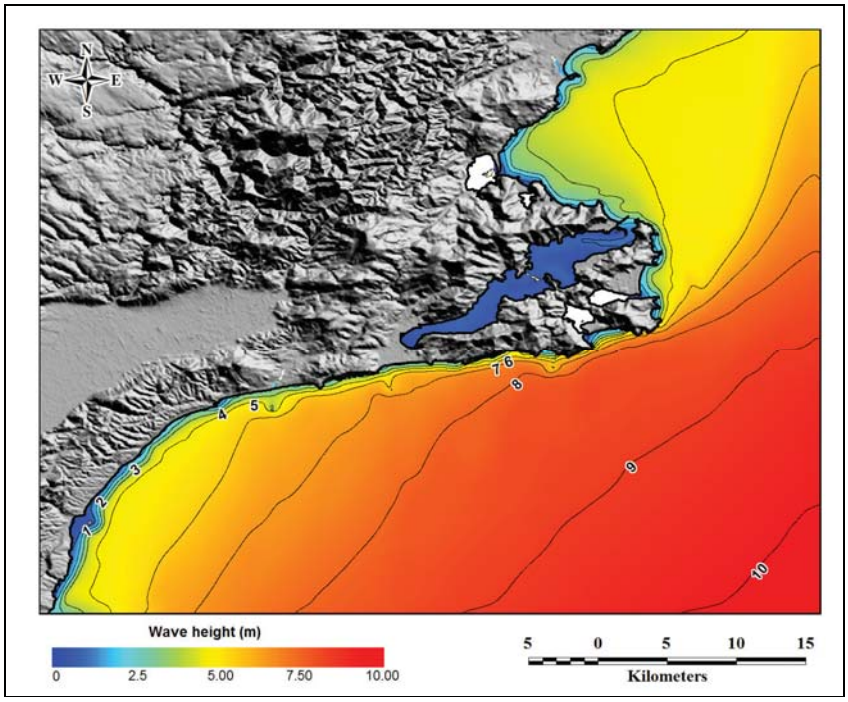

Figure 5.5 Maximum significant wave height (1998-2007).

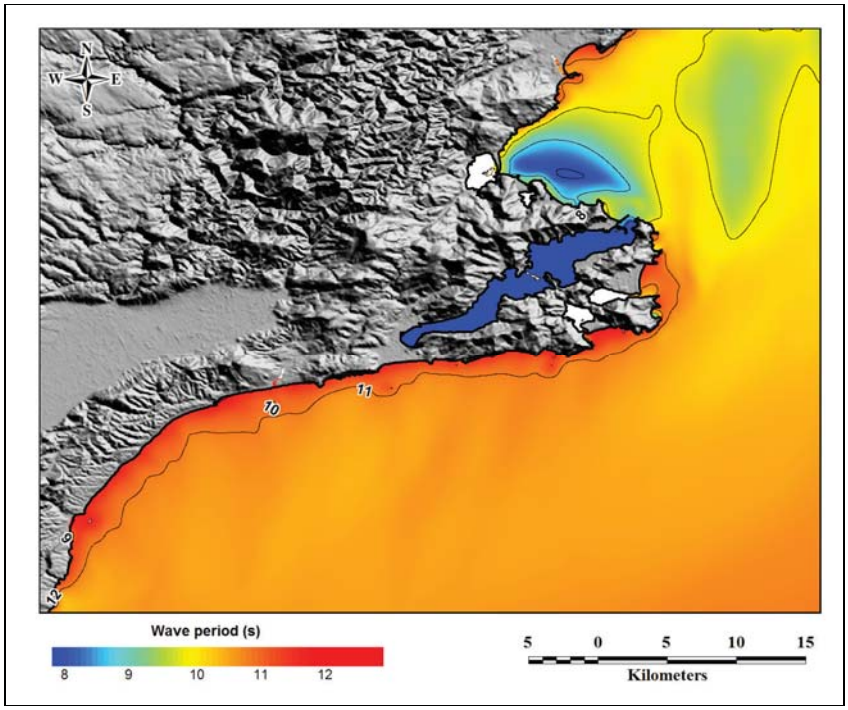

Figure 5.6 Average peak spectral wave period (1998-2007).

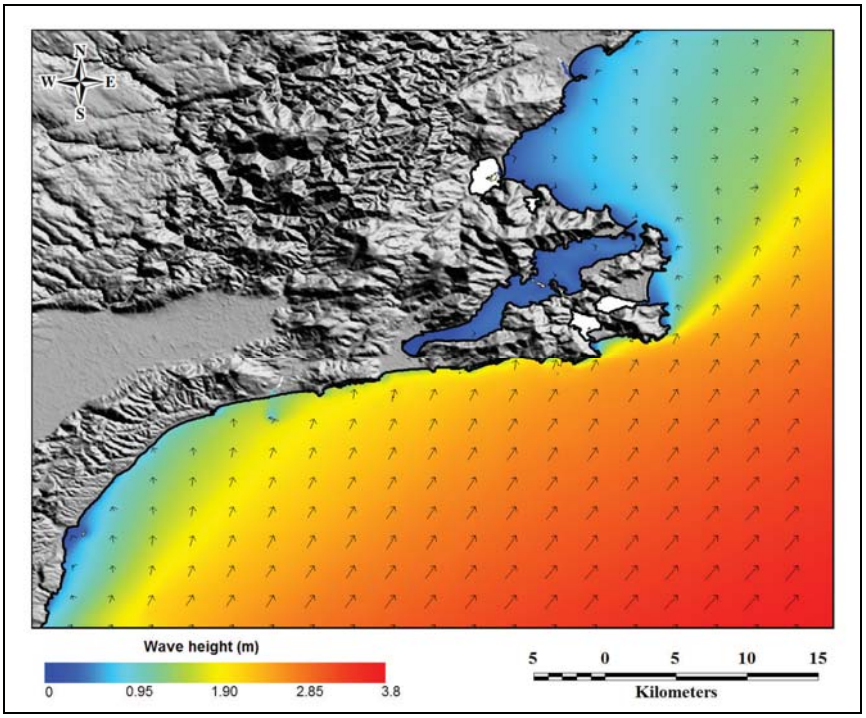

Figure 5.7 Example wave height distributions for a characteristic event from the southeast.

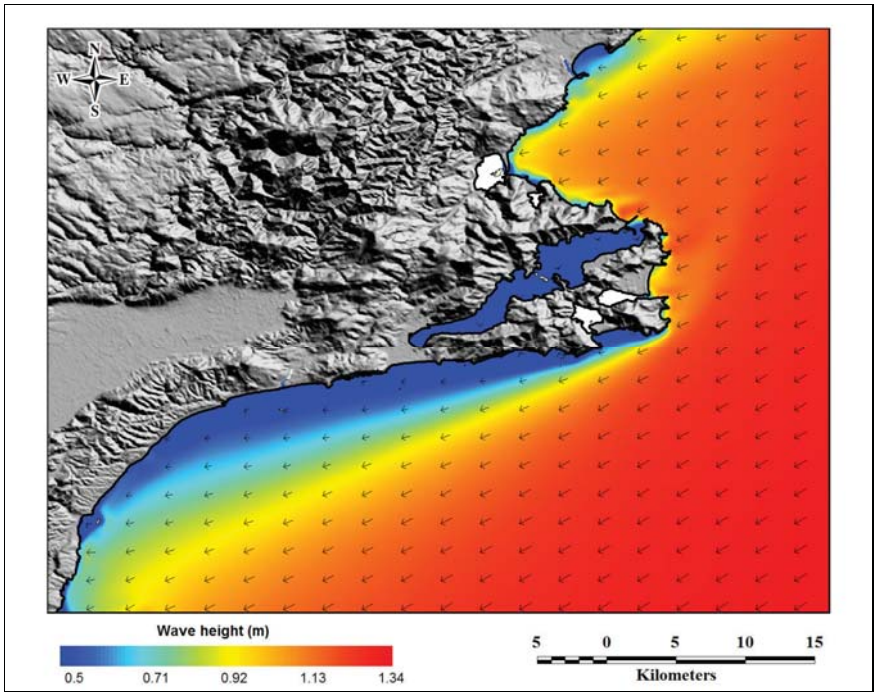

Figure 5.8 Example wave height distributions for a characteristic event from the northeast.

5.3 Ocean Beach wave climate

Summary maps of the wave climate from the 10-year hindcast of the wave conditions are presented and discussed in this section. The mean significant wave height is provided in Figure 5.9, clearly showing the effect of the offshore White Island and the surrounding bathymetry. The combined effects of wave refraction and seabed friction give rise to a wave energy shadow in the lee of the Island, extending from St Clair to approximately St Kilda beach. The 99th percentile non-exceedence level exhibits a very similar wave height pattern (Fig. 5.10), with a zone of higher wave energy clearly evident between Lawyers Head and St Kilda. This region of elevated wave height is due to focusing by wave refraction on the offshore bathymetry. The focusing effect is also evident in the maximum observed significant wave heights (Fig. 5.11).

Significant wave heights exceeding 7 m were hindcast for the nearshore region over the period 1998-2007. Notably, the maximum wave height map (Fig. 5.11) shows a high degree of sheltering in the lee of the White Island subtidal structure, however depth-limited conditions become apparent all along Ocean Beach at approximately the 4 m

maximum wave height contour. The average peak spectral wave period is presented in Figure 5.12, and these subtle patterns in wave period indicate that wave refraction around the White Island bathymetric structures area an important process along Ocean Beach. Examples of the wave height distribution during wave events from the northeast and the southeast are provided for comparison in Figures 5.13 and 5.14.

Wave height statistics have been analysed for a representative location offshore of Ocean Beach at 170.5222˚E -45.9145˚N, beyond the influence of White Island in 35 m water depth. The monthly and annual significant wave height statistics are provided in Table 5.2. Within the hindcast time-series, the Years 2002, 2004 and 2007 stand out as being energetic, as indicated by the higher percentile exceedence values for significant wave height (e.g. P95 and P99).

The joint probability distribution of significant wave height and peak wave direction is presented for the annual and seasonal conditions in Appendix One. These tables show that the largest wave events consistently approach from the southerly octant. During the winter months, high-energy wave events can also approach from the easterly sector. The joint probability distribution of significant wave height and peak wave period is presented for the annual and seasonal conditions in Appendix One. The energetic wave events tend to have peak spectral wave periods of 10-15 s. The hindcast data indicate a higher percentage of wave conditions with shorter periods (i.e. <10 s) during the summer months, while the winter months exhibit a higher percentage of wave conditions with longer periods (i.e. 12-16 s) and swell-dominated sea states.

The annual wave height non-exceedence and exceedence persistence matrices are provided in Appendix One. These tables indicate the percentage of time (on an annual basis) that the significant wave heights are above or below certain thresholds for durations of up to 72 hours. Such data provide useful context when considering storm thresholds and durations. For example, wave heights are greater than 2 m for durations of 6 hours or more for 17% of the time, and 72 hours or more 6% of the time. Similarly, wave heights are less than 2 m for durations of 6 hours or more for 34% of the time, and 16% of the time for durations of 72 hours or more. The monthly wave height exceedence statistics indicate suggest February can be very energetic; in this case due to a single storm event that produced the maximum wave height in the 10-year hindcast. Wave height extrema at 1-100 year return periods are provided in Table 5.3. The omni-

directional 100-year return period significant wave height at 35 m water depth is 9.22 m.

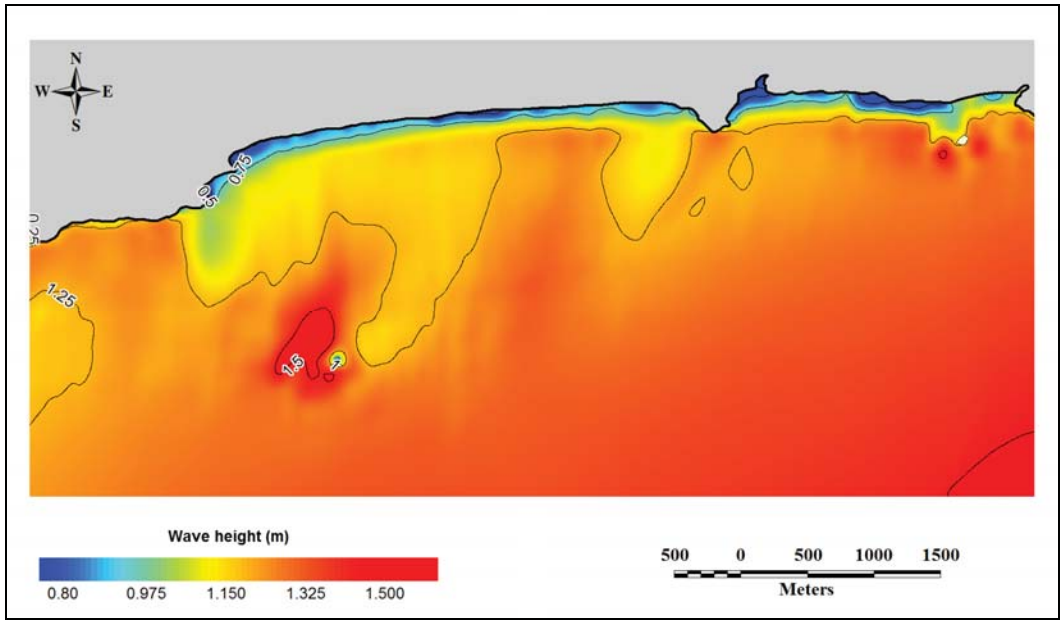

Figure 5.9 Nearshore mean significant wave height (1998-2007).

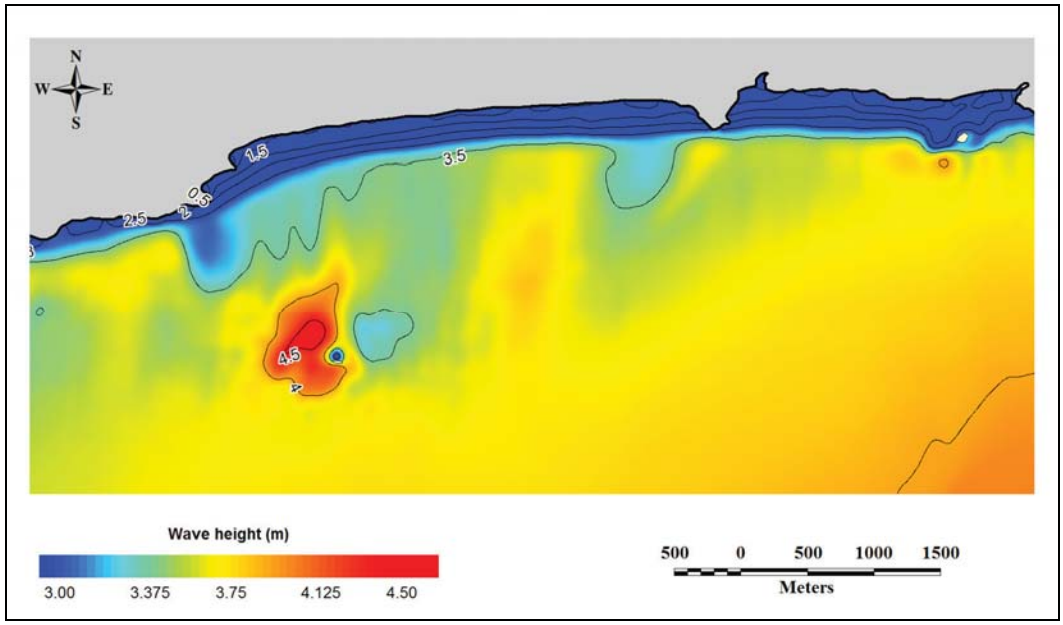

Figure 5.10 Nearshore 99th percentile non-exceedence significant wave height (1998-2007).

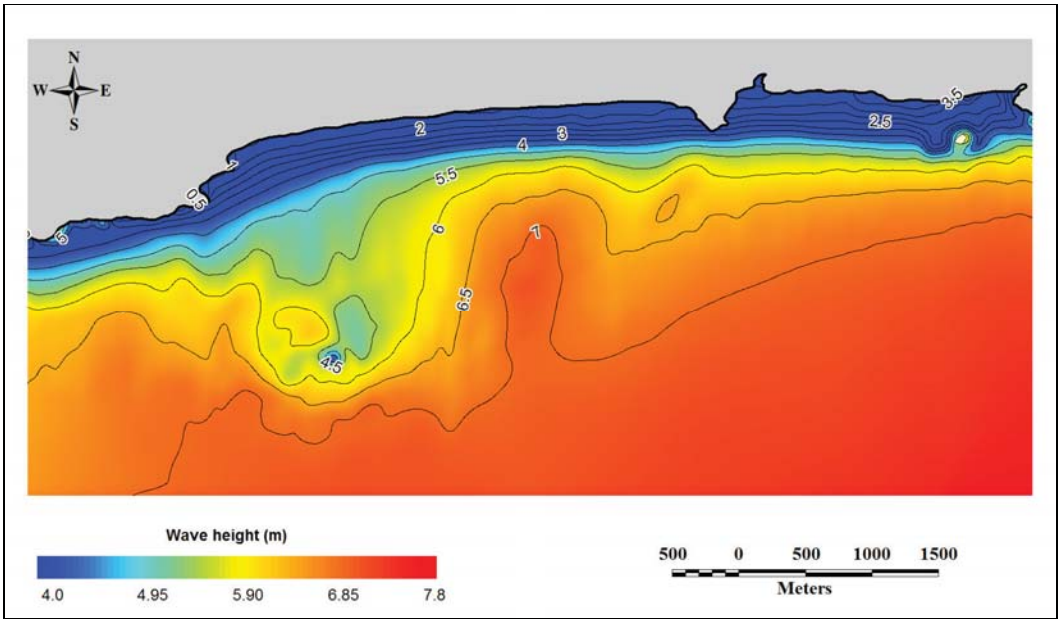

Figure 5.11 Nearshore maximum significant wave height (1998-2007).

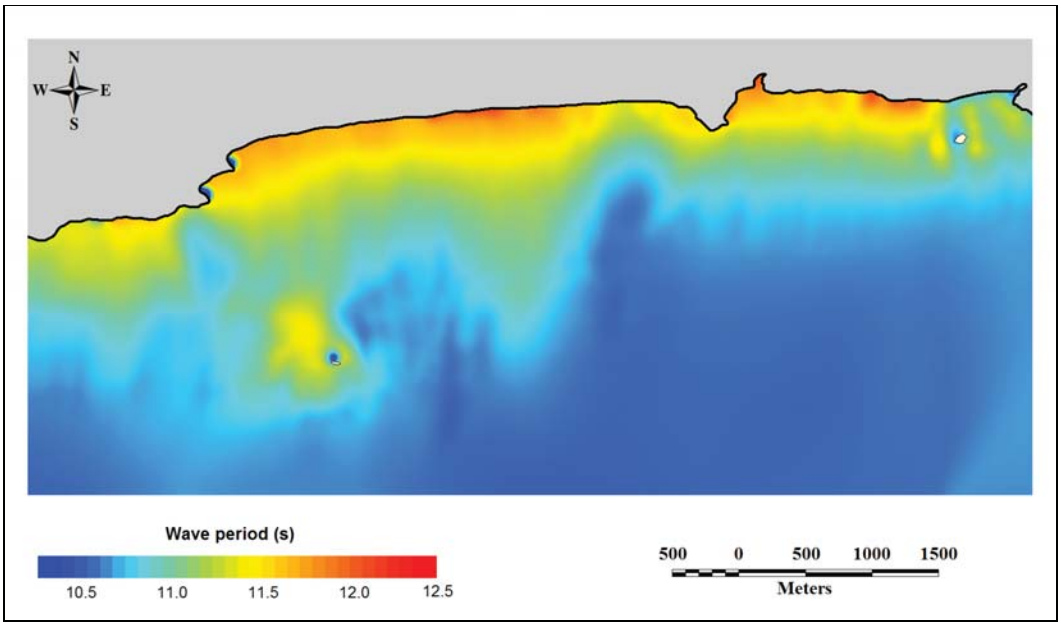

Figure 5.12 Nearshore average peak spectral wave period (1998-2007).

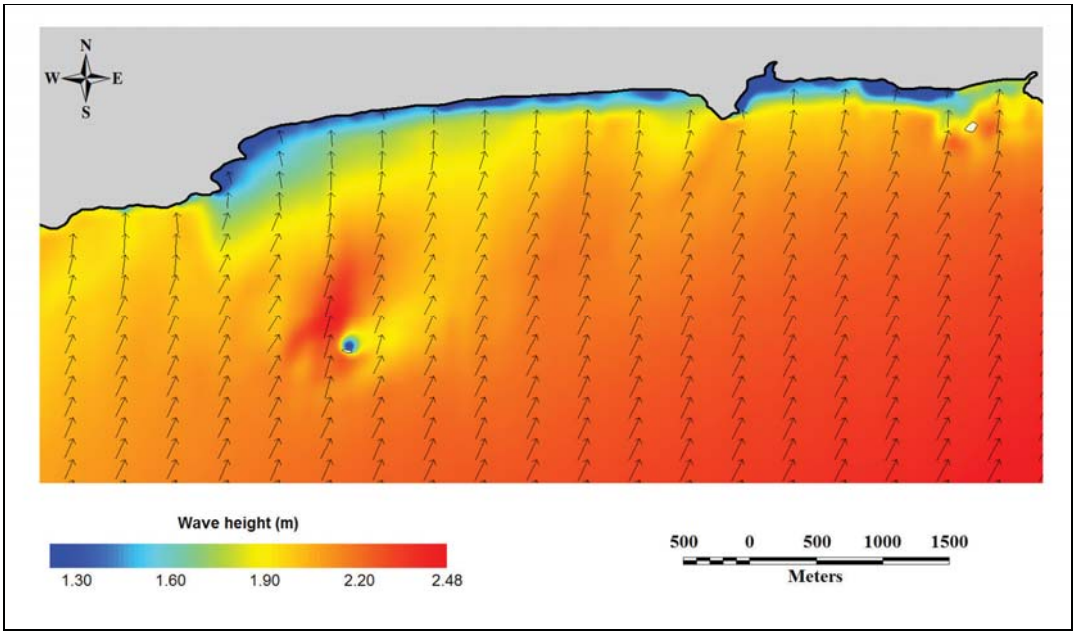

Figure 5.13 Nearshore example wave height distributions for a characteristic event from the southwest.

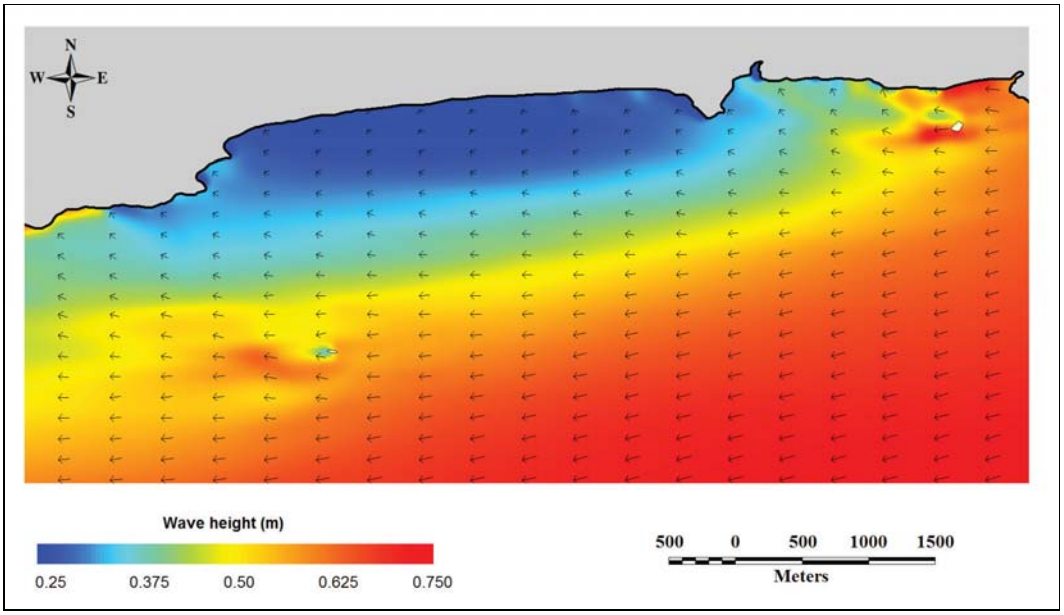

Figure 5.14 Nearshore example wave height distributions for a characteristic event from the northeast.

Table 5.2 Annual and monthly significant wave height statistics (35 m depth).

Period	Statistic					
	Mean (m)	Median (m)	P90 (m)	P95 (m)	P99 (m)	Max (m)
January	1.12	0.98	1.89	2.38	3.25	4.61
February	1.22	1.10	1.98	2.41	3.13	7.16
March	1.32	1.17	2.14	2.61	3.59	4.66
April	1.52	1.33	2.60	3.07	4.32	5.81
May	1.51	1.32	2.63	3.09	4.19	5.44
June	1.64	1.49	2.74	3.32	5.04	6.31
July	1.54	1.37	2.67	3.26	4.09	5.17
August	1.65	1.51	2.81	3.22	4.08	5.71
September	1.34	1.15	2.37	2.90	3.55	5.29
October	1.30	1.20	2.12	2.39	3.27	4.05
November	1.32	1.23	2.15	2.53	3.32	4.68
December	1.20	1.09	1.99	2.41	3.21	4.16
1998	1.31	1.16	2.19	2.62	3.27	3.84
1999	1.37	1.27	2.17	2.65	3.74	4.49
2000	1.33	1.16	2.23	2.73	3.81	5.30
2001	1.36	1.21	2.35	2.81	3.55	4.90
2002	1.47	1.23	2.67	3.15	4.14	5.71
2003	1.41	1.26	2.41	2.85	3.69	4.63
2004	1.52	1.30	2.69	3.19	4.29	7.16
2005	1.28	1.14	2.16	2.48	3.32	4.75
2006	1.43	1.30	2.37	2.79	3.61	5.81
2007	1.43	1.20	2.53	3.24	4.97	6.31
Annual	1.39	1.23	2.39	2.85	3.83	7.16

Table 5.3 Wave height extrema and associated wave periods at the 1-100 year return periods (35 m depth).

Parameter	Units		Return period (years)					
			1	5	10	25	50	100
Significant wave height	**Hs**	**m**	5.86	7.05	7.55	8.22	8.72	9.22
Maximum single wave	**Hm**	**m**	10.90	13.11	14.04	15.29	16.22	17.15
Period of Hm (min)	**Tass min**	**s**	8.73	9.57	9.91	10.34	10.65	10.95
Period of Hm (max)	**Tass max**	**s**	13.26	14.54	15.05	15.70	16.17	16.63

6 REGIONAL CURRENT MODELLING RESULTS

6.1 Validation

Current meter data from Ocean Beach were available for model validation. Over a two month period (19/07/2001 – 17/09/2001) current meters were deployed by the Cawthron Institute at locations in 20 and 30 m depth, directly offshore of the Tahuna Wastewater Plant. Hindcast current data have been output at these specific locations, and a timeseries comparison of the measured and modeled speeds and directions is presented for the 30 m depth site. Notably, the current meter data are a 3-minute average from a point-source, while the model is the hourly depth-averaged values.

The total currents (tidal and wind-driven flows) are presented in Figure 6.1, while the non-tidal (i.e. residual) currents are presented in Figure 6.2. In general, the measured and modeled currents show good agreement, particularly considering the relatively coarse model resolution for comparison with nearshore location. The dominant flows and periods of flow reversal are being captured by the model, along with the correct magnitudes, particularly for the high flow events. The tidal flows make up a relatively small fraction of the overall current variance at Ocean Beach.

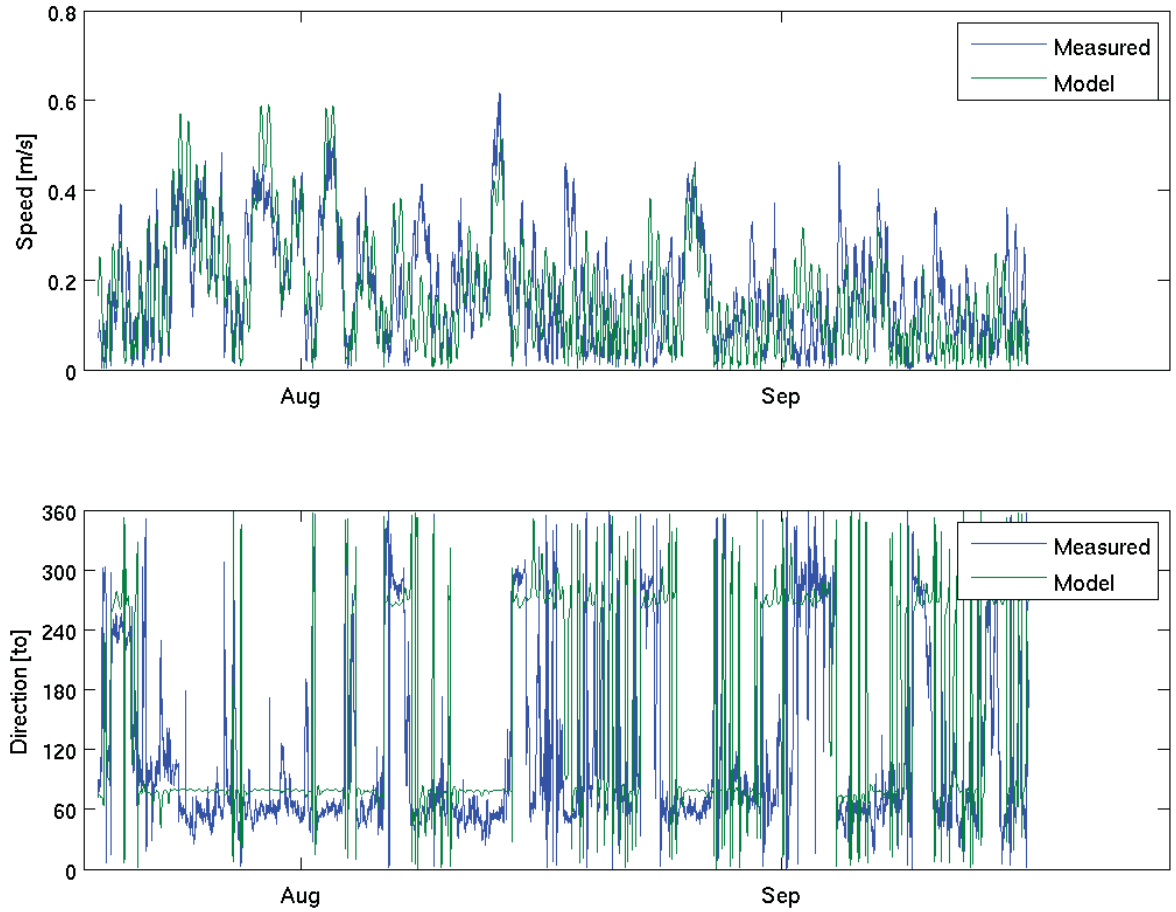

Figure 6.1 Timeseries validation plot showing the measured and modeled total current speeds and directions from 30 m depth offshore Tahuna in 2001.

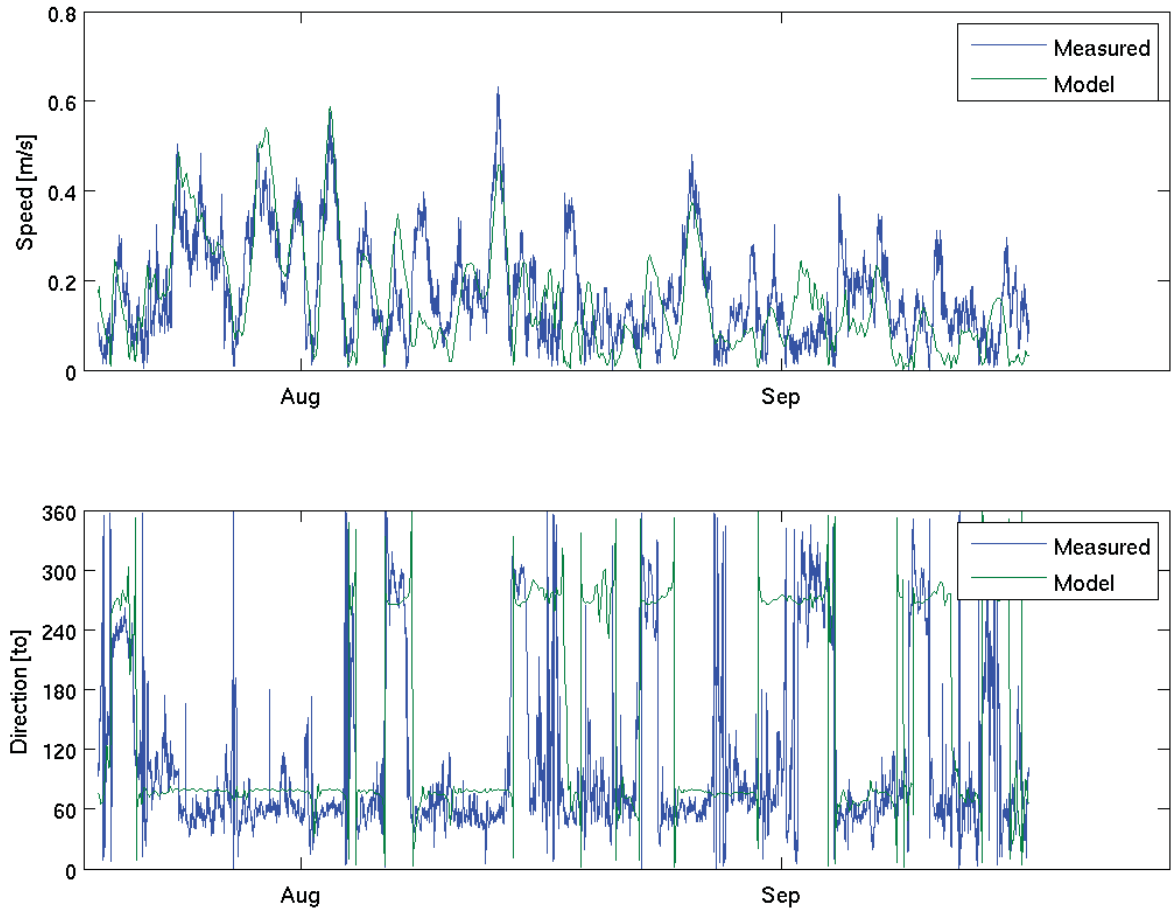

Figure 6.2 Timeseries validation plot showing the measured and modeled non-tidal current speeds and directions from 30 m depth offshore Tahuna in 2001.

6.2 Regional current setting

The mean regional current flow pattern is presented in Figure 6.3, showing the mean depth-averaged speed and direction (1998-2002). The current flows are predominantly directed to the north and northeast, with considerable acceleration of the currents evident in the vicinity of Cape Saunders and along sections of the southern Otago Peninsula (e.g. Allans Beach and Tow Rock). A clear zone of higher flows extends in a band to the southwest of the Cape, which is the local expression of the Southland Current. Moderate nearshore flows, directed to the east, extend from near Green Island to Smails Beach, with further strengthening eastward flows toward Allans Beach. From Brighton through to Tairei Mouth the mean nearshore flow regime is of comparatively lower energy. An example of the regional current flows under energetic conditions (03/02/1998) is provided in Figure 6.4. During this event the depth-averaged current speeds off Cape Saunders reached ~1.5 ms^{-1}, while the current speeds in regions north and south of the Peninsula were significantly less.

6.3 Ocean Beach current regime

Within the Ocean Beach region, the mean current pattern from the 5-year hindcast is presented in Figure 6.5. The mean currents are directed to the east and there is evidence of flow acceleration over the bathymetric sill that connects White Island to the shoreline west of the St Clair Headland. There are alongshore gradients in the current strength; strong mean eastward flows are evident along the coastline from Blackhead to St Clair, reduced flows exist along the Ocean Beach region, and then there is a further strengthening of the flows in the region east of Lawyers Head. An example of the depth-averaged flows under energetic conditions (i.e. 03/02/1998) is presented in Figure 6.6. Over the sill, easterly-directed currents of 0.6-0.8 ms^{-1} were hindcast, and a shadow zone can be seen to extend to the immediate east of the White Island bathymetric structures.

Timeseries current data have been analysed for two locations. Site C1 is positioned mid-beach beyond the line of the headlands (45.917643°, 170.512322°) in 10 m water depth, while Site C2 is located further offshore and beyond White Island in 35 m depth

(45.917643°, 170.512322°). Current roses for these sites are provided in Figures 6.7 and 6.8; clearly showing the predominantly alongshore flow regime and the strong bias to the eastward flow mode.

The current patterns directly offshore of Ocean Beach (i.e. Site C1) are of direct relevance to the study of local sediment dynamics. A joint probability distribution of total current speed and direction is provided in Table 6.1. This table quantifies the two directional flow modes shown on the rose plots, and indicates that 75% of all the current flows exceeding 0.1 ms^{-1} are directed to the east, including the highest flow conditions. The maximum hindcast current speed was 0.87 ms^{-1}, and the 95^{th} percentile exceedence level was 0.43 ms^{-1}. The tidal current signal is approximately symmetrical, with two alongshore flows modes (eastward and westward) of equivalent magnitude. The mean tidal current speed is 0.06 ms^{-1} and the maximum depth-averaged tidal currents are 0.18 ms^{-1}. Accordingly, tidal currents provide a relatively small contribution to the overall current variance at Ocean Beach.

6.4 Correlation of wave and current events

A joint probability distribution has been prepared to consider the coincidence of wave heights and current flows. The depth-averaged eastward velocity at Site C1 has been compared with the significant wave heights, also at Site C1, over the period 1998-2002. The results (Table 6.2) indicate that during stormy conditions, the ocean currents are typically directed to the east, and the highest current flows are all associated with energetic wave conditions. For wave events under 3 m in height and during current speeds exceeding 0.2 ms^{-1}, there are twice as many events with flows directed to the east compared with the westward flows. For conditions when significant wave heights exceed 3 m, there are 14 times as many events with eastward flows compared with westward flows.

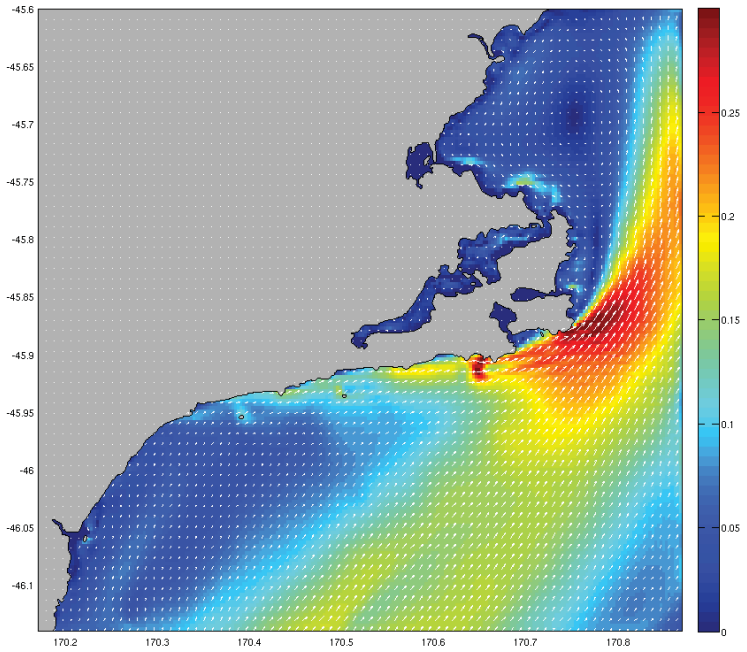

Figure 6.3 Mean depth-averaged flows (m/s) for the Otago Peninsula region (1998-2002).

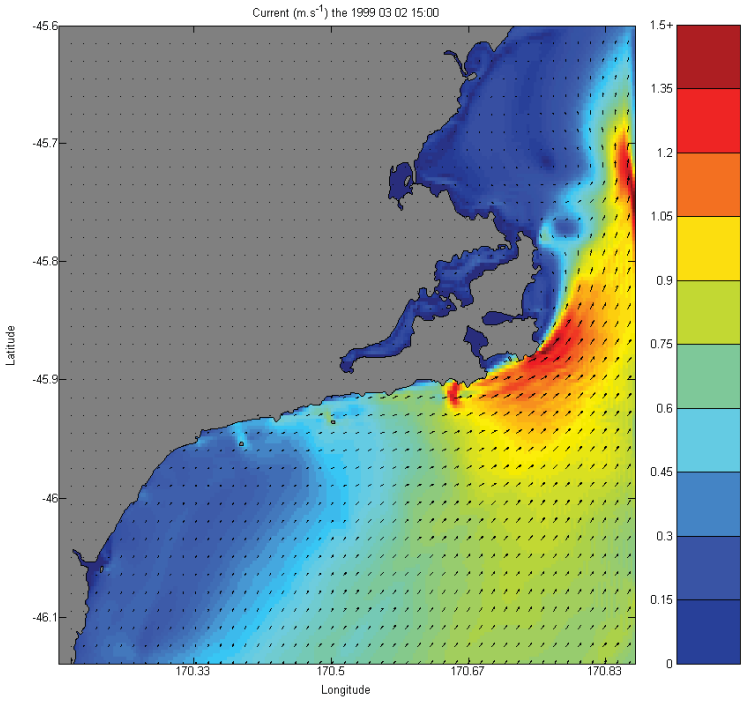

Figure 6.4 Depth-averaged flows (m/s) for the Otago Peninsula region (03/02/1998).

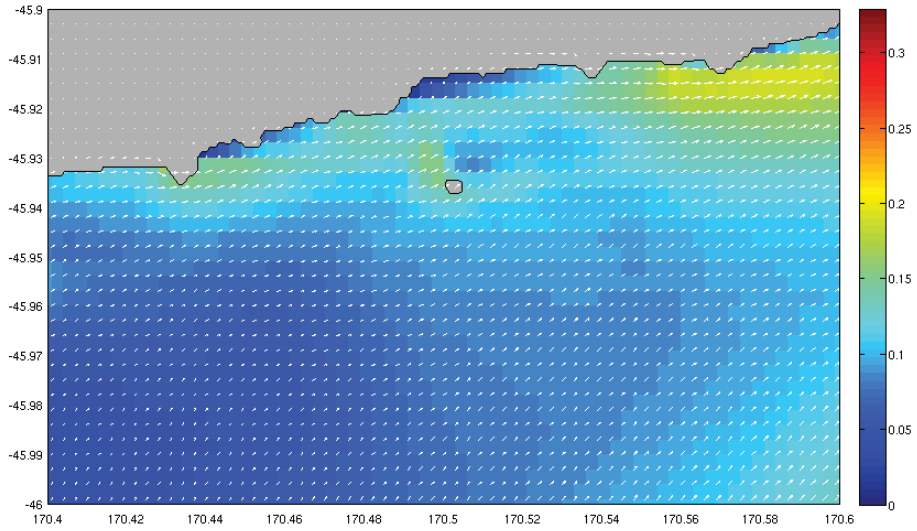

Figure 6.5 Mean depth-averaged flows (m/s) for the Ocean Beach region (1998-2002).

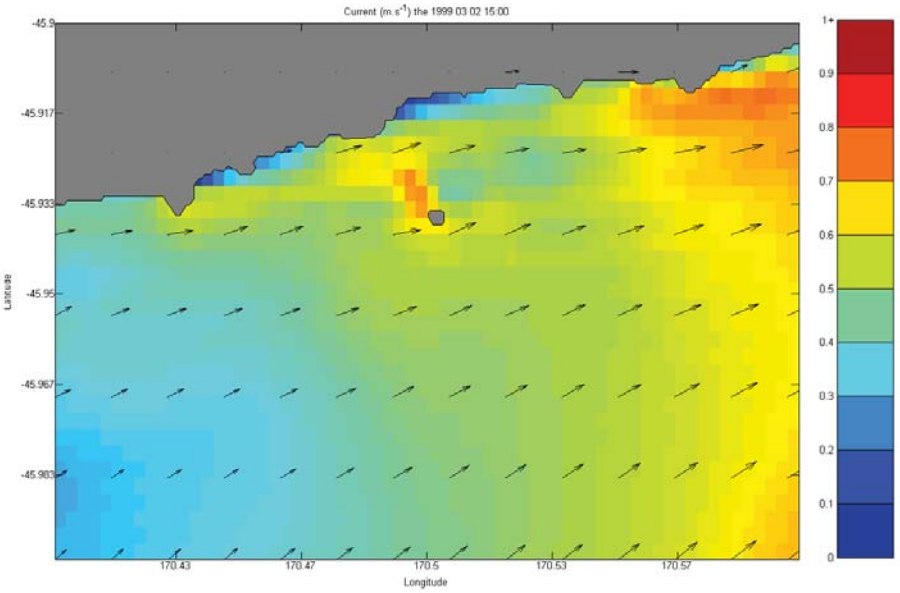

Figure 6.6 Depth-averaged flows for the Ocean Beach region (03/02/1998).

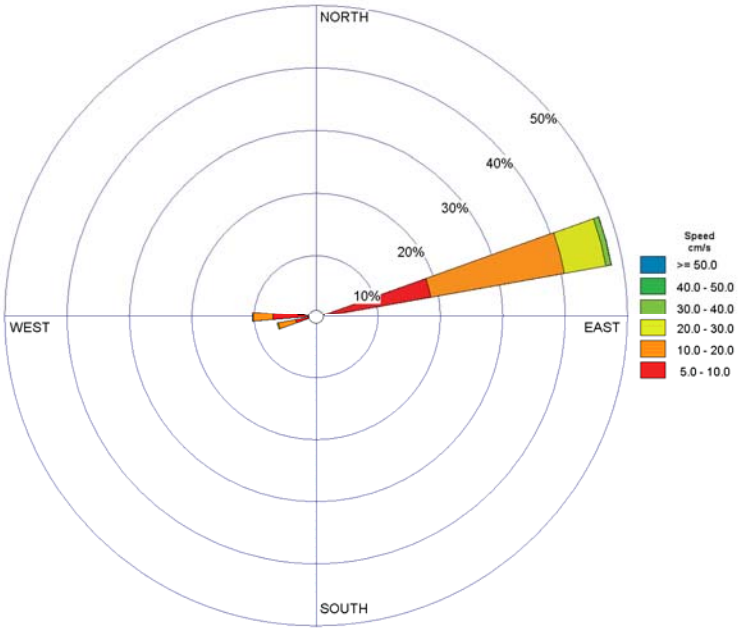

Figure 6.7 Hindcast current rose for the combined tidal and wind-driven residual flows at location C1 (45.917643°, 170.512322°), mid way along Ocean Beach in 10 m water depth.

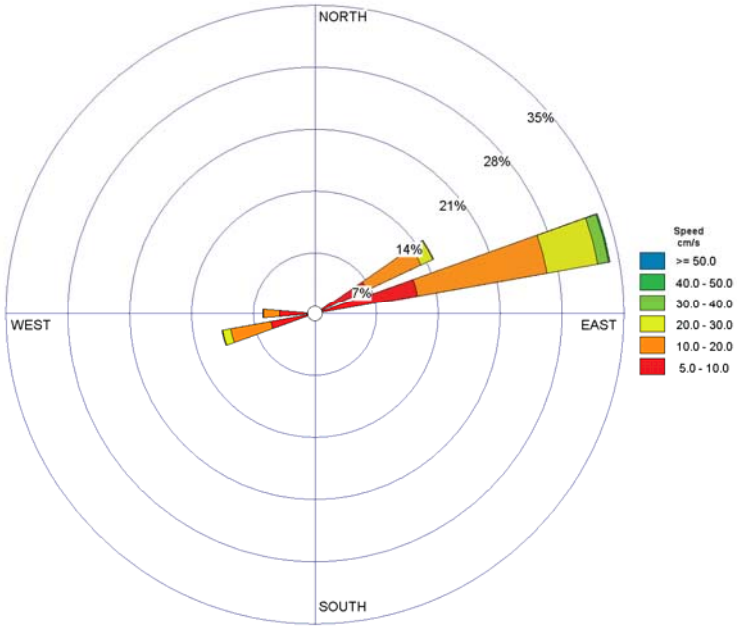

Figure 6.8 Hindcast current rose for the combined tidal and wind-driven residual flows at location C2 (45.917643°, 170.512322°) in 35 m water depth.

Table 6.1 Joint probability distribution (parts-per-thousand) of the depth-averaged current speed and direction from 10 m depth offshore Ocean Beach.

Current speed (m/s)	Current direction (degT)																		
	0-20	20-40	40-60	60-80	80-100	100-120	120-140	140-160	160-180	180-200	200-220	220-240	240-260	260-280	280-300	300-320	320-340	340-360	SUM
> 0 <= 0.05	7.3	11.9	28.9	43	10.8	1.7	0.7	0.4	0.3	0.5	0.8	1.9	11.1	37.1	25.3	11.1	7.1	6.5	206.4
> 0.05 <= 0.1	0	0	0.9	94	8.2	0.1	0	0	0	0	0	0.1	10.3	63.1	1.8	0	0	0	178.5
> 0.1 <= 0.15	0	0	0	94.3	4.2	0	0	0	0	0	0	0	6.7	49.4	0	0	0	0	154.6
> 0.15 <= 0.2	0	0	0	85.2	1.2	0	0	0	0	0	0	0	3.2	37.6	0	0	0	0	127.2
> 0.2 <= 0.25	0	0	0	72.1	0.3	0	0	0	0	0	0	0	1.5	24.8	0	0	0	0	98.7
> 0.25 <= 0.3	0	0	0	58.9	0.1	0	0	0	0	0	0	0	1	14.2	0	0	0	0	74.2
> 0.3 <= 0.35	0	0	0	47.4	0.1	0	0	0	0	0	0	0	0.5	7.8	0	0	0	0	55.8
> 0.35 <= 0.4	0	0	0	34.5	0	0	0	0	0	0	0	0	0.1	4.3	0	0	0	0	38.9
> 0.4 <= 0.45	0	0	0	24.9	0	0	0	0	0	0	0	0	0	1.2	0	0	0	0	26.1
> 0.45 <= 0.5	0	0	0	16.1	0	0	0	0	0	0	0	0	0	0.6	0	0	0	0	16.7
> 0.5 <= 0.55	0	0	0	9.3	0	0	0	0	0	0	0	0	0	0.3	0	0	0	0	9.6
> 0.55 <= 0.6	0	0	0	7	0	0	0	0	0	0	0	0	0	0	0	0	0	0	7
> 0.6 <= 0.65	0	0	0	2.8	0	0	0	0	0	0	0	0	0	0	0	0	0	0	2.8
> 0.65 <= 0.7	0	0	0	2.1	0	0	0	0	0	0	0	0	0	0	0	0	0	0	2.1
> 0.7 <= 0.75	0	0	0	0.8	0	0	0	0	0	0	0	0	0	0	0	0	0	0	0.8
> 0.75 <= 0.8	0	0	0	0.4	0	0	0	0	0	0	0	0	0	0	0	0	0	0	0.4
> 0.8 <= 0.85	0	0	0	0.2	0	0	0	0	0	0	0	0	0	0	0	0	0	0	0.2
> 0.85 <= 0.9	0	0	0	0	0	0	0	0	0	0	0	0	0	0	0	0	0	0	0
> 0.9 <= 0.95	0	0	0	0	0	0	0	0	0	0	0	0	0	0	0	0	0	0	0
> 0.95 <= 1	0	0	0	0	0	0	0	0	0	0	0	0	0	0	0	0	0	0	0
SUM	7.3	11.9	29.8	593	24.9	1.8	0.7	0.4	0.3	0.5	0.8	2	34.4	240.4	27.1	11.1	7.1	6.5	1000

Table 6.2 Joint probability distribution (parts-per-thousand) of the depth-averaged current velocity to the east (U) and significant wave height. Data from the period 1998-2002.

Hs (m)	Depth-averaged current velocity to the east (m/s)																	
	-0.8	-0.7	-0.6	-0.5	-0.4	-0.3	-0.2	-0.1	0	0.1	0.2	0.3	0.4	0.5	0.6	0.7	0.8	SUM
> 0 <= 0.5	0	0	0	0	0	0.3	4.6	13.4	18.9	12.7	4.9	0.1	0	0	0	0	0	54.9
> 0.5 <= 1	0	0	0	0	0.9	11.6	40.1	77.1	82.1	56.3	24	4	0	0	0	0	0	296.1
> 1 <= 1.5	0	0	0	0.3	5.4	19.3	34.4	57.5	70.6	62.9	43.8	15.9	1.5	0.1	0	0	0	311.7
> 1.5 <= 2	0	0	0.1	0.6	3.8	6.8	10.9	18.3	27.2	34.6	39.3	26.9	7.5	0.4	0	0	0	176.4
> 2 <= 2.5	0.1	0	0.3	0.5	1.6	2.7	3.4	4.7	7.8	12.2	13.3	20.3	11.7	2.5	0	0	0	81.1
> 2.5 <= 3	0	0	0.1	0.4	0.5	1.1	1.8	1.7	3.1	3	7.5	10.4	10.5	4.9	0.2	0	0	45.2
> 3 <= 3.5	0	0	0	0	0.4	0.8	0.6	0.8	0.9	1	1	3.4	5.2	4.2	0.4	0	0	18.7
> 3.5 <= 4	0	0	0	0	0.1	0.3	0.5	0.6	0.7	0.6	0.6	0.9	1.7	2.7	1.7	0.1	0	10.5
> 4 <= 4.5	0	0	0	0	0	0.1	0.1	0.1	0.1	0.1	0.3	0.2	0.1	0.8	1.2	0.2	0	3.3
> 4.5 <= 5	0	0	0	0	0.1	0	0.1	0	0	0	0.1	0	0.1	0.5	0.5	0.3	0	1.7
> 5 <= 5.5	0	0	0	0	0	0	0	0	0	0	0	0	0	0	0.2	0.3	0.1	0.6
> 5.5 <= 6	0	0	0	0	0	0	0	0	0	0	0	0	0	0	0.1	0.1	0	0.2
> 6 <= 6.5	0	0	0	0	0	0	0	0	0	0	0	0	0	0	0	0	0	0
> 6.5 <= 7	0	0	0	0	0	0	0	0	0	0	0	0	0	0	0	0	0	0
SUM	0.1	0	0.5	1.8	12.8	43	96.5	174.2	211.4	183.4	134.8	82.1	38.3	16.1	4.3	1	0.1	1000

7 MORPHOLOGY MODELLING RESULTS

7.1 Model output and postprocessing

The hydrodynamic variables, the total depth-averaged sediment flux and rate of change of bed level are stored every six hours through the model simulations. Averaged maps of the depth-averaged current, the sediment flux and rate of bed level change were also calculated for the scenarios by (vector) averaging the six-hourly outputs through the duration of each simulation.

A series of five cross-shore transects were defined as shown in Figure 7.1. The perpendicular (alongshore) and parallel (cross-shore) component of mean sediment flux during each event was extracted along each transect; 'eastwards' and 'westwards' are defined as fluxes towards the eastern and western sides of the transects respectively.

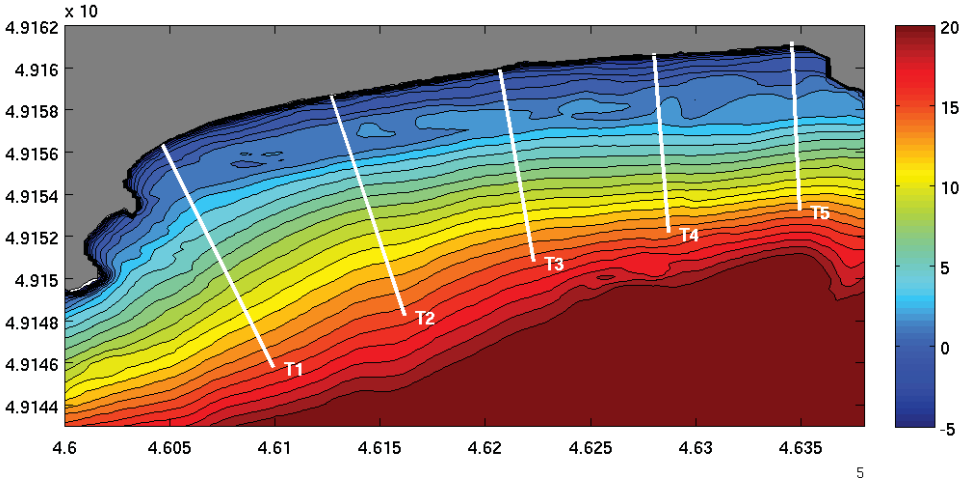

Figure 7.1 Transect locations for modeled alongshore sediment flux.

7.2 Validation of surf zone currents

The surf zone currents generated by the current module were validated in a semi-quantitative manner through comparison with three sets of signal buoys moored at three alongshore locations during February and March 2010. Each buoy set consisted of one buoy tethered to the mooring weight and to a second

buoy which was free to stream in the direction of the current (Figure 7.2). Visual observations were made of the buoy alignment to record the general current direction. The resulting data therefore gives an indication of dominant current direction but without any speed information.

The signal buoys were deployed in three alongshore locations, shown in Figure Figure 7.3; their cross-shore position was approximately in the middle of the trough as it existed on deployment date. Observations of the buoys were made on 14 occasions between 23 Feb 2009 and 18 Mar 2009. The depth-averaged current data from the model was extracted for the same times and locations.

Figure 7.2 One of the signal buoys deployed in the surf zone trough. Note the red buoy is moored and the yellow buoy streams with the current.

Figure 7.3 Locations of signal buoys. Imagery from Google Earth.

The observed and modeled current directions are presented in Table 7.1. During periods with winds over about 10 knots, the buoys show a tendency to align with wind rather than the current and are therefore unreliably as current indicators. However there were 10 observations during very low winds, which allow for a meaningful comparison.

At the western buoy A, the model agreed with the observations in terms of both showing flow in the same direction on 7 out of 10 occasions. The observations indicate westward flow on 8 out of 10 occasions while the model has 7. At buoy B, there is no dominant direction. The model also does not exhibit a dominant flow direction, and agrees with observations in terms of directional quadrant in 7 out of 10 cases. Buoy C also has no dominant observed direction. By contrast the model consistently shows easterly flow. Agreement with the model is poor, for only the 4 out of 10 cases when observed flow was eastwards.

The validation is not intended to provide a specific and exact validation of the modeled surf zone currents. Without detailed bathymetry data, if is unlikely that a good validation of this kind could be achieved in any case. However it does allow a few useful conclusions to be drawn:

- For the observed periods, flow at the western end of the beach is predominantly towards the west.

- The model is largely successful in reproducing the dominant westward flow at the western end.

- The observed flow direction towards the centre part of the beach is more variable.

- The modeled directions also show variability and correspond at specific times for 70% of the observations at buoy B, approximately 1/3 of the distance along the beach.

- The discrepancy between the modeled dominant direction and observed variability at the eastern buoy location suggests that flow alignment there may be bathymetrically controlled in the model.

Table 7.1 Observed direction of signal buoys compared to modeled current direction. Shaded cells indicate likely wind influence on buoys.

Date	Time NZST	Wind* knots	Swell* m	A		B		C	
				Obs	Model	Obs	Model	Obs	Model
23/02/10	1830	10-20 NE	1.0 SW	SW	W	SW	NE	S/SW	SE
24/02/10	1900	10-15 NE	0.5 SW	SW	SE	SW	SE	S/SW	SW
27/02/10	1300	5 NE	1.5 S/SW	SW	W	NE	E	SW	E
27/02/10	2000	0-5 N	2.0 S/SW	W	NW	E	S	NE	SE
28/02/10	1800	0-5N	1.5 S/SW	NE	NE	NE	NW	SW	E
03/03/10	1830	15 W	1.5-2.0 SW	NE	NW	NE	E	NE	E
04/03/10	1600	5-10 SW	2.0 SW	NW	NW	NW	E	NW	E
05/03/10	1030	0	2.0-2.5 SW	SW	NW	NE	E	NE	E
08/03/10	1930	0	1.5-2.0 SE	NW	W	NW	NW	NW	E
10/03/10	1700	5 NE	1.5-2.0 SE	NW	NE	NW	NW	NW	E
12/03/10	1130	30-40 SW	2.0-2.5 SW	E	W	E	NW	E	E
15/03/10	2000	5 W	2.5-3.5 SW	NE	W	NE	E	NE	E
17/03/10	2000	0	2.5-3.5 S	W	SE	W	NW	W	E
18/03/10	1000	0	2.0-3.0 S	W	W	W	NW	SE	SE

*Observed estimates.

7.3 Model results

7.3.1 Storm events

Results are first presented for the four storm events to illustrate typical flow patterns and sediment transport pathways for the two dominant transport modes on the beach (Figs. 7.4 - 7.11).

The first three southerly storms show very similar patterns in wave-driven currents, sediment transport vectors and the primary zones of erosion and accretion. These events represent the dominant direction for waves approaching Ocean Beach. It is convenient to describe the model results in terms of the various sections of the beach, as follows.

In the western half of Ocean Beach, the model consistently shows a region of strong nearshore flows and high sediment transport occurring around the St Clair headland from the west. At approximately the location of Transect 1, these nearshore flows are deflected offshore by an offshore flow from the western end of the beach. Within the inner surf zone flow is directed to the west on the landward side of the trough, typically in 0 – 1 m water depths (CD) and extending along most of the western third of Ocean Beach. Immediately seaward of the bar, there is another zone of westward flow that also extends along much of the western part of the Beach. This flow is a broader feature and merges with offshore flow from the far western end.

Erosion is seen near the high tide level, and there is also some offshore migration of the bar (Figs. 7.8 - 7.10). Specific locations of erosion/accretion are not necessarily significant as they are determined by the specific initial bathymetry. Modeled sediment transport is in opposite directions with strong eastward flux offshore, but a mean westward flux occurring within the surf zone (Transects 1 and 2).

In the central regions of Ocean Beach, there is a bifurcation of the nearshore flows; with a broad westerly flow on one side and slight easterly flows on the other. The sediment transport vectors suggest net onshore transport from regions beyond the bar, veering to the west in the nearshore regions.

In the eastern third, nearshore currents are generally to the east but also show signs of recirculating flows consistent with rip cell dynamics. The sediment transport flux offshore of the surf zone is clearly directed to the east with sediment escaping the beach around Lawyers Head at the eastern end.

The distinctive current flow patterns and resultant sediment transport vectors for these three southerly storm events is primarily caused by the wave energy gradient that exists along the beach under these conditions. The initialising bathymetry will also exert a degree of influence as well, in particular in determining the location and configuration of any circulation associated with rip channels and other alongshore variable features.

It is notable that: i) there is a net eastward sediment flux at either end of Ocean Beach, ii) there is a large circulation cell along the western beach, with a strong westward sediment flux adjacent to the surf zone and eastward flux further offshore in deeper water, and iii) the nearshore zone of strong westward flows corresponds with the zone of lower wave energy.

Under the southerly storm conditions, the model is predicting shoreline erosion along the whole beach with greatest magnitude from just west of St Kilda Beach to the immediate east of St Clair Beach. At the western end sediments are actively eroded from the intertidal beach and deposited in the trough, while being rapidly advected to the west. This process is occurring within the surf zone in relatively shallow water. The modeled area of erosion is in qualitative agreement with the visual observations of morphological change during the three specific storm events.

The model outcomes for the southeasterly storm are quite different (see Fig. 7.10). Under these conditions, the wave height gradient is reversed and there is more energy reaching the St Clair end of the beach. The current flows and sediment transport vectors are uniformly directed to the west, and there are no significant circulation cells. Strong nearshore flows and intertidal beach erosion occurs from St Kilda to St Clair, as for the southerly storms. Under the southeasterly storm conditions, the along-shore flows are driven by the high

angle of incidence between the waves and the shoreline, rather than by gradients in water level setup.

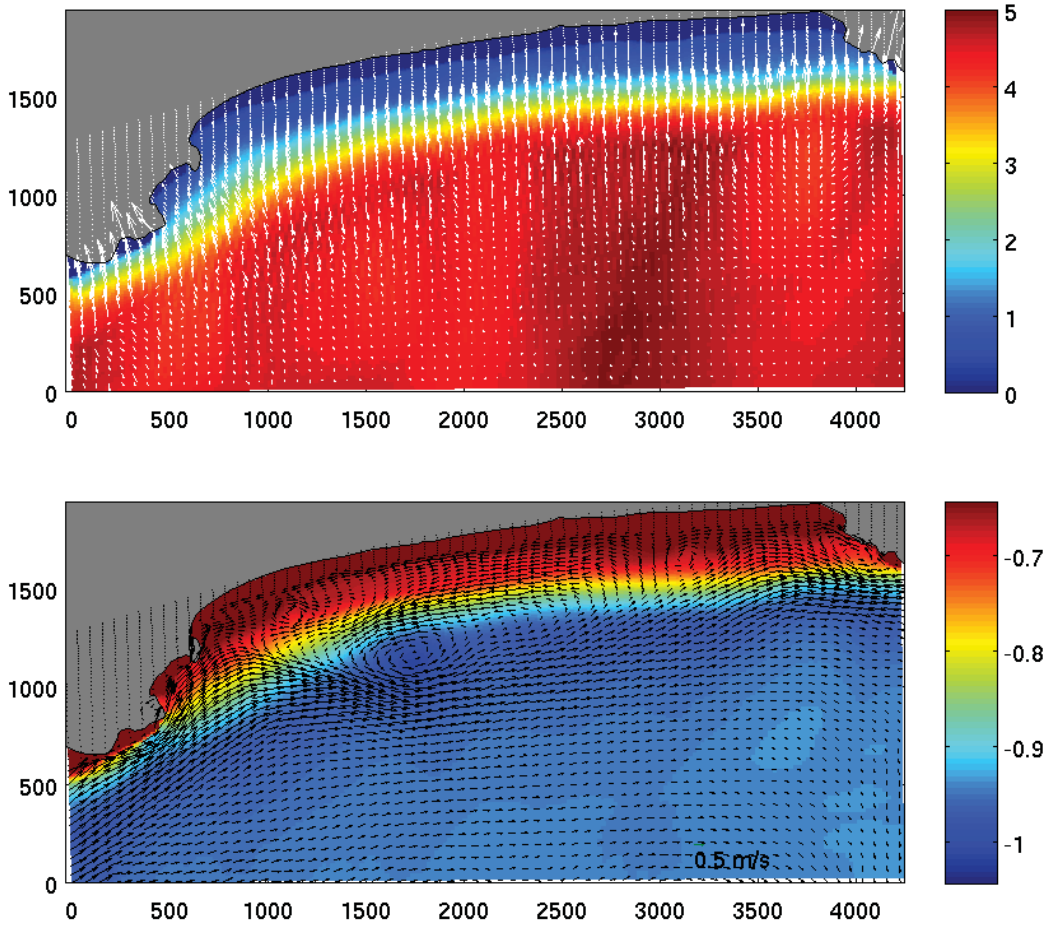

Figure 7.4 Snapshot of significant waveheight [m] (top) and depth-averaged current and wave-averaged elevation [m] (bottom) during the storm of 12-13 April 2007.

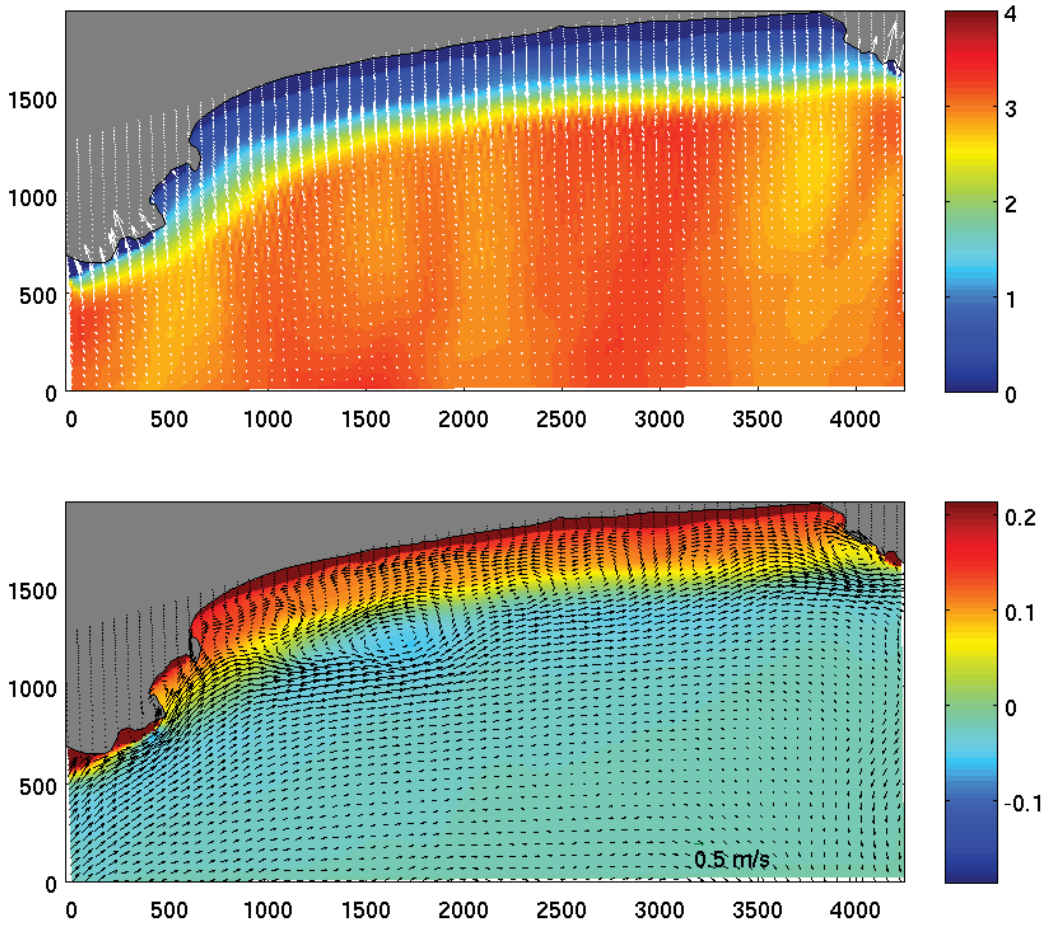

Figure 7.5 Snapshot of significant waveheight [m] (top) and depth-averaged current and wave-averaged elevation [m] (bottom) during the storm of 16-17 May 2007.

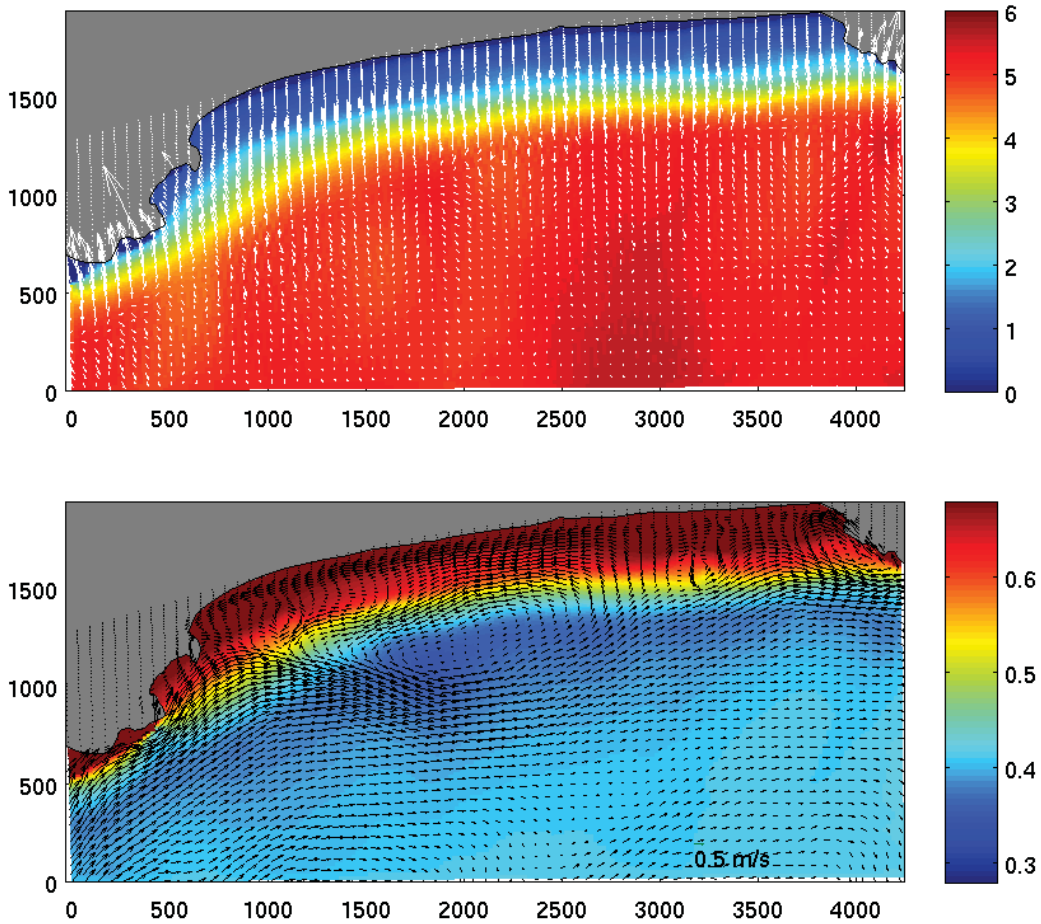

Figure 7.6 Snapshot of significant waveheight [m] (top) and depth-averaged current and wave-averaged elevation [m] (bottom) during the storm of 22-27 June 2007.

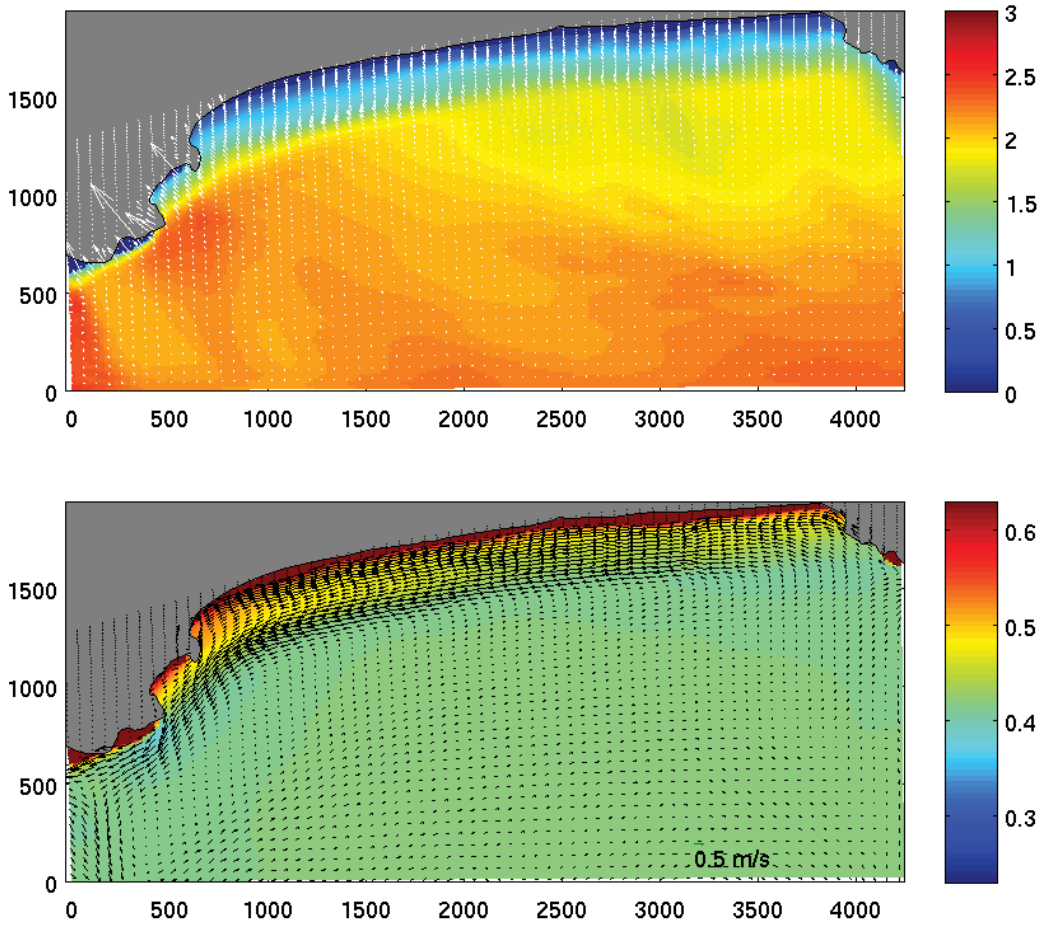

Figure 7.7 Snapshot of significant waveheight [m] (top) and depth-averaged current and wave-averaged elevation [m] (bottom) during the SE event of 1-4 August 2007.

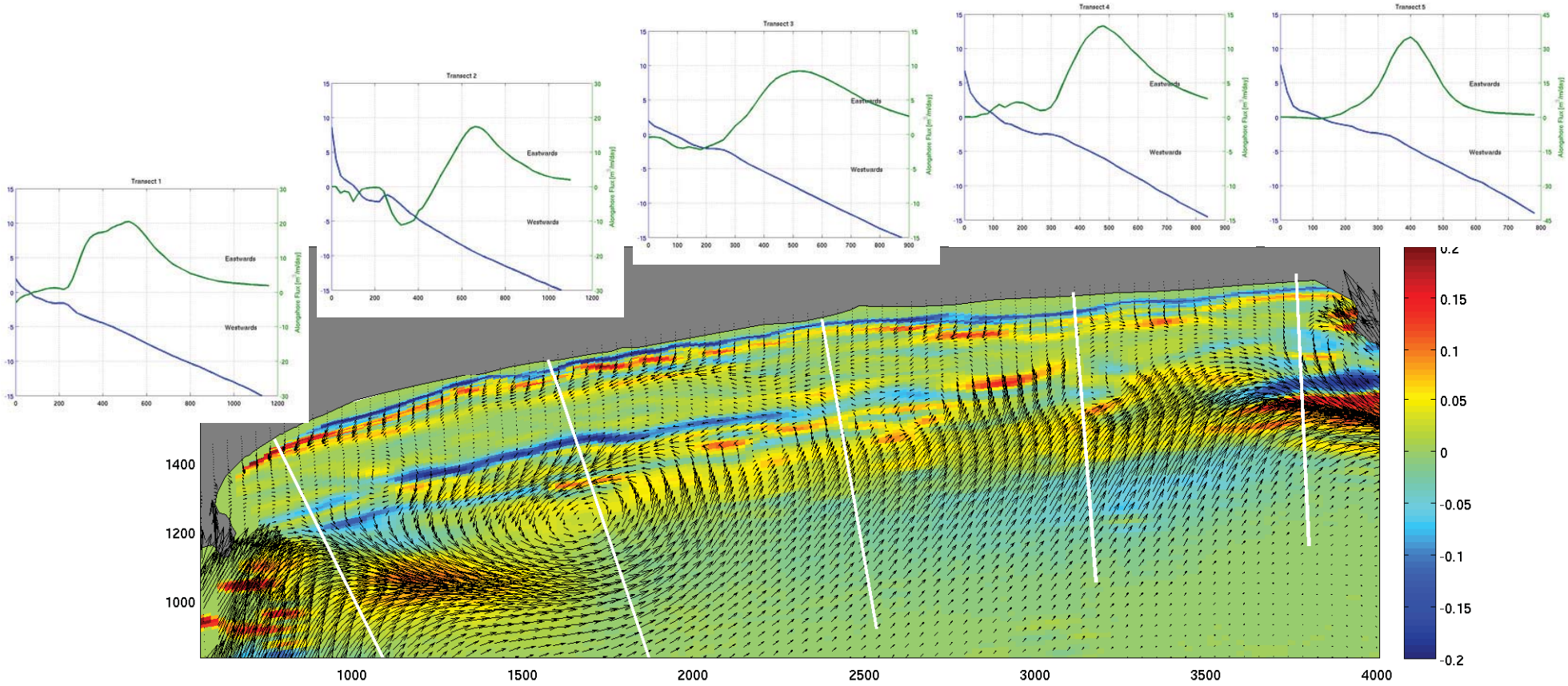

Figure 7.8 Mean sediment flux and change of bed level [m/day] over Storm 1 with alongshore flux shown for each transect.

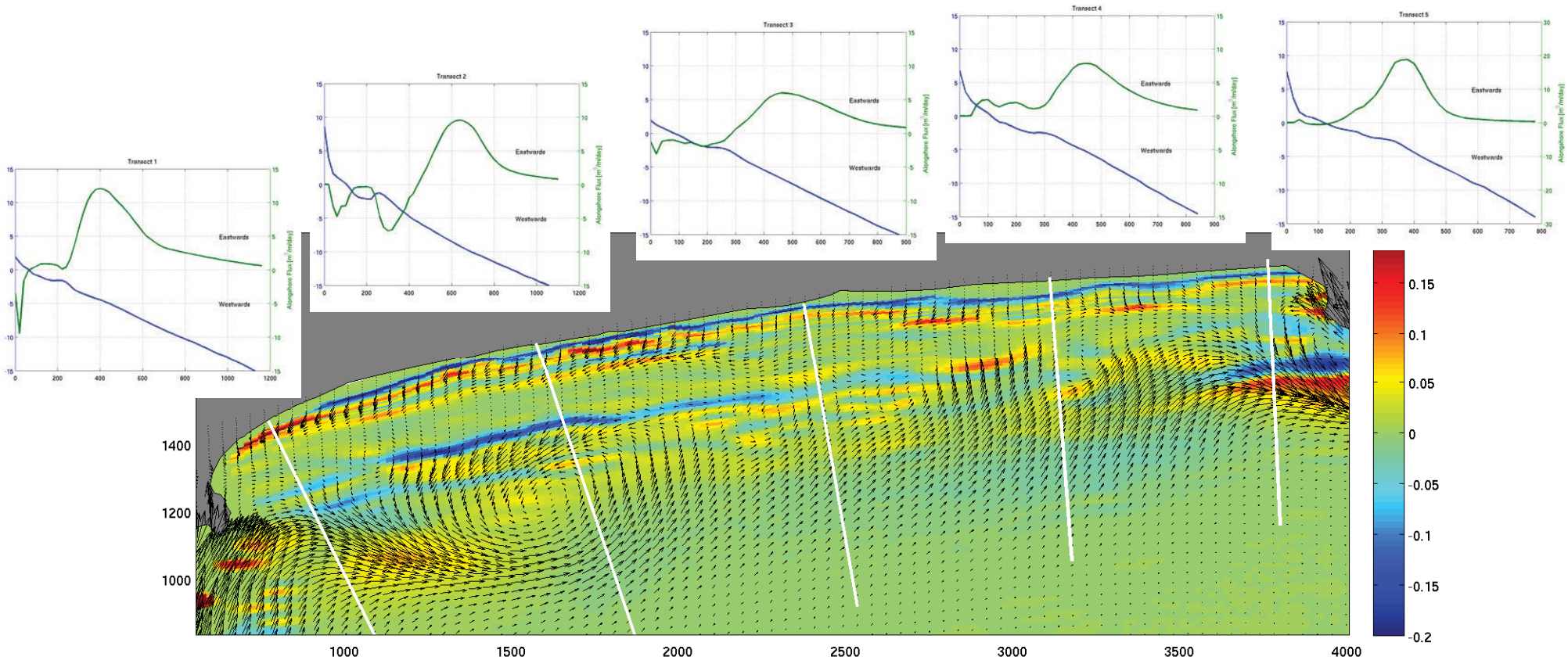

Figure 7.9 Mean sediment flux and change of bed level [m/day] over Storm 2 with alongshore flux shown for each transect.

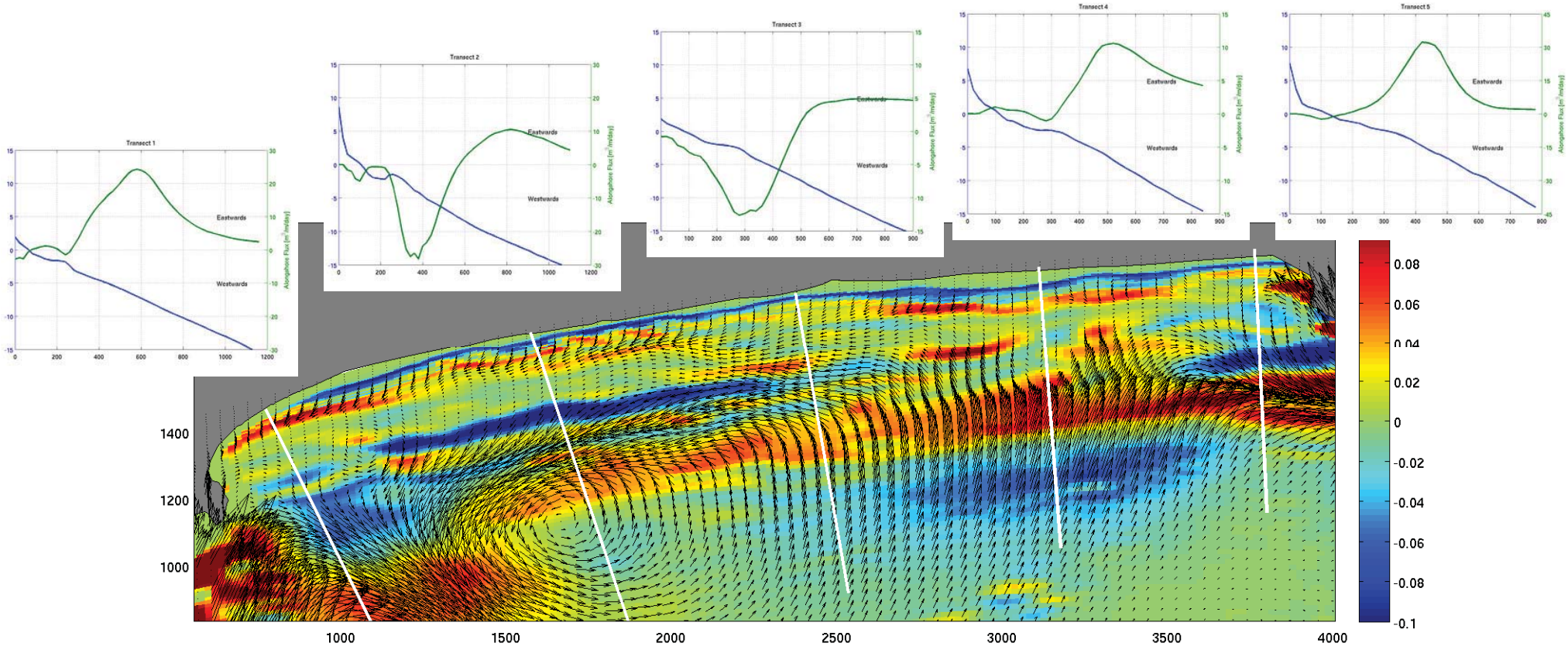

Figure 7.10 Mean sediment flux and change of bed level [m/day] over Storm 3 with alongshore flux shown for each transect.

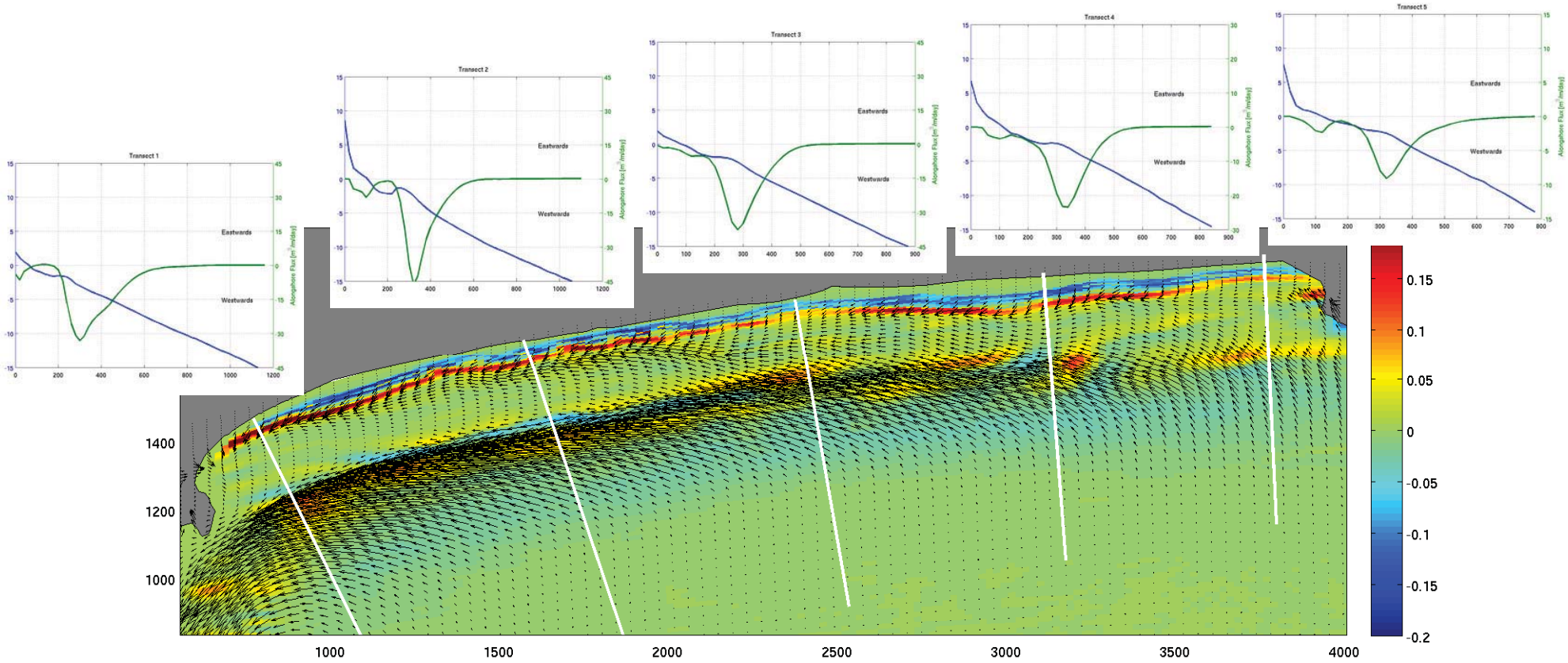

Figure 7.11 Mean sediment flux and change of bed level [m/day] over the SE event with alongshore flux shown for each transect.

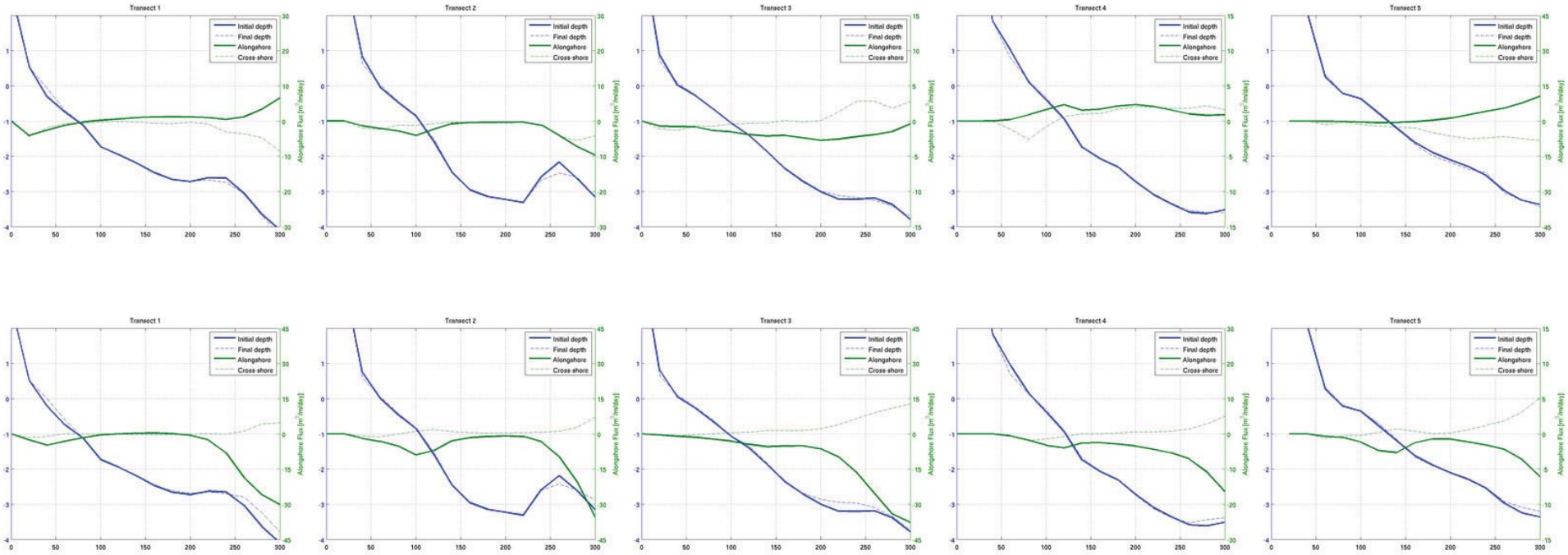

Figure 7.12 Cross-shore profiles of alongshore and cross-shore sediment flux for Storm 1 (top row) and the SE event (bottom row). Flux is +ve eastwards and onshore.

Storm 1

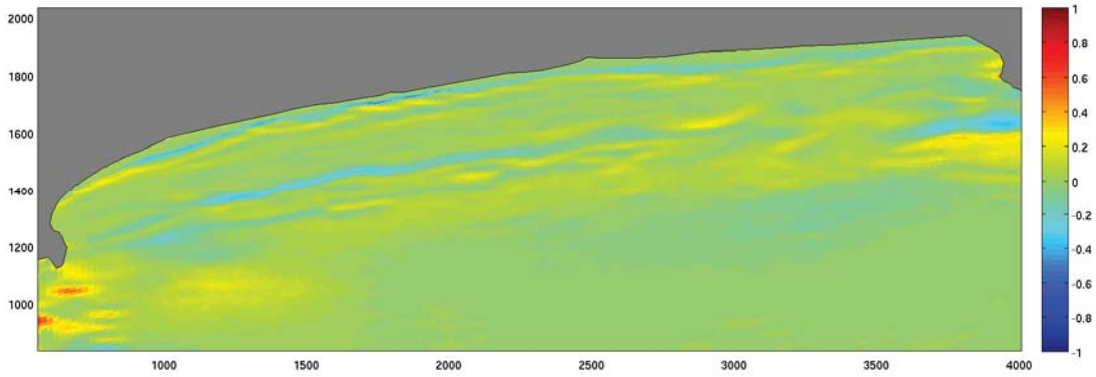

Storm 2

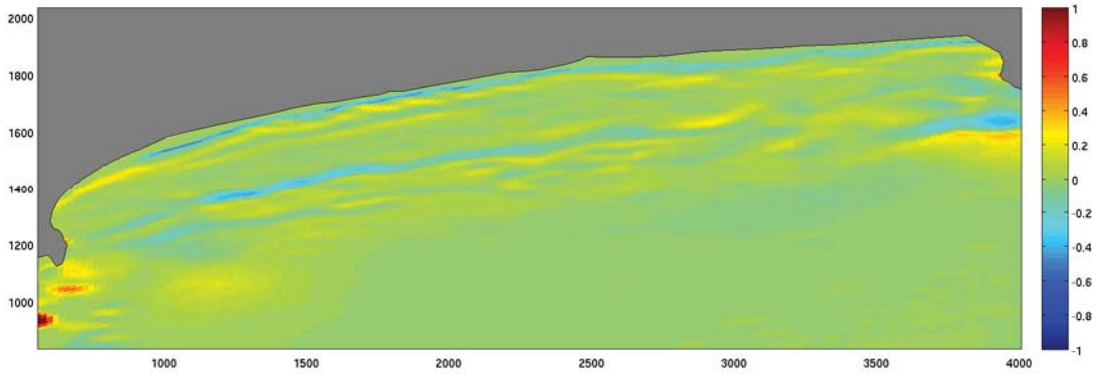

Storm 3

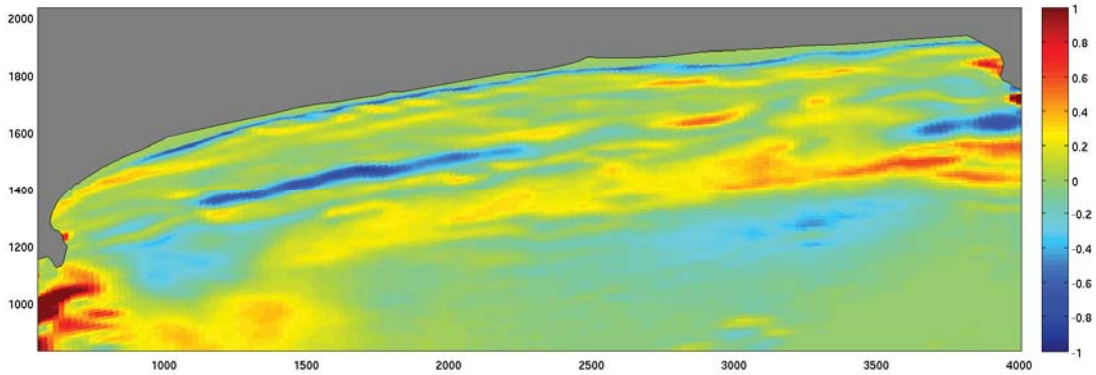

SE event

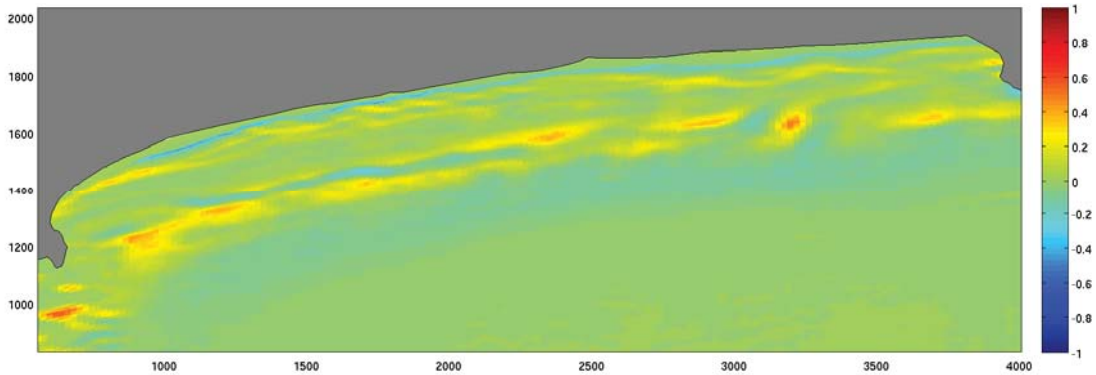

Figure 7.13 Change of bed level for the three storm events and the SE event. Accretion is positive.

7.3.2 Seasonal trends

Averaged sediment flux for the example winter and summer periods in 2006/2007 are shown in Fig. 7.14. These are intended to provide a general picture of the longer term mean sediment fluxes.

Both seasonal periods shows a pattern of mean sediment transport that is broadly similar to the model outcomes from the individual southerly storm events. The strong westerly-directed nearshore flows (and sediment transport vectors) persist along the western third of the beach. However, the integrated fluxes over the entire domain show a net sediment transport to the east.

Modeled mean total flux through the eastern transect averages approximately 500 m^3/day during summer and approximately 750 m^3/day in winter. Based on these figures a tentative estimate of yearly total flux would be of the order of ~200,000 m^3, directed to the east.

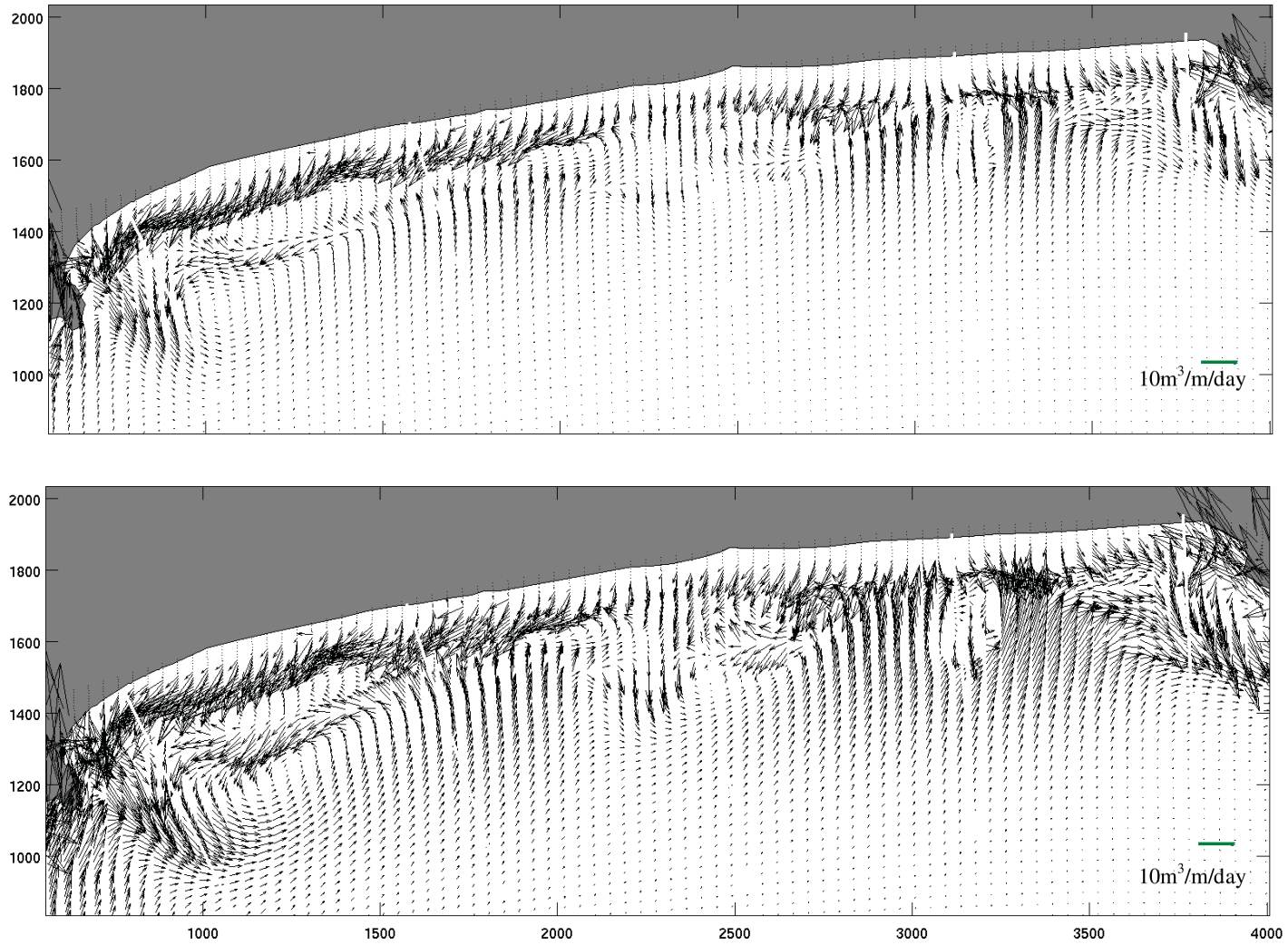

Figure 7.14 Summer 2006/2007 (top) and winter 2007(bottom) mean sediment transport.

7.3.3 2009 periods

The measured and modeled change of bed level for the two periods during 2009 are shown in Figs 7.15 and 7.16. The model shows beach building behaviour during both of these periods (Fig 7.17) with overall accretion within the inner surf zone and onshore bar migration.

Agreement with the measurements of the beach face and intertidal change are reasonable for July-September, which was a period of considerable beach rebuilding. However the observed changes were of erosion for the January to March period, which was not seen in the model. As with the storm cases, it is worth noting that the beach response is very similar for the two periods, which indicates that its adjustment within the model is largely determined by the initial bathymetry. Comparisons of specific changes may therefore be relatively unreliable.

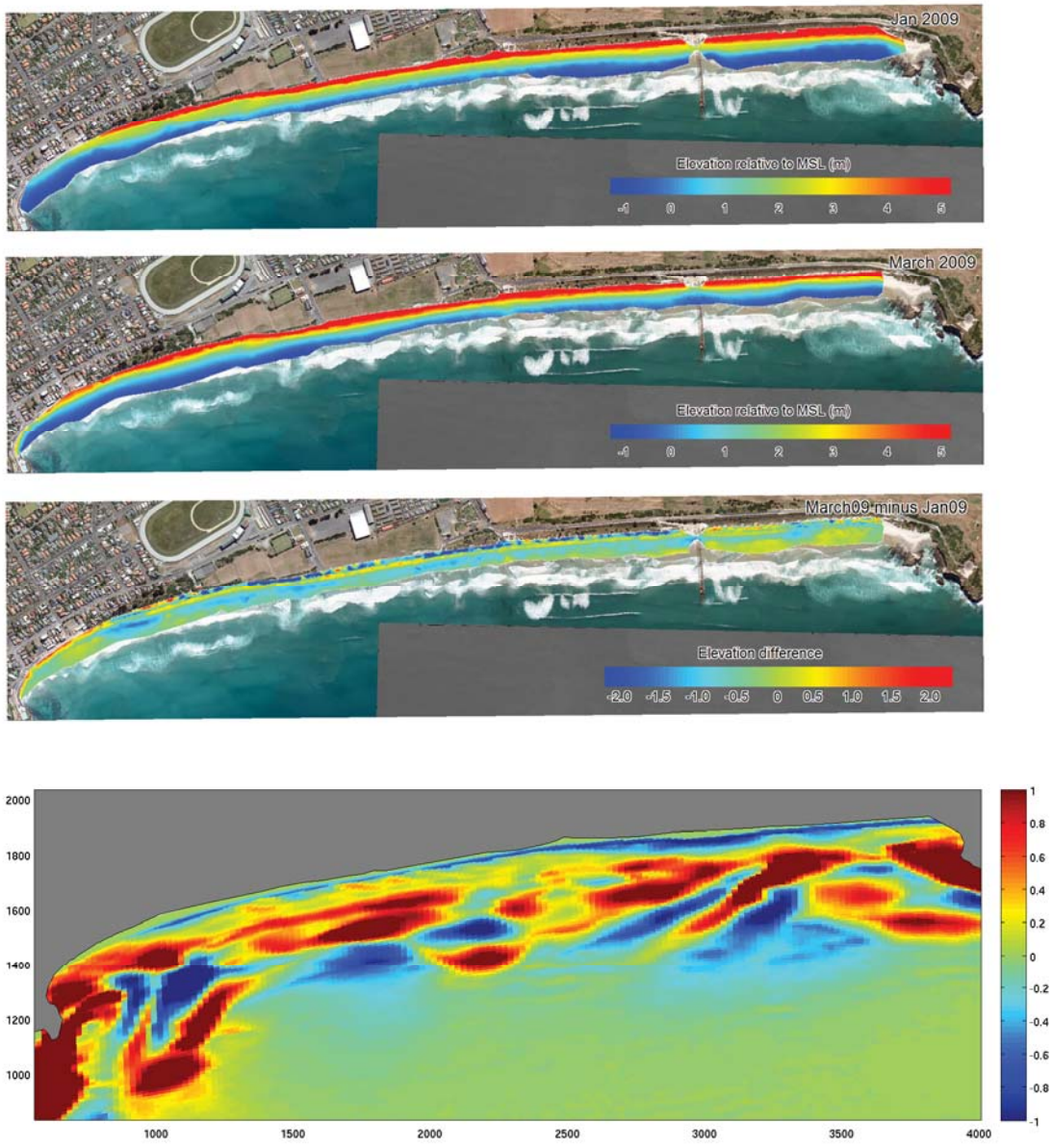

Figure 7.15 Measured (top three figures) modeled (bottom figure) change of bed level between 14 January and 14 March 2009.

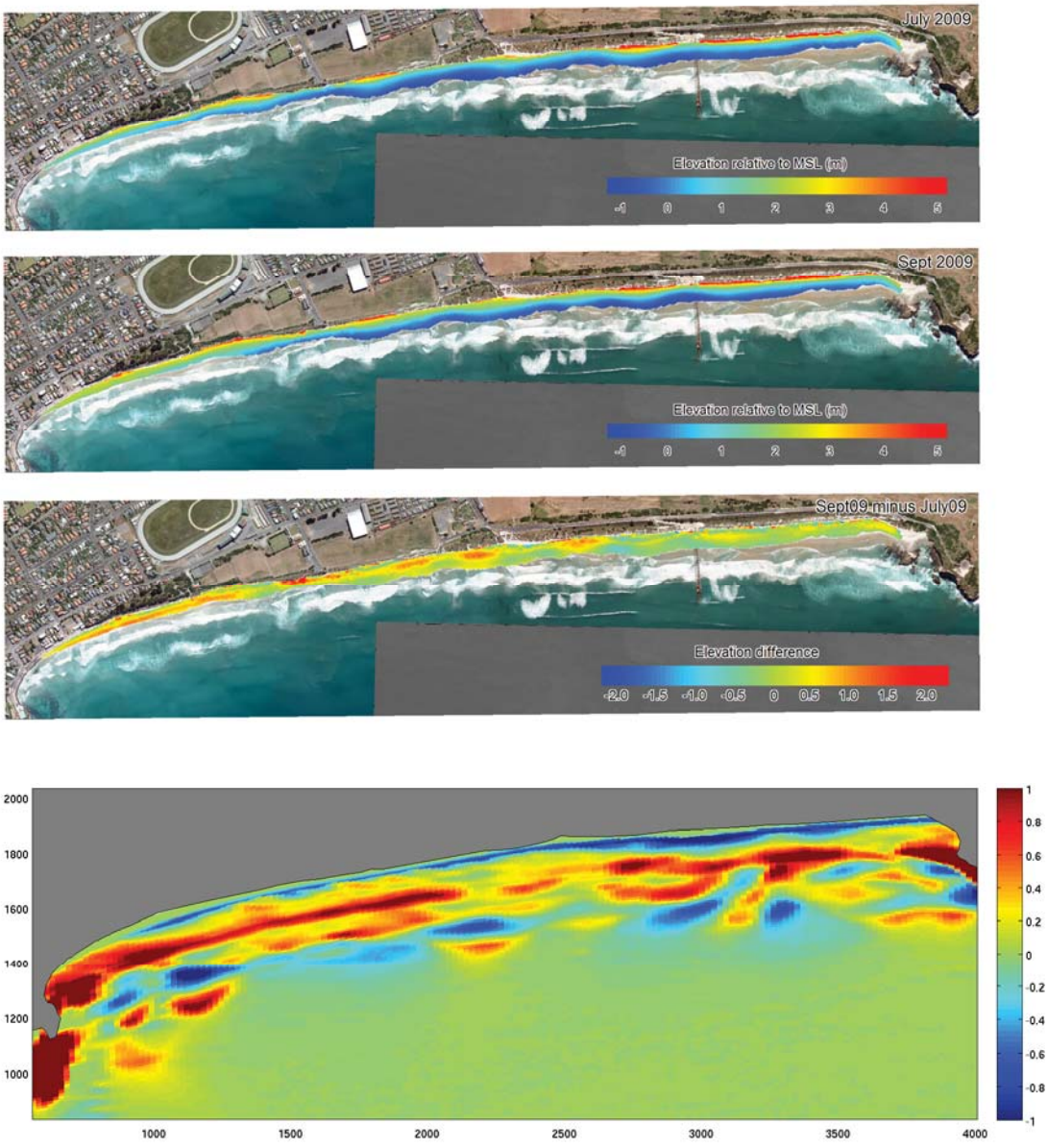

Figure 7.16 Measured (top three figures) modeled (bottom figure) change of bed level between 26 July and 28 September 2009.

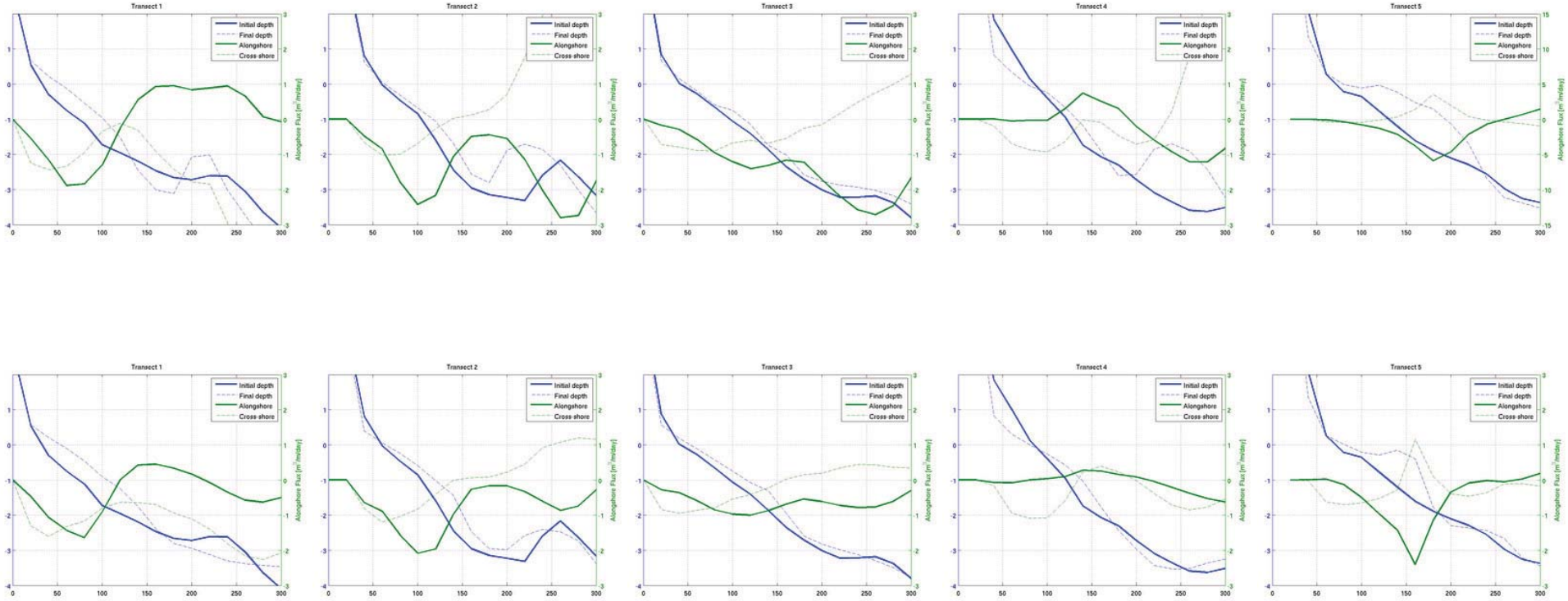

Figure 7.17 Cross-shore profiles of bed level change and along and cross-shore flux for the period 14 Jan – 14 March 2009 (top) and 26 July – 28 September 2009 (bottom). The alongshore transport is +ve eastwards and cross-shore transport is +ve onshore.

7.4 Discussion

The sediment transport model results presented here are solely driven by wave processes at the shore. The wave energy gradient along Ocean Beach is responsible for the westward sediment flux within the surf zone at the western end of the beach. The wave processes also drive a strong sediment flux around the St Clair Headland from the west, and a net transport to the east of the Ocean Beach littoral cell (i.e. past Lawyers Head). It is worth noting that the sediment transport modeling has assumed the Ocean Beach littoral system is not supply limited.

The regional coastal currents (Section 6) will further influence the overall sediment transport regime, particularly during the energetic wave conditions. The hindcasting has shown that the mean current flow is directed to the east, and the highest currents (also to the east) typically coincide with the larger wave events. The open ocean currents are not expected to affect the nearshore and surf zone sediment dynamics, but they will certainly influence the net volumes of sediments moving into and out of the Ocean Beach coastal compartment. Accordingly, the timing, duration and magnitude of preceding wave events and coastal current flows may be influencing the sediment volumes on the beach at any given time.

The results show westerly flows within the surf zone along the western third of the beach. This generic aspect of the modeled flow structure is supported by the signal buoy observations in Section 7.2. In addition, this would appear to be a persistent feature, independent of the exact nearshore bathymetry.

During storm events, erosion of the upper beach face occurs with deposition of the sediments in the trough (and subsequent advection). Thus, the western section of the beach is dominated by a linear, alongshore flux, while the central and eastern parts of the beach features relatively more cross-shore advection. Despite the higher wave energy and greater instantaneous sediment transport, the eastern beach does not experience as much erosion during storms; it is postulated that this part of the beach is in dynamic equilibrium with the wave climate.

The long term seasonal runs show similar mean outcomes in terms of the patterns and flows. Note that the highly nonlinear nature of sediment transport means that averages

are strongly influenced by the few storm events. However when interpreting the long term results, it needs to be considered that the morphology was not updated during the simulations, so the beach was not able to erode and accrete. The details of the flow patterns appear to be strongly governed by the initial bathymetry conditions (i.e. the bar and trough morphology).

The model has shown the ability to simulate beach building, including onshore bar migration. Comparison with measured upper beach and subtidal surveys however has been inconclusive. As with the other runs, the similarity of the two 2009 periods is partially determined by the use of the same (but not actual) measured bathymetry. There remains the question of how much of the model response is determined by initial bathymetry conditions. A rigorous validation of the morphodynamic processes, in particular the cross-shore balance, is probably not achievable without sequential measured subtidal bathymetries.

8 SUMMARY OF THE DYNAMICS

This section provides a summary of the wave, ocean current and sediment transport and morphology dynamics for Ocean Beach. It should be noted that wind effects on the sub-aerial beach and dunes are not considered in this study scope.

8.1 Wave climate

The Ocean Beach wave climate has been hindcast for a 10-year period. The results of the numerical hindcasting technique have been validated with data from a wave buoy moored 1.2 km offshore of the beach during January – May 2007.

The regional wave climate exhibits a well-defined wave energy gradient; the average wave heights gradually increase from south-west regions towards the Otago Peninsula. Regions to the north of the Peninsula are typically sheltered from the dominant wave conditions. Significant wave heights exceeding 8 m were hindcast for the inner shelf regions over the period 1998-2007, and the 100-year return period wave height offshore Dunedin (35 m water depth) is 9.22 m. The regional wave climate may be described as swell-dominated, with the largest wave events approaching from the south.

Local scale wave modeling at Ocean Beach has shown that the nearshore wave climate is strongly influenced by White Island and its' extensive bathymetric features. The combined effects of direct shadowing, combined with wave refraction and seabed friction from the subtidal structures cause a wave energy shadow that extends over the western half of Ocean Beach. The overall shadowing effect varies with the incident wave direction and period, so the wave energy gradients along the beach face are not constant. The dominant condition, however, is for a zone of higher wave energy between Lawyers Head and St Kilda, and a transition zone to lower wave energy located between St Kilda and Middles Beach. The wave climate at St Clair is consistently less energetic than St Kilda and the eastern third of Ocean Beach.

Analysis of the 10 year wave hindcast dataset shows the expected seasonal modulation in the mean monthly wave height (i.e. lowest in January, highest in June and August), but also reveals that very energetic conditions can occur throughout the year. The

largest storm event in the hindcast was during February 2004. A strong inter-annual signal is evident in the wave height timeseries, and the Years 2002, 2004 and 2007 stand out as being significantly more energetic than the 10-year average.

8.2 Open ocean currents

The ocean current regime for Otago region and the Ocean Beach area has been hindcast for a 5-year period. The results of the numerical hindcasting technique have been validated with data from current meters that were deployed off Ocean Beach during July – September 2001.

The mean regional ocean currents are predominantly directed to the north and northeast, with significant acceleration of the current flows in the vicinity of Cape Saunders and along sections of the southern Otago Peninsula. Moderate nearshore flows, directed to the east, extend from near Green Island to Smails Beach, with further strengthening eastward flows toward Allans Beach. From Brighton through to Tairei Mouth the mean nearshore flow regime is of comparatively lower energy.

Within the Ocean Beach region, the mean currents are directed to the east, with flow acceleration over the bathymetric sill between White Island and the St Clair Headland. Strong nearshore currents are evident along the coastline from Blackhead to St Clair, with reduced flows along the Ocean Beach region, and then a further strengthening of the flows in the region to the east of Lawyers Head. The White Island bathymetric structures create a slight current shadow in their lee.

The nearshore currents are predominantly alongshore, with a strong bias to the eastward direction. Some 75% of all the current flows exceeding 0.1 ms^{-1} are directed to the east, including the highest flow conditions. The maximum hindcast current speed was 0.87 ms^{-1}, and the 95^{th} percentile exceedence level was 0.43 ms^{-1}. Tidal currents provide only a small contribution to the overall current variance at Ocean Beach. The occasions of high current flow are all associated with coincident energetic wave conditions, and the flows are predominantly directed eastward.

8.3 Sediment transport and morphology response at Ocean Beach

The sediment transport and morphology response of the beach to southerly and southeasterly storms has been modeled. The dominant direction for storm wave conditions approaching Ocean Beach is from the south, however energetic southeasterly events occur and appear to generate different overall sediment transport pathways and have significant morphological impacts.

In southerly storm conditions, the model predicts a consistent pattern of wave-driven circulation, sediment transport, and areas of beach erosion:

- The offshore bathymetry associated with White Island produce a gradient in wave height along the beach with larger waves at the eastern end.
- The longshore setup gradient drives a persistent westerly flow within the surf zone along the western third of the beach. Seaward of the bar, there is another broader zone of westward flow that also extends along much of the western part of the Beach.
- In the central regions of Ocean Beach, there is bifurcation of the nearshore flows; with a broad westerly flow on one side and slight easterly flows on the other.
- At the eastern end of the beach flow is mainly eastward but also features recirculating regions associated with rip channels.
- Active erosion of the upper beach face and deposition of the sediments in the trough occurs primarily at the western end of the beach and this material is subsequently advected to the west.
- Sediment transport vectors suggest net onshore transport through the central part of the beach, veering to the west in the nearshore regions.
- In the eastern third of the beach, the transport vectors are clearly directed to the east. Despite the higher wave energy, the central and eastern parts of the beach do not exhibit as much erosion in the storms, suggesting that this region may be in dynamic equilibrium with the wave climate.

A conceptual diagram of the sediment transport regime in southerly storms is shown on Figure 8.1.

The model outcomes for the southeasterly storm conditions are quite different. Here, the wave height gradient is reversed and there is more energy reaching the St Clair end of the beach. The current flows and sediment transport vectors are uniformly directed to the west, and there are no significant circulation cells (despite the same initial bathymetry); the along-shore flows are driven by the high angle of incidence between the waves and the shoreline, rather than by gradients in water level setup. Strong nearshore flows and intertidal beach erosion occurs from St Kilda to St Clair, as for the southerly storms.

Regional coastal currents will influence the overall sediment transport regime, particularly during the storm conditions. These currents typically provide an easterly alongshore vector to the sediments mobilised by wave action. They are unlikely to significantly influence the nearshore and surf zone sediment dynamics, but they will alter the net volumes of sediments moving into and out of the Ocean Beach coastal compartment. Based on the modeled seasonal average sediment flux, a tentative estimate of total yearly flux passing to the east around Lawyers Head is 200,000 m^3/year.

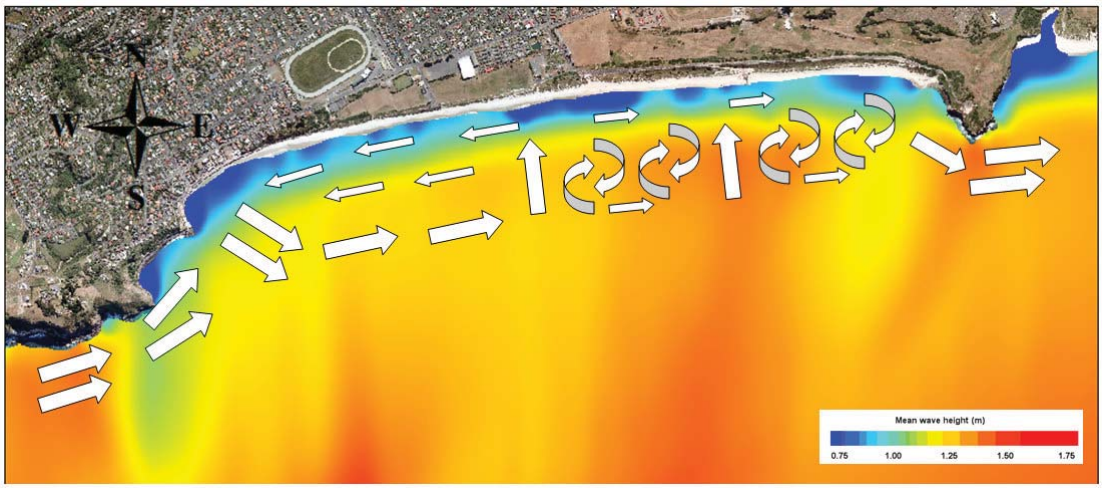

Figure 8.1 Conceptual diagram showing the mean sediment transport pathways during southerly storm conditions, along with the annual mean significant wave height

9 RECOMMENDATIONS

The numerical modeling of waves, currents and sediment transport has clearly identified several key processes that dominate the sediment dynamics along Ocean Beach. The typical storm conditions have been modeled, and the resultant erosion of the upper beach has been simulated. Beach building conditions with onshore bar migration have also been simulated. The work to date has established a set of robust numerical tools that can be used to examine and test a range of potential management options for the beach, and also to consider the dynamics of the beach under future scenarios. For example:

- The morphology model can be used to consider the likely changes to the beach dynamics under a range of sea level rise scenarios.
- Management options such as renourishment can be optimised to ensure that introduced material is deposited in the ideal location to maximise the benefits.
- Making use of the sediment recirculation patterns along the beach can be examined - including the feasibility of transferring sediments from the eastern beach to a renourishment location.
- Engineering options (e.g. groynes or detached structures) that directly target the processes leading to beach erosion can be evaluated with the morphology model; identifying their effectiveness and quantifying the likely positive and negative outcomes.

10 REFERENCES

Caires, S and Sterl, A. (2004). 100-Year Return Value Estimates for Ocean Wind Speed and Significant Wave Height from the ERA-40 Data. Journal of Climate, 18: 1032-1048.

Egbert, G.D., and S.Y. Erofeeva, (2002) Efficient inverse modeling of barotropic ocean tides, J. Atmos. Oceanic Technol., 19(2), 183-204.

Goda, Y. (1970). Numerical experiments on wave statistics and spectral estimates. Report of the Port and Harbour Research Institute, 9(3): 3-57.

Grasmeijer, B.T. and Ruessink, B.G. (2003) Modeling of waves and currents in the nearshore: parametric vs. probabilistic approach. Coastal Engineering. 49, 185-207.

Holthuijsen, L.H., (2007). Waves in Oceanic and Coastal Waters. Cambridge University Press. ISBN 0521860288, 9780521860284

HSE, (2001). Environmental Considerations. A report by Bomel Ltd to the U.K. Health and Safety Executive. Offshore Technology Report 2001/010. HSE Books, 73 p.

Long, W., Kirby, J.T. and Shao, Z. (2008) A numerical scheme for morphological bed level calculations. Coastal Engineering 55(2), 167-180.

Marchesiello, P., J. C. McWilliams, A. F. Shchepetkin, 2001: Open boundary conditions for long-term integration of regional ocean models, Ocean Modeling, 3, 1-20.

Mellor, G.L. (2004) Users guide for a Three-dimensional, primitive equation, numerical ocean model.

Nicholson, J., Broker, I. Roelvink, J.A., Price, D., Tanguy, J.M. and Moreno, L. (1997) Intercomparison of coastal area morphodynamics models. Coastal Engineering 31, 97-123.

Shi, F., Svendsen, I. A., Kirby, J. T. and Smith, J. M., (2003) A curvilinear version of a quasi-3D nearshore circulation model, Coastal Engineering, 49, 99-124

Shi, F., Kirby, J. T. and Hanes, D. M., (2007) An efficient mode-splitting method for a curvilinear nearshore circulation model, Coastal Engineering, in press.

Svendsen, I. A. and U. Putrevu (1994): Nearshore mixing and dispersion. Proc. Roy. Soc. Lond, A, 445, 561-576. 14.

Zhang, H.M., J.J. Bates, and R.W. Reynolds, (2006). Assessment of composite global sampling: Sea surface wind speed. Geophysical Research Letters, VOL. 33, L17714, doi:10.1029/2006GL027086.

APPENDIX ONE – WAVE DATA TABLES

Table A1.0.1 Annual joint probability distribution (parts per thousand) of the significant wave height and mean wave direction (35 m depth)

Hs (m)	Mean wave direction (degT)								
	337.5 - 22.5	22.5 - 67.5	67.5 - 112.5	112.5 - 157.5	157.5 - 202.5	202.5 - 247.5	247.5 - 292.5	292.5 - 337.5	Total
> 0 <= 0.5	0.1	0.8	14.4	2.8	22.5	7.7	4.1	1.6	54
> 0.5 <= 1	0	0.3	39.9	12.3	203	28.5	7.4	0.3	291.7
> 1 <= 1.5	0	0	40.9	22.4	227.5	15.8	0.8	0	307.4
> 1.5 <= 2	0	0	14.6	16.4	131.8	10.1	0	0	172.9
> 2 <= 2.5	0	0	5.7	9.9	67.5	6.1	0	0	89.2
> 2.5 <= 3	0	0	1.3	5.9	34.7	3.4	0	0	45.3
> 3 <= 3.5	0	0	0.5	4.1	15.6	1.4	0	0	21.6
> 3.5 <= 4	0	0	0.1	2.3	7.6	0.4	0	0	10.4
> 4 <= 4.5	0	0	0.2	0.4	3.1	0	0	0	3.7
> 4.5 <= 5	0	0	0.1	0.3	1.6	0	0	0	2
> 5 <= 5.5	0	0	0.1	0.1	1.1	0	0	0	1.3
> 5.5 <= 6	0	0	0	0	0.2	0	0	0	0.2
> 6 <= 6.5	0	0	0	0	0.1	0	0	0	0.1
> 6.5 <= 7	0	0	0	0	0	0	0	0	0
> 7 <= 7.5	0	0	0	0	0.1	0	0	0	0.1
Total	0.1	1.1	117.8	76.9	716.4	73.4	12.3	1.9	1000

Table A1.0.2 Summer (Dec-Feb) joint probability distribution (parts per thousand) of the significant wave height and mean wave direction (35 m depth)

Hs (m)	Mean wave direction (degT)								
	337.5 - 22.5	22.5 - 67.5	67.5 - 112.5	112.5 - 157.5	157.5 - 202.5	202.5 - 247.5	247.5 - 292.5	292.5 - 337.5	Total
> 0 <= 0.5	0.4	2.1	19	2.5	22.8	9.8	7.3	3.8	67.7
> 0.5 <= 1	0	0.8	31.9	11.8	218.7	28.7	11	0.5	303.4
> 1 <= 1.5	0	0	30.5	22.1	232.4	15.5	1	0	301.5
> 1.5 <= 2	0	0	11	17.7	141.9	11.3	0	0	181.9
> 2 <= 2.5	0	0	2.1	7.8	69	6.9	0	0	85.8
> 2.5 <= 3	0	0	0.1	3.6	29.5	2.3	0	0	35.5
> 3 <= 3.5	0	0	0	0.8	13.5	1.6	0	0	15.9
> 3.5 <= 4	0	0	0	1.1	5.4	0	0	0	6.5
> 4 <= 4.5	0	0	0	0	1.2	0	0	0	1.2
> 4.5 <= 5	0	0	0	0	0.4	0	0	0	0.4
> 5 <= 5.5	0	0	0	0	0.3	0	0	0	0.3
> 5.5 <= 6	0	0	0	0	0	0	0	0	0
> 6 <= 6.5	0	0	0	0	0	0	0	0	0
> 6.5 <= 7	0	0	0	0	0	0	0	0	0
> 7 <= 7.5	0	0	0	0	0	0	0	0	0
Total	0.4	2.9	94.6	67.4	735.1	76.1	19.3	4.3	1000

Table A1.0.3 Autumn (Mar-May) joint probability distribution (parts per thousand) of the significant wave height and mean wave direction (35 m depth)

Hs (m)	Mean wave direction (degT)								
	337.5 - 22.5	22.5 - 67.5	67.5 - 112.5	112.5 - 157.5	157.5 - 202.5	202.5 - 247.5	247.5 - 292.5	292.5 - 337.5	Total
> 0 <= 0.5	0	0	6.5	1.6	16.4	6	2.6	0.3	33.4
> 0.5 <= 1	0	0	33.7	7.9	200	18.6	5.2	0.1	265.5
> 1 <= 1.5	0	0	35.3	14.9	272.1	8.6	0.7	0	331.6
> 1.5 <= 2	0	0	14.8	11.4	154.3	8.2	0.1	0	188.8
> 2 <= 2.5	0	0	4.8	6.8	67.8	6.5	0	0	85.9
> 2.5 <= 3	0	0	0.4	2.4	42.5	3.1	0	0	48.4
> 3 <= 3.5	0	0	0.1	2.2	19.4	1.5	0	0	23.2
> 3.5 <= 4	0	0	0	1	10.7	1.1	0	0	12.8
> 4 <= 4.5	0	0	0	0	4.9	0.1	0	0	5
> 4.5 <= 5	0	0	0	0.3	3.4	0	0	0	3.7
> 5 <= 5.5	0	0	0	0.3	1.1	0	0	0	1.4
> 5.5 <= 6	0	0	0	0.1	0	0	0	0	0.1
> 6 <= 6.5	0	0	0	0	0	0	0	0	0
> 6.5 <= 7	0	0	0	0	0	0	0	0	0
> 7 <= 7.5	0	0	0	0	0	0	0	0	0
Total	0	0	95.6	48.9	792.6	53.7	8.6	0.4	1000

Table A1.0.4 Winter (Jun-Aug) joint probability distribution (parts per thousand) of the significant wave height and mean wave direction (35 m depth)

Hs (m)	Mean wave direction (degT)								
	337.5 - 22.5	22.5 - 67.5	67.5 - 112.5	112.5 - 157.5	157.5 - 202.5	202.5 - 247.5	247.5 - 292.5	292.5 - 337.5	Total
> 0 <= 0.5	0	1.1	12.2	3.3	22.6	3.8	1.5	1.8	46.3
> 0.5 <= 1	0	0	33.4	7.7	155	11.4	4.1	0.3	211.9
> 1 <= 1.5	0	0	40.1	19.3	194.2	14	0.1	0	267.7
> 1.5 <= 2	0	0	28.1	20.9	145.8	5.3	0	0	200.1
> 2 <= 2.5	0	0	13.7	17.8	97.8	3.3	0	0	132.6
> 2.5 <= 3	0	0	2.6	14	49.5	4.9	0	0	71
> 3 <= 3.5	0	0	1.8	10.9	22.6	0.8	0	0	36.1
> 3.5 <= 4	0	0	0.4	7.2	10.7	0.5	0	0	18.8
> 4 <= 4.5	0	0	0.7	1.8	5	0	0	0	7.5
> 4.5 <= 5	0	0	0.5	1.1	2	0	0	0	3.6
> 5 <= 5.5	0	0	0.3	0	3	0	0	0	3.3
> 5.5 <= 6	0	0	0	0	1	0	0	0	1
> 6 <= 6.5	0	0	0	0	0.3	0	0	0	0.3
> 6.5 <= 7	0	0	0	0	0	0	0	0	0
> 7 <= 7.5	0	0	0	0	0	0	0	0	0
Total	0	1.1	133.8	104	709.5	44	5.7	2.1	1000

Table A1.0.5 Spring (Sep-Nov) joint probability distribution (parts per thousand) of the significant wave height and mean wave direction (35 m depth)

Hs (m)	Mean wave direction (degT)								
	337.5 - 22.5	22.5 - 67.5	67.5 - 112.5	112.5 - 157.5	157.5 - 202.5	202.5 - 247.5	247.5 - 292.5	292.5 - 337.5	Total
> 0 <= 0.5	0.4	2.1	19	2.5	22.8	9.8	7.3	3.8	67.7
> 0.5 <= 1	0	0.8	31.9	11.8	218.7	28.7	11	0.5	303.4
> 1 <= 1.5	0	0	30.5	22.1	232.4	15.5	1	0	301.5
> 1.5 <= 2	0	0	11	17.7	141.9	11.3	0	0	181.9
> 2 <= 2.5	0	0	2.1	7.8	69	6.9	0	0	85.8
> 2.5 <= 3	0	0	0.1	3.6	29.5	2.3	0	0	35.5
> 3 <= 3.5	0	0	0	0.8	13.5	1.6	0	0	15.9
> 3.5 <= 4	0	0	0	1.1	5.4	0	0	0	6.5
> 4 <= 4.5	0	0	0	0	1.2	0	0	0	1.2
> 4.5 <= 5	0	0	0	0	0.4	0	0	0	0.4
> 5 <= 5.5	0	0	0	0	0.3	0	0	0	0.3
> 5.5 <= 6	0	0	0	0	0	0	0	0	0
> 6 <= 6.5	0	0	0	0	0	0	0	0	0
> 6.5 <= 7	0	0	0	0	0	0	0	0	0
> 7 <= 7.5	0	0	0	0	0	0	0	0	0
Total	0.4	2.9	94.6	67.4	735.1	76.1	19.3	4.3	1000

Table A1.0.6 Annual joint probability distribution (parts per thousand) of the significant wave height and peak spectral wave period (35 m depth)

Hs (m)	Peak spectral wave period Tp (s)																				
	0-1	**1-2**	**2-3**	**3-4**	**4-5**	**5-6**	**6-7**	**7-8**	**8-9**	**9-10**	**10-11**	**11-12**	**12-13**	**13-14**	**14-15**	**15-16**	**16-17**	**17-18**	**18-19**	**19-20**	**Total**
> 0 <= 0.5	0	0.9	7.3	0.6	1.8	4.9	6.2	4.3	3.1	4.9	6.6	7.1	2.7	1.7	0.9	0.8	0.2	0.1	0	0	54.1
> 0.5 <= 1	0	0	3.5	9.8	4.4	5.6	12.2	15.1	17.7	28.1	47.5	56.1	39.4	33.1	10.4	5.8	2.2	0.8	0.1	0	291.8
> 1 <= 1.5	0	0	0	0.7	7.4	8.2	6.8	11.9	21.5	32.5	56.3	58.9	45.3	35.7	13.7	6.8	1.1	0.3	0	0	307.1
> 1.5 <= 2	0	0	0	0	0.2	7.7	7.3	6.8	10.5	19.2	32.4	34.1	25.7	20.3	6.3	2.1	0.5	0	0	0	173.1
> 2 <= 2.5	0	0	0	0	0	0.3	7.4	5.2	3.3	7.1	17.5	19.7	13.3	11.4	2.3	1.5	0.1	0	0	0	89.1
> 2.5 <= 3	0	0	0	0	0	0	0.8	5.7	1.8	2.6	6.6	11.3	7.9	6.4	1.3	0.7	0	0	0	0	45.1
> 3 <= 3.5	0	0	0	0	0	0	0	1.8	2.6	0.9	1.9	4.7	4	4.1	1.3	0.2	0	0	0	0	21.5
> 3.5 <= 4	0	0	0	0	0	0	0	0.2	1.8	0.7	0.5	1.8	1.9	2.6	0.7	0.1	0	0	0	0	10.3
> 4 <= 4.5	0	0	0	0	0	0	0	0	0.3	0.5	0.3	0.7	0.8	1	0.2	0	0	0	0	0	3.8
> 4.5 <= 5	0	0	0	0	0	0	0	0	0	0.4	0.3	0.2	0.4	0.7	0.1	0	0	0	0	0	2.1
> 5 <= 5.5	0	0	0	0	0	0	0	0	0	0	0.1	0.3	0.3	0.4	0.1	0	0	0	0	0	1.2
> 5.5 <= 6	0	0	0	0	0	0	0	0	0	0	0.1	0	0.1	0	0.1	0	0	0	0	0	0.3
> 6 <= 6.5	0	0	0	0	0	0	0	0	0	0	0	0	0	0	0	0	0	0	0	0	0
> 6.5 <= 7	0	0	0	0	0	0	0	0	0	0	0	0	0	0	0	0	0	0	0	0	0
> 7 <= 7.5	0	0	0	0	0	0	0	0	0	0	0	0.1	0	0	0	0	0	0	0	0	0.1
Total	0	0.9	10.8	11.1	13.8	26.7	40.7	51	62.6	96.9	170.1	195	141.8	117.4	37.4	18	4.1	1.2	0.1	0	1000

Table A1.0.7 Summer (Dec-Feb) joint probability distribution (parts per thousand) of the significant wave height and peak spectral wave period (35 m depth)

Hs (m)	Peak spectral wave period Tp (s)																				
	0-1	**1-2**	**2-3**	**3-4**	**4-5**	**5-6**	**6-7**	**7-8**	**8-9**	**9-10**	**10-11**	**11-12**	**12-13**	**13-14**	**14-15**	**15-16**	**16-17**	**17-18**	**18-19**	**19-20**	**Total**
> 0 <= 0.5	0	0.8	7.2	0.8	2.1	6.1	7.3	6.2	4.8	8.7	10	6.9	3.2	2.1	1.7	0.7	0.4	0.3	0	0	69.3
> 0.5 <= 1	0	0	4.7	13.6	6.1	10.7	19.8	24.8	33.9	50.4	69.1	72.2	39.1	31.9	7.6	3.5	0.6	0	0	0	388
> 1 <= 1.5	0	0	0	1.4	11.1	11.8	13.6	18.8	33.9	46.8	74.4	60.3	27.2	20	7.9	1.7	0.1	0	0	0	329
> 1.5 <= 2	0	0	0	0	0.3	10.4	8.9	9	10.8	14.5	22	23	11.9	8.7	0.8	0	0	0	0	0	120.3
> 2 <= 2.5	0	0	0	0	0	0.4	9	5.5	3.7	6.9	12.5	7.5	1.9	3.9	0.1	0	0	0	0	0	51.4
> 2.5 <= 3	0	0	0	0	0	0	0.4	5.8	2.8	2.9	5.4	4.3	2.1	1.2	0.3	0	0	0	0	0	25.2
> 3 <= 3.5	0	0	0	0	0	0	0	1.9	2.9	1.7	2.6	0.7	0.1	0.7	0.1	0	0	0	0	0	10.7
> 3.5 <= 4	0	0	0	0	0	0	0	0.3	1.4	0.8	0.3	0.1	0	0.3	0.1	0	0	0	0	0	3.3
> 4 <= 4.5	0	0	0	0	0	0	0	0	0	0.1	0.4	0.6	0	0	0	0	0	0	0	0	1.1
> 4.5 <= 5	0	0	0	0	0	0	0	0	0	0.3	0.4	0	0	0	0	0	0	0	0	0	0.7
> 5 <= 5.5	0	0	0	0	0	0	0	0	0	0	0	0	0	0	0	0	0	0	0	0	0
> 5.5 <= 6	0	0	0	0	0	0	0	0	0	0	0	0	0	0	0	0	0	0	0	0	0
> 6 <= 6.5	0	0	0	0	0	0	0	0	0	0	0	0.1	0	0	0	0	0	0	0	0	0.1
> 6.5 <= 7	0	0	0	0	0	0	0	0	0	0	0.1	0	0	0	0	0	0	0	0	0	0.1
> 7 <= 7.5	0	0	0	0	0	0	0	0	0	0	0	0.3	0	0	0	0	0	0	0	0	0.3
Total	0	0.8	11.9	15.8	19.6	39.4	59	72.3	94.2	133.1	197.2	176	85.5	68.8	18.6	5.9	1.1	0.3	0	0	1000

Table A1.0.8 Autumn (Mar-May) joint probability distribution (parts per thousand) of the significant wave height and peak spectral wave period (35 m depth)

Hs (m)	Peak spectral wave period Tp (s)																				
	0-1	1-2	2-3	3-4	4-5	5-6	6-7	7-8	8-9	9-10	10-11	11-12	12-13	13-14	14-15	15-16	16-17	17-18	18-19	19-20	Total
> 0 <= 0.5	0	0.3	3.4	0.1	0.4	3.3	3.4	2.7	1.6	4.2	3.3	7.3	1.9	0.5	0.5	0.3	0.1	0	0	0	33.3
> 0.5 <= 1	0	0	2.4	6.4	3.1	5	10.5	13.7	11.4	20.7	45.9	62.1	39.5	31.5	6.9	4.3	1.2	0.7	0	0	265.3
> 1 <= 1.5	0	0	0	0.3	7.3	8.2	4.5	9.2	12.4	26.8	53.7	65.8	70.1	49.7	14.8	7.3	1.6	0	0	0	331.7
> 1.5 <= 2	0	0	0	0	0.3	5.2	7.2	4.5	9.4	15.4	32.1	30.6	38.9	32.1	9.2	3.8	0.4	0	0	0	189.1
> 2 <= 2.5	0	0	0	0	0	0.1	7.6	3.7	2.4	4.1	14	17.5	16.8	13.7	3.5	2.3	0	0	0	0	85.7
> 2.5 <= 3	0	0	0	0	0	0	0.5	5.6	1.8	2.4	8	10.9	9.5	6.5	2.7	0.5	0	0	0	0	48.4
> 3 <= 3.5	0	0	0	0	0	0	0	2.3	2.4	0.5	1.5	5.6	6.1	4.3	0.3	0.1	0	0	0	0	23.1
> 3.5 <= 4	0	0	0	0	0	0	0	0.3	3	1	0.3	1.8	2.4	3.3	0.8	0	0	0	0	0	12.9
> 4 <= 4.5	0	0	0	0	0	0	0	0	0.7	0.8	0.5	0.7	0.8	1.5	0	0	0	0	0	0	5
> 4.5 <= 5	0	0	0	0	0	0	0	0	0	1	0.1	0.3	1	1.4	0	0	0	0	0	0	3.8
> 5 <= 5.5	0	0	0	0	0	0	0	0	0	0.1	0	0.4	0.5	0.3	0	0	0	0	0	0	1.3
> 5.5 <= 6	0	0	0	0	0	0	0	0	0	0	0.1	0	0	0	0	0	0	0	0	0	0.1
> 6 <= 6.5	0	0	0	0	0	0	0	0	0	0	0	0	0	0	0	0	0	0	0	0	0
> 6.5 <= 7	0	0	0	0	0	0	0	0	0	0	0	0	0	0	0	0	0	0	0	0	0
> 7 <= 7.5	0	0	0	0	0	0	0	0	0	0	0	0	0	0	0	0	0	0	0	0	0
Total	0	0.3	5.8	6.8	11.1	21.8	33.7	42	45.1	77	159.5	203	187.5	144.8	38.7	18.6	3.3	0.7	0	0	1000

Table A1.0.9 Winter (Jun-Aug) joint probability distribution (parts per thousand) of the significant wave height and peak spectral wave period (35 m depth)

Hs (m)	Peak spectral wave period Tp (s)																				
	0-1	**1-2**	**2-3**	**3-4**	**4-5**	**5-6**	**6-7**	**7-8**	**8-9**	**9-10**	**10-11**	**11-12**	**12-13**	**13-14**	**14-15**	**15-16**	**16-17**	**17-18**	**18-19**	**19-20**	**Total**
> 0 <= 0.5	0	0.8	4.9	0.3	2.9	3.5	4.3	4.2	2.9	2.7	5.6	7.3	2.9	2.4	0.7	0.8	0	0	0	0	46.2
> 0.5 <= 1	0	0	2	4.5	3.8	1.6	7.5	11.7	7.2	17.5	28.9	42	33.2	29.5	13.7	5.7	3.1	0	0	0	211.9
> 1 <= 1.5	0	0	0	0.3	4.5	6.5	4.3	9.6	18.3	22	45.7	49	38.3	37.9	18.1	11.8	1	0.3	0	0	267.6
> 1.5 <= 2	0	0	0	0	0	5.8	5.4	7.3	9.9	24.3	40.9	43.3	29.9	22.7	6.9	2.9	0.7	0	0	0	200
> 2 <= 2.5	0	0	0	0	0	0.3	4.2	6.4	4.3	9.8	25.1	36.8	20.5	20.5	2.9	1.5	0.3	0	0	0	132.6
> 2.5 <= 3	0	0	0	0	0	0	1.2	7.1	1.4	3.8	7.1	21.2	13.2	13.3	1.4	1.2	0.1	0	0	0	71
> 3 <= 3.5	0	0	0	0	0	0	0	1.2	3.5	1	2.3	10.5	7.2	7.3	3	0	0	0	0	0	36
> 3.5 <= 4	0	0	0	0	0	0	0	0.3	2.2	0.5	0.7	3.8	4.6	5.2	1.6	0	0	0	0	0	18.9
> 4 <= 4.5	0	0	0	0	0	0	0	0	0.5	1	0.3	1.1	2.2	2.2	0.3	0	0	0	0	0	7.6
> 4.5 <= 5	0	0	0	0	0	0	0	0	0	0.4	0.7	0.4	0.4	1.5	0.3	0	0	0	0	0	3.7
> 5 <= 5.5	0	0	0	0	0	0	0	0	0	0	0.4	0.5	0.5	1.2	0.5	0	0	0	0	0	3.1
> 5.5 <= 6	0	0	0	0	0	0	0	0	0	0	0.1	0.1	0.3	0.1	0.3	0	0	0	0	0	0.9
> 6 <= 6.5	0	0	0	0	0	0	0	0	0	0	0	0	0	0.1	0.1	0	0	0	0	0	0.2
> 6.5 <= 7	0	0	0	0	0	0	0	0	0	0	0	0	0	0	0	0	0	0	0	0	0
> 7 <= 7.5	0	0	0	0	0	0	0	0	0	0	0	0	0	0	0	0	0	0	0	0	0
Total	0	0.8	6.9	5.1	11.2	17.7	26.9	47.8	50.2	83	157.8	216	153.2	143.9	49.8	23.9	5.2	0.3	0	0	1000

Table A1.0.10 Spring (Sep-Nov) joint probability distribution (parts per thousand) of the significant wave height and peak spectral wave period (35 m depth)

Hs (m)	Peak spectral wave period Tp (s)																				
	0-1	**1-2**	**2-3**	**3-4**	**4-5**	**5-6**	**6-7**	**7-8**	**8-9**	**9-10**	**10-11**	**11-12**	**12-13**	**13-14**	**14-15**	**15-16**	**16-17**	**17-18**	**18-19**	**19-20**	**Total**
> 0 <= 0.5	0	1.5	13.6	1.1	2.1	6.6	9.8	4	3.2	4	7.7	6.7	2.7	1.9	0.8	1.2	0.4	0.3	0	0	67.6
> 0.5 <= 1	0	0	4.8	14.7	4.5	5.4	11.3	10.3	18.4	24.3	46.4	48.2	46	39.6	13.3	9.6	4	2.3	0.3	0	303.4
> 1 <= 1.5	0	0	0	1	6.7	6.6	4.8	10.2	21.6	34.9	51.9	60.6	45.3	34.9	14	6.2	1.8	1.1	0	0	301.6
> 1.5 <= 2	0	0	0	0	0.3	9.5	7.6	6.6	11.8	22.7	34.3	39.1	22	17.4	8.1	1.6	0.8	0	0	0	181.8
> 2 <= 2.5	0	0	0	0	0	0.4	8.8	5.2	2.6	7.7	18.3	16.8	13.9	7.1	2.6	2.3	0	0	0	0	85.7
> 2.5 <= 3	0	0	0	0	0	0	1.1	4.3	1.2	1.2	5.8	8.8	6.6	4.5	1	1.1	0	0	0	0	35.6
> 3 <= 3.5	0	0	0	0	0	0	0	1.9	1.5	0.3	1.1	1.9	2.6	4	1.8	0.8	0	0	0	0	15.9
> 3.5 <= 4	0	0	0	0	0	0	0	0.1	0.7	0.4	1	1.5	0.5	1.8	0.1	0.3	0	0	0	0	6.4
> 4 <= 4.5	0	0	0	0	0	0	0	0	0	0	0	0.3	0.3	0.3	0.4	0	0	0	0	0	1.3
> 4.5 <= 5	0	0	0	0	0	0	0	0	0	0	0.1	0	0.3	0	0	0	0	0	0	0	0.4
> 5 <= 5.5	0	0	0	0	0	0	0	0	0	0	0.1	0.1	0	0	0	0	0	0	0	0	0.2
> 5.5 <= 6	0	0	0	0	0	0	0	0	0	0	0	0	0	0	0	0	0	0	0	0	0
> 6 <= 6.5	0	0	0	0	0	0	0	0	0	0	0	0	0	0	0	0	0	0	0	0	0
> 6.5 <= 7	0	0	0	0	0	0	0	0	0	0	0	0	0	0	0	0	0	0	0	0	0
> 7 <= 7.5	0	0	0	0	0	0	0	0	0	0	0	0	0	0	0	0	0	0	0	0	0
Total	0	1.5	18.4	16.8	13.6	28.5	43.4	42.6	61	95.5	166.7	184	140.2	111.5	42.1	23.1	7	3.7	0.3	0	1000

Table A1.0.11 Annual persistence non-exceedence (%) for total significant wave height (35 m depth)

Hs (m)	Duration (hours)											
	> 6	**> 12**	**> 18**	**> 24**	**> 30**	**> 36**	**> 42**	**> 48**	**> 54**	**> 60**	**> 66**	**> 72**
<= 1	0	0	0	0	0	0	0	0	0	0	0	0
<= 1.5	5.07	4.49	3.72	2.98	2.02	1.48	1.12	0.64	0.35	0.08	0.08	0
<= 2.0	34.17	33.07	31.57	29.44	27.56	26.03	24.1	21.94	20.39	18.61	17.14	15.78
<= 2.5	65.09	64.3	63.43	62.34	61.26	60.25	58.88	57.51	56.07	54.67	53.34	51.66
<= 3.0	82.48	82.09	81.7	81.24	80.68	80.02	79.18	78.81	78.27	77.34	76.67	76.02
<= 3.5	91.44	91.32	91.07	90.76	90.41	90.01	89.51	89.3	89.18	88.85	88.63	88.3
<= 4.0	96.03	95.97	95.88	95.7	95.57	95.42	95.24	94.98	94.91	94.71	94.27	94.03
<= 4.5	98.19	98.17	98.14	98.07	98.01	98.01	97.91	97.81	97.69	97.62	97.62	97.54
<= 5.0	99.24	99.23	99.21	99.13	99.1	99.1	99.1	99.1	99.1	99.1	99.1	99.1
<= 5.5	99.62	99.62	99.62	99.62	99.58	99.54	99.54	99.54	99.54	99.54	99.54	99.54
<= 6.0	99.83	99.83	99.83	99.83	99.83	99.83	99.83	99.83	99.83	99.83	99.83	99.83

Table A1.0.12 Annual persistence exceedence (%) for total significant wave height (35 m depth)

Hs (m)	Duration (hours)											
	> 6	**> 12**	**> 18**	**> 24**	**> 30**	**> 36**	**> 42**	**> 48**	**> 54**	**> 60**	**> 66**	**> 72**
>= 0	100	100	100	100	100	100	100	100	100	100	100	100
>= 0.5	94.47	94.38	94.27	94.17	93.84	93.69	93.59	93.32	93.26	93.13	92.91	92.26
>= 1	65.1	64.3	63.2	62.19	61.17	59.79	58.68	57.24	55.46	53.33	51.85	50.01
>= 1.5	34.2	33.34	31.81	30.21	28.47	26.51	25.32	23.67	21.96	20.68	19.42	18.21
>= 2	16.99	16.2	15.08	13.82	12.34	10.89	10.06	9.18	8.46	7.2	6.55	5.82
>= 2.5	8.23	7.36	6.79	5.92	5.06	4.23	3.81	2.96	2.61	2.14	1.63	1.3
>= 3	3.83	3.39	2.63	2.15	1.84	1.25	1.01	0.95	0.72	0.72	0.72	0.55
>= 3.5	1.67	1.35	1.04	0.8	0.6	0.48	0.43	0.33	0.27	0.27	0.27	0.27
>= 4	0.69	0.52	0.34	0.23	0.23	0.16	0.16	0.11	0.11	0.11	0.11	0.11
>= 4.5	0.36	0.23	0.13	0.13	0.13	0.09	0.09	0.09	0.09	0.09	0.09	0.09
>= 5	0.13	0.1	0.06	0.06	0.06	0.06	0.06	0.06	0	0	0	0

Table A1.0.13 Monthly significant wave height exceedence (35 m depth)

Hs (m)	Month											
	Jan	**Feb**	**Mar**	**Apr**	**May**	**Jun**	**Jul**	**Aug**	**Sep**	**Oct**	**Nov**	**Dec**
> 0	100	100	100	100	100	100	100	100	100	100	100	100
> 0.5	90.73	94.55	96.25	96.79	96.94	95.25	95.93	94.96	92.79	93.83	93.08	94.03
> 1	47.76	58.07	63.79	71.67	74.92	75.67	70.81	76.13	59.54	64.27	64.83	57.3
> 1.5	19.23	23.45	30.2	42.38	38.47	49.17	42.7	50.44	33.38	31.61	33.29	21.61
> 2	8.46	9.71	12.82	21.04	20.4	27.25	24.44	30.52	17.63	12.38	13.75	9.84
> 2.5	4.23	4.12	6.01	11.54	10.93	14	12.38	16.09	8.54	3.99	5.5	4.15
> 3	2.02	1.11	2.82	5.42	5.65	6.79	6.69	7.66	4.08	1.57	1.67	1.77
> 3.5	0.69	0.4	1.29	2.75	2.86	3.96	3.51	2.9	1.25	0.6	0.67	0.6
> 4	0.2	0.31	0.32	1.33	1.41	2.29	1.33	1.09	0.29	0.12	0.17	0.2
> 4.5	0.12	0.27	0.12	0.83	0.6	1.63	0.32	0.52	0.13	0	0.08	0
> 5	0	0.18	0	0.25	0.2	1.04	0.08	0.24	0.08	0	0	0
> 5.5	0	0.18	0	0.04	0	0.29	0	0.08	0	0	0	0
> 6	0	0.18	0	0	0	0.08	0	0	0	0	0	0
> 6.5	0	0.13	0	0	0	0	0	0	0	0	0	0
> 7	0	0.09	0	0	0	0	0	0	0	0	0	0
> 7.5	0	0	0	0	0	0	0	0	0	0	0	0